



**UNIVERSITÀ DEGLI STUDI DI CAGLIARI**  
**FACOLTÀ DI SCIENZE MATEMATICHE FISICHE E NATURALI**  
**Scuola di Dottorato in Scienze e Tecnologie Fisiche**

XXII Ciclo  
2006 – 2009

**Accreting millisecond X-ray pulsars: a  
search for pulsed radio emission and  
constraints from the *radio-ejection*  
mechanism**

**Ph.D. Thesis by**  
Maria Noemi Iacolina

**Supervisors**

Prof. Luciano Burderi – Dott.ssa Marta Burgay  
Dott. Andrea Possenti – Dott.ssa Tiziana Di Salvo

*To my love,  
who is doing so much for me*

# Contents

<b>Introduction</b>	<b>1</b>
<b>1 X-ray accretion-powered and radio rotation-powered millisecond pulsars</b>	<b>3</b>
1.1 Neutron stars and pulsars . . . . .	4
1.2 Roche geometry . . . . .	6
1.3 X-ray accretion-powered millisecond pulsars . . . . .	9
1.3.1 The Eddington limit . . . . .	9
1.3.2 The emitted spectrum . . . . .	10
1.3.3 Classification of X-Ray Binaries . . . . .	11
1.3.4 Binary evolution of LMXBs . . . . .	13
1.3.5 Disc accretion onto magnetized neutron stars . . . . .	19
1.4 Rotation-powered millisecond pulsars . . . . .	22
1.4.1 Electrodynamics and radio emission properties . . . . .	24
1.4.2 The signal shape . . . . .	27
1.5 Standard evolutionary link between accretion-powered and rotation-powered millisecond pulsars . . . . .	31
1.5.1 Evolution of isolated rotation-powered pulsars . . . . .	31
1.5.2 Evolution of binary pulsars: the <i>recycling</i> model . . . . .	32
1.5.3 Magnetic evolution in accreting binary NSs . . . . .	34
<b>2 New evolutionary scenarios</b>	<b>38</b>
2.1 Introduction . . . . .	39
2.1.1 Open issues . . . . .	40
2.2 The mechanism of “radio-ejection” . . . . .	41
2.2.1 Luminosity during accretion . . . . .	47

2.3	Comparisons with observations . . . . .	48
2.4	Results . . . . .	51
2.5	New estimates for parameters of MSPs and AMXPs . . . . .	52
2.5.1	Age of MSPs . . . . .	52
2.5.2	Magnetic field of AMXPs . . . . .	53
2.6	Effects of the uncertainties on the pulsar parameters and of the equation of state and observational biases . . . . .	55
2.6.1	Effects of the parameters uncertainties . . . . .	56
2.6.2	The effects of the equation of state and observational biases . . . . .	59
2.7	Conclusions . . . . .	60
<b>3</b>	<b>Search for radio pulsed emission from four accreting millisecond X-ray pulsars</b>	<b>64</b>
3.1	Introduction . . . . .	65
3.1.1	Constraints for the switch-on of radio emission . . . . .	65
3.1.2	The effect of the matter enclosing the system . . . . .	66
3.2	The sources, the observations and the data analysis . . . . .	67
3.2.1	Constraints from the surface magnetic field . . . . .	71
3.2.2	Constraints from optical observations . . . . .	73
3.3	Results . . . . .	74
3.3.1	Upper limit on the flux density . . . . .	78
3.4	Discussion . . . . .	79
3.4.1	The geometric factor . . . . .	80
3.4.2	The luminosity upper limits . . . . .	80
3.5	Conclusions . . . . .	82
	<b>Conclusions</b>	<b>88</b>
	<b>A Physical and astronomical constants and units</b>	<b>91</b>
	<b>B The Parkes radiotelescope</b>	<b>93</b>
	<b>List of Figures</b>	<b>100</b>
	<b>List of Tables</b>	<b>103</b>



# List of symbols

$a$	Binary separation
$B$ ( $B_s$ )	Magnetic field (surface magnetic field)
$e$	Eccentricity of a binary system
$G$	Nominal gain of a radio telescope
$L$	Pseudo-luminosity of a pulsar
$L_{\text{acc}}, L_X$ ( $L_{37}$ )	Accretion luminosity (in units of $10^{37}$ erg s $^{-1}$ )
$M_1, M_2$ ( $m, m_2$ )	Primary and secondary star masses (in solar masses)
$M_c$	Companion star mass
$\dot{M}$ ( $\dot{m}_{-10}$ )	Mass accretion rate (in units of $10^{-10} M_\odot \text{y}^{-1}$ )
$n$	Index of the mass-radius relation ( $R \propto M^n$ )
$n_p$ ( $n_{0.615}$ )	Mean particle mass (in units of the proton mass)
$N_s$	Samples number
$P_S$ ( $P_{-3}$ )	Spin period (in milliseconds) of the pulsar
$\dot{P}_S$	Spin period derivative of the pulsar
$\mathcal{P}_{\text{MAG}}$	Magnetic pressure
$\mathcal{P}_{\text{DIP}}$	Radiation pressure of the rotating magneto-dipole
$\mathcal{P}_{\text{DISK}}$	Shakura-Sunyaev disk pressure
$P_{\text{orb}}$ ( $P_h$ )	Orbital period (in hours)
$q$	Mass ratio, $M_2/M_1$
$R_A$	Alfvén radius
$R_{L_1}, R_{L_2}$	Roche lobe radius of the primary and secondary star
$R_{\text{lc}}$	Light cylinder radius

$R_M$	Magnetospheric radius
$R_{NS} (R_6)$	Neutron star radius (in units of $10^6$ cm)
$R_\Omega$	Corotation radius
$S$	Minimum detectable flux density
$T_{sky}$	Sky temperature
$T_{sys}$	System temperature of a radio telescope
$\alpha$	Shakura-Sunyaev viscosity parameter
$\Delta t$	Data serie time
$\delta t_{DM}$	Dispersion broadening
$\delta t_{sam}$	Sampling time
$\delta t_{scatt}$	Scattering broadening
$\eta_{acc}$	Accretion efficiency
$\mu (\mu_{26})$	Magnetic moment (in units of $10^{-26}$ G cm <sup>3</sup> )
$\nu_{obs} (\nu_9)$	Observing radio frequency (in units of $10^9$ Hz)
$\nu_S$	Spin frequency of the pulsar
$\dot{\nu}_S$	Spin frequency derivative of the pulsar
$\tau (\tau_c)$	Age of a pulsar (characteristic age)
$\tau_{ff}$	Free-free optical depth
$\Omega_K$	Keplerian velocity

# Acronyms

AMXP	Accreting millisecond X-ray pulsar
GR	Gravitational radiation
GBT	Green bank radio telescope
HMXB	High mass X-ray binary
LMXB	Low mass X-ray binary
MSP	Millisecond pulsar
NS	Neutron star



# Introduction

In this thesis I present the work performed in my three years PhD, developed in the framework of the studies devoted to clarify still unsolved issues of the so-called recycling scenario.

This model argues the existence of an evolutionary link between the low mass X-ray binaries (LMXBs), binary systems containing a low magnetized ( $B < 10^{10}$  G) NS accreting mass from a low mass ( $M < 1 M_{\odot}$ ) companion, and the radio millisecond pulsars (MSPs), asserting that LMXBs are progenitors of at least some of the radio MSPs.

A bridge between these two classes of astronomical objects is likely represented by the accreting millisecond X-ray pulsars (AMXPs), a subclass of LMXBs showing short accretion episodes (outbursts, of the order of tens of days) during which the pulsed X-ray emission reaches luminosity  $L_X \approx 10^{36\div38}$  erg s<sup>-1</sup>, in the range 0.5-10 keV, alternated to longer quiescence phases during which the luminosity drops to  $10^{31\div34}$  erg s<sup>-1</sup>. In **Chapter 1** a description of the characteristics of LMXBs, radio MSPs and AMXPs is given, as well as a detailed presentation of the recycling model.

The theoretical part of my PhD work, presented in **Chapter 2**, is aimed to investigate the spin and orbital characteristics of the observed radio MSPs in order to provide observational support to the mechanism of the so-called *radio-ejection*. This is an effect due to the radiation pressure of the NS rotating magneto-dipole during a phase of matter transfer in accretion systems that prevents the infalling matter to reach the NS surface by ejecting it away from the binary at the inner Lagrangian point.

The occurrence of a radio-ejection phase allows one to solve some of the still unanswered difficulties of the recycling model, e.g. the lacking of ultra-

rapidly spinning pulsars (with spin period less than 1 ms).

A unambiguous observational proof of the recycling mechanism would be provided by the detection of coherent radio pulsations in a LMXB, at the same repetition period of coherent X-ray pulsations. The best candidates for this key-observation are the AMXPs. Hence, the observational part of my PhD work focused on a search for radio millisecond pulsations on four of the twelve known AMXPs during their quiescence phase, XTE J0929–314, XTE J1751–305, XTE J1814–338 and SAX J1808.4–3658.

The search, presented in **Chapter 3**, has been realized in three steps, exploiting the precise knowledge of the orbital and spin ephemerides of the NS in these systems obtained from observations in X-rays. I first dedispersed the data series, two for each source (taken from Parkes radiotelescope, Australia), in order to minimize the effect of the interstellar medium, then I barycentred the time series to remove both the effects of motion of the NS in the binary system and of the earth in the solar system. Finally, I folded the time series according to the spin parameters obtained from X-ray observations, in order to increase the signal to noise ratio.

The last part of my thesis (**Conclusions**) reports a brief summary of the outcome of my work.

## **Chapter 1**

# **X-ray accretion-powered and radio rotation-powered millisecond pulsars**

## 1.1 Neutron stars and pulsars

A neutron star is a type of remnant that can result from the gravitational collapse of a massive star ( $M \gtrsim 8 M_{\odot}$ ) during a Type II, Type Ib or Type Ic supernova event, which occurs when a massive star runs out of nuclear fuel in its core at the end of its life.

A typical neutron star has a mass between  $1 M_{\odot} - 2.1 M_{\odot}$ , with a corresponding radius range of 8 – 15 km and then a resulting central density of  $10^{14} - 10^{15} \text{ g/cm}^3$  (Lattimer & Prakash 2007). The combination of high mass and small size results in an extremely large gravitational field, estimated to be about  $10^{11}$  times that on the Earth.

Such stars are mostly composed of neutrons, subatomic particles without electrical charge and roughly the same mass as protons. They are very hot and are supported against further collapse by the nuclear forces and the Pauli exclusion principle, which states that no two neutrons (or any other fermionic particle) can occupy the same quantum state simultaneously.

The neutron subatomic particle was discovered in 1932 by Sir James Chadwick (Chadwick 1932), who was awarded the Nobel Prize in Physics in 1935 for his discovery. By bombarding the hydrogen atoms in paraffin with emissions from beryllium that was itself being bombarded with alpha particles, he demonstrated that these emissions contained a neutral particle that had about the same mass as a proton.

In 1933, Walter Baade and Fritz Zwicky proposed the existence of the neutron star (Baade & Zwicky 1934), only a year after Chadwick's discovery of the neutron. In seeking an explanation for the origin of a supernova, they proposed that the neutron star is formed in a supernova. Supernovae are suddenly appearing dying stars in the sky, whose luminosity in the optical might outshine an entire galaxy for days to weeks. Baade and Zwicky correctly proposed that the release of the gravitational binding energy that accompanies the formation of the neutron stars powers the supernova: "In the supernova process mass in bulk is annihilated".

In 1965, Antony Hewish and Samuel Okoye discovered "an unusual

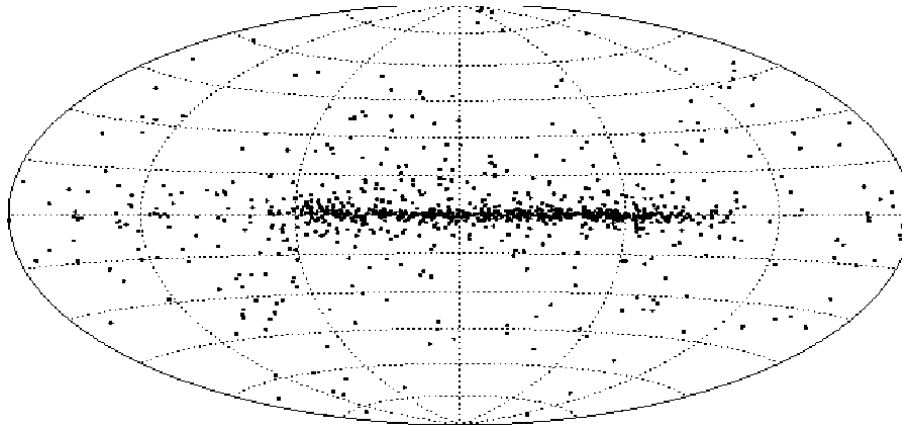


Figure 1.1: Galactic distribution of the known population of radio pulsars. -

<http://www.astro.wisc.edu/goat/article/7/the-milky-way-using-real-data>

source of high radio brightness temperature in the Crab Nebula". This source turned out to be the Crab Nebula neutron star that resulted from the great supernova of 1054.

In 1967, Jocelyn Bell and Antony Hewish (awarded the Nobel Prize in Physics in 1974; Hewish et al. (1968)) discovered regular radio pulses, with a period of 1.337 s, firstly interpreted as possible signals from an extraterrestrial intelligence and the first pulsar was nicknamed LGM1 (for Little Green Man 1).

The evidence that pulsars were indeed neutron stars came from the discovery, a year later, of the pulsar in the location of the Hewish and Okoye radio source (Cocke et al. 1969). These pulses were then interpreted as originating from an isolated, rotating neutron star. The energy source of the radio pulsar is the rotational energy of the neutron star (see Section 1.4) and for this reason they are named rotation-powered pulsars. The largest number of known neutron stars are of this type. At present more than 1800 radio pulsars are known and their galactic distribution is shown in Fig. 1.1.

Another class of pulsars is that of the accretion-powered pulsars (see Sec. 1.3) and in order to understand the basic mechanism for this type of objects in the following we will focus on the accretion mechanism and the geometry of binary systems.

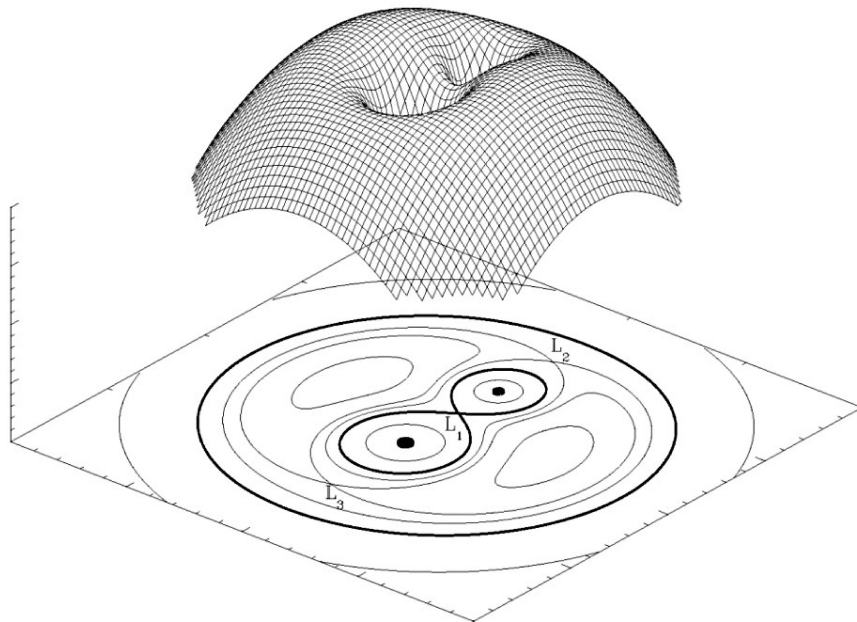


Figure 1.2: A three-dimensional representation of the Roche potential in a binary star. The droplet-shaped figures in the equipotential plot at the bottom of the figure are called the Roche lobes of each star.  $L_1$ ,  $L_2$  and  $L_3$  are the Lagrangian points where forces cancel out. Mass can flow through the saddle point  $L_1$  from one star to its companion, if the latter fills its Roche lobe. - <http://hemel.waarnemen.com/Informatie/Sterren/hoofdstuk6.html#mtr>.

## 1.2 Roche geometry

The majority of stars in the universe is thought to be or to have been part of a binary system at some stage of their evolutionary lifetimes. During this phase, some stars may undergo matter accretion from the companion star.

Following the approach of Frank et al. (2002), there exist two main way in which binaries can transfer matter and these are:

- (a) **accretion via Roche lobe overflow:** due to the fact that in the course of its evolution, one of the two stars in the binary system may increase in radius, or the binary separation shrinks, to the point where the gravitational pull of the companion can remove the outer layers of its

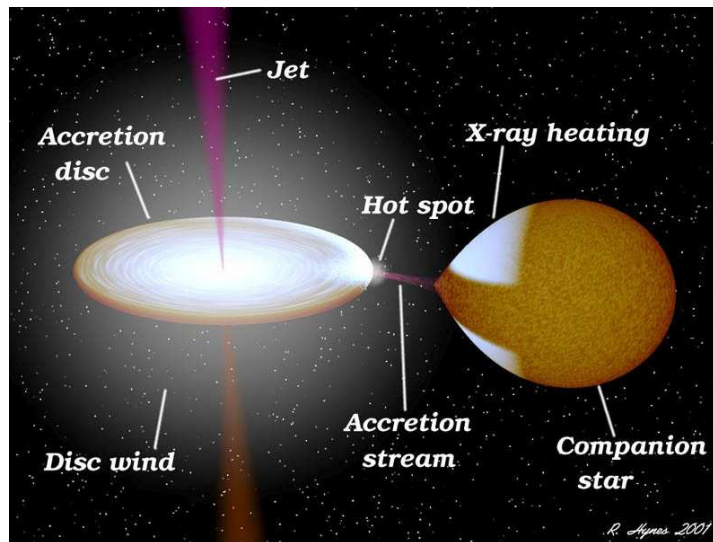


Figure 1.3: Graphic illustration of an X-ray binary system. - [http://www.redorb.it.com/education/reference/\\_library/universe/xray/\\_binaries/257/index.html](http://www.redorb.it.com/education/reference/_library/universe/xray/_binaries/257/index.html)

envelope;

- (b) **accretion via stellar wind:** due to the fact that one of the stars may, at some evolutionary phase, eject much of its mass in the form of a stellar wind; some of this material will be gravitationally captured by the companion.

The case (b) won't be treated in detail, since it is not the specific case for this thesis work.

### Accretion via Roche lobe overflow

The problem was first studied by Edouard Roche in the 19<sup>th</sup> century considering two auto-gravitating bodies orbiting around a common centre of mass, which influence a gravitationally bound test mass.

In Fig. 1.2 a representation of the shape of the equipotential lines around a binary system is illustrated. The regions of space around each star within which orbiting material is gravitationally bound to that star are called Roche lobes and are visible in the bottom part of the Fig. 1.2 as the droplet-shaped

figures.

The shapes of the Roche lobes are determined only by the mass ratio of the two stars,  $q = M_2/M_1$ , whereas the overall scale is fixed by the binary separation  $a$ , which can be expressed from the third Kepler's law as

$$a = \left( \frac{G(M_1 + M_2)P_{\text{orb}}^2}{4\pi^2} \right)^{1/3}, \quad (1.1)$$

where  $G$  is the gravitational constant,  $M_1$  and  $M_2$  are the masses of the two stars and  $P_{\text{orb}}$  is the orbital period of the system. Hereafter we will name primary the star with mass  $M_1$  and secondary that with mass  $M_2$ . An useful approximated expression of the radius of the Roche lobe of a star,  $R_{L_2}$ , valid to 2%, for  $q \lesssim 0.8$ , is given by Paczyński (1967):

$$R_{L_2} = 0.46a \left( \frac{M_2}{M_1 + M_2} \right)^{1/3}. \quad (1.2)$$

An analogous expression for  $R_{L_1}$  can be obtained by replacing  $q$  with  $q^{-1}$ .

If the two stars in the binary system are smaller than their Roche lobes, there is no tendency for material to be pulled off from one of the stars by the gravitational attraction of the other; the binary is said *detached* and mass transfer could proceed only via wind mechanism. However, if, for some reason (e.g. stellar evolution), one of the stars, for example the secondary, swells up so that its surface fills its Roche lobe, part of its envelope will lie very close to the inner Lagrangian point,  $L_1$ , a point of unstable equilibrium (see Figure 1.2 and its caption). Any perturbation of this material will push it over  $L_1$  into the Roche lobe of the primary, where it must, eventually be captured by the star. Such perturbations are always present, provided, for example, by pressure forces. A system like this is said *semi-detached*, and will efficiently transfer mass from the secondary to the primary star for as long as the secondary remains in contact with its Roche lobe (see Sec. 1.3.4).

This accreting matter, transferring toward the Roche lobe of the primary star  $M_1$  through  $L_1$ , keeps an high angular momentum, hence it can not be directly captured by that star and will start to rotate around  $M_1$  giving rise to the formation of an accretion disk. Accretion disks are matter configurations which, through dissipative processes (as viscosity), are able to transport the angular momentum from the inner parts of the disk to the outers one

(thus accomplishing the conservation of the total angular momentum), while matter can slowly drifting inwards.

Energy dissipation in the disk leads orbits to evolve toward configurations with minimum energy, which correspond to circular shape, with the matter coiling to lower radii moving with keplerian velocity:

$$\Omega_K(r) = \sqrt{\frac{GM_1}{r^3}}. \quad (1.3)$$

### 1.3 X-ray accretion-powered millisecond pulsars

Accretion-powered pulsars (Fig. 1.3) belong to the broader class of X-ray binaries, systems in which a compact object (a neutron star or black hole) accretes mass from a companion star (possibly filling its Roche lobe or ejecting mass via stellar wind). As a mass  $m$  is accreted onto the compact object,  $M_1$ , it releases its gravitational binding energy  $\Delta E = (GM_1/R_*)m$ , where  $R_*$  is the radius of the accreting object. If all of the kinetic energy of the in-falling matter is converted in radiation, the accretion luminosity will result:

$$L_{\text{acc}} = \frac{\Delta E}{\Delta t} = \frac{GM_1\dot{M}}{R_*}, \quad (1.4)$$

where  $\dot{M}$  is the mass accretion rate.

The efficiency of this process is evaluated by comparison with the total rest energy available,  $\eta_{\text{acc}} = \Delta E/mc^2 = GM_1/R_*c^2$  (that is  $L_{\text{acc}} = \eta_{\text{acc}}\dot{M}c^2$ ), and is higher for more compact objects: it is  $10^{-4}$  for a white dwarf and  $\sim 0.2$  for a neutron star. For a black hole undergoing disk accretion, we have to take into account the Schwarzschild radius,  $R_{\text{Sch}} = \frac{2GM}{c^2}$ ; the efficiency in this case reaches  $\sim 0.5$  for a Kerr black hole.

Accretion appears therefore as one of the most effective ways to convert energy into radiation, considering that thermonuclear fusion of four hydrogen nuclei into one  ${}^4\text{He}$  burns  $\sim 0.007$  times their rest energy.

#### 1.3.1 The Eddington limit

The energy amount that can be released through accretion however is limited by the so-called Eddington limit. This is the critical theoretical limit at which

the radiation pressure arising from the accretion itself would exceed the gravitational attraction towards the compact object.

Derived for stationary and spherically symmetric accretion, equating gravitational with radiation pressure, the Eddington limit results to be a function of the mass of the accreting object,  $M_1$ :

$$L_{\text{Edd}} = \frac{4\pi Gc}{\bar{k}} M_1, \quad (1.5)$$

where  $\bar{k}$  is the opacity near the surface of the star. It is possible to make an estimate of the Eddington limit for stars on the upper end of the main sequence, for which the effective temperature is high enough that most of the hydrogen is ionized in their photospheres and the opacity is dominated by Thomson scattering,  $\bar{k} = \bar{k}_T = n_e \sigma_T / \rho$ :

$$L_{\text{Edd}} = \frac{4\pi G M_1 m_p c}{\sigma_T} \cong 1.3 \times 10^{38} m \text{ erg} \cdot \text{s}^{-1}, \quad (1.6)$$

with  $n_e$  the number of free electron per  $\text{cm}^3$ ,  $\rho$  the density of the medium,  $m$  the mass of the accreting object in solar unit,  $m_p$  the proton mass and  $\sigma_T$  the Thomson cross section. Using Eq. 1.4, the Eddington mass transfer rate for a neutron star will result:

$$\dot{M}_{\text{Edd}} = \frac{4\pi R_{\text{NS}} m_p c}{\sigma_T} \cong 1.5 \cdot 10^{-8} R_6 \text{ } M_{\odot} \text{ yr}^{-1}, \quad (1.7)$$

where  $R_{\text{NS}}$  and  $R_6$  are the neutron star radius and the same in units of  $10^6$  cm.

### 1.3.2 The emitted spectrum

To have an estimate of the band of the electromagnetic spectrum in which the energy emitted by an accreting compact object is released, we consider a radiation temperature  $T_{\text{rad}} = h\nu/k$ , (with  $\nu$  the frequency of a typically emitted photon,  $k$  the Boltzmann constant and  $h$  the Planck constant) and define a black body temperature,

$$T_{\text{bb}} = \left( \frac{L_{\text{acc}}}{4\pi R_*^2 \sigma} \right)^{1/4}, \quad (1.8)$$

(with  $\sigma$  the Stefan-Boltzmann constant) at an accretion luminosity,  $L_{\text{acc}}$ , which is the temperature of a black body of radius  $R_*$  emitting the accretion energy.

The radiation temperature has to be in between the temperatures of the less ( $T_{\text{bb}}$ ) and most thermally efficient ways of converting heat into radiation, which is the thermal temperature defined as:

$$T_{\text{th}} = \frac{GMm_{\text{p}}}{3kR_*}; \quad (1.9)$$

i.e.  $T_{\text{bb}} \leq T_{\text{rad}} \leq T_{\text{th}}$ . Hence, for a NS of mass  $1.4, M_{\odot}$  it results:

$$10^7 \text{ K} \leq T_{\text{rad}} \leq 5 \times 10^{11} \text{ K} \longrightarrow 2 \text{ keV} \leq h\nu \leq 50 \text{ MeV}, \quad (1.10)$$

clearly pointing to the X-ray/ $\gamma$ -ray band of the spectrum.

### 1.3.3 Classification of X-Ray Binaries

X-Ray Binaries can be classified in several ways. A first distinction concerns their X-ray variability:

- Steady, in which we have a stable emission of X-rays flux;
- Transient (XRT) in which we observe a periodic modulation of the X-rays flux, alternating *outburst* phases, lasting periods of the order of months with a X-ray luminosity between  $10^{36}$  and  $10^{38} \text{ erg s}^{-1}$  and *quiescence* phases, lasting periods of the order of years in which luminosity drops down to  $10^{31-33} \text{ erg s}^{-1}$ .

A second classification is based on the ratio of X-ray to optical luminosity (Bradt & McClintock 1983),

$$\frac{L_{\text{X}}(2 - 10 \text{ keV})}{L_{\text{opt}}(300 - 700 \text{ nm})}, \quad (1.11)$$

they are divided in:

- high-mass X-ray binaries (HMXB) with ratio  $\lesssim 10$
- low-mass X-ray binaries (LMXB) with ratio  $\gtrsim 10$

This last classification coincides with a division based on the mass of the companion. This is because if the companion is an early type massive star, the optical luminosity will dominate. If the companion is a low mass star the optical luminosity will be dominated by the accretion disk.

Despite these classifications are regardless of the nature of the compact object (neutron star or black hole), in this work only the case regarding the neutron star will be treated.

### High-mass X-ray binaries

High-mass X-ray binaries are binary systems in which the secondary star is a massive star ( $\gtrsim 10 M_{\odot}$ , Hayakawa (1985)), usually an O or B type of population I, generally concentrated in the galactic plane. They are systems with eccentric orbits and high orbital separations,  $\gtrsim 20$  lt-s (and binary periods  $\gtrsim 1$  day), because of the huge sizes of the secondary star.

In these types of system, accretion of matter can occur either via stellar wind, very strong in this kind of secondary star, or via Roche lobe overflow. However, the timescale of this matter transfer is very short and, consequently, in this case that mechanism is hardly detectable.

The compact objects in HMXB are young neutron stars with high magnetic fields ( $\gtrsim 10^{12}$  G) which are often able to force the accreting matter to be channeled along the field lines until it reaches the magnetic polar caps causing the asymmetry in the emission responsible for the observed pulsed emission of X-rays at the spin period of the neutron star. Measured spin periods are in the range  $\sim 66$  ms  $\div$   $\sim 1000$  s.

### Low-mass X-ray binaries

Low-mass X-ray binaries are X binaries in which the secondary star is an evolved low mass population II star, which is not able to eject matter via stellar wind. Matter transfer will then be allowed only via Roche lobe overflow.

The most part of the known LMXB does not show coherent pulsation in their light curves. The reasons for that are still under debate: it could be due e.g. to the alignment of the magnetic field with the rotational axis or to a very low ( $< 10^8$  G) magnetic field which makes the matter accretion to happen on the entire neutron star surface.

The only subclass of LMXB in which coherent pulsations have been observed is that of the accreting millisecond X-ray pulsars (AMXPs). AMXPs are transient systems in which the outburst stage, associated to the matter falling onto the neutron star surface, has spun up the neutron star to periods of the order of millisecond. The list of the twelve known AMXPs is shown in

Table 1.1<sup>1</sup>.

In a larger subclass of LMXB, however, there are other indirect observational evidences for the spin period of the NS hosted in these system to have been pushed down to millisecond by the mass transfer, as we discuss in the following.

### 1.3.4 Binary evolution of LMXBs

In order to analyze the evolution of this kind of systems we have to keep in mind that the evolutionary processes are ruled by time scales for single stars, which, considering  $M$ ,  $L$ ,  $R$  the mass, luminosity and radius of the star respectively, are (Morton 1960):

- *nuclear time scale*,

$$\tau_{\text{nuc}} \simeq 10^{10} \frac{M}{M_{\odot}} \frac{L_{\odot}}{L} \text{ yr}, \quad (1.12)$$

the time scale on which a star evolves due to nuclear burning in the core;

- *thermal time scale*,

$$\tau_{\text{th}} \simeq 3.1 \times 10^7 \left( \frac{M}{M_{\odot}} \right)^2 \frac{R_{\odot}}{R} \frac{L_{\odot}}{L} \text{ yr}, \quad (1.13)$$

the time scale on which a star tries to restore thermal equilibrium when it is perturbed;

- *dynamical time scale*,

$$\tau_{\text{dyn}} \simeq 0.04 \left( \frac{M_{\odot}}{M} \right)^{1/2} \left( \frac{R}{R_{\odot}} \right)^{3/2} \text{ days}, \quad (1.14)$$

the time scale on which a star restores a perturbed hydrostatic equilibrium.

---

<sup>1</sup>References in the Table are: WV98 = Wijnands & van der Klis (1998); M02 = Markwardt et al. (2002); G02 = Galloway et al. (2002); M03 = Markwardt et al. (2003); M03b = Markwardt & Swank (2003); G05 = Galloway et al. (2005); K05 = Kaaret et al. (2006); K07 = Krimm et al. (2007); C08 = Casella et al. (2008); A08 = Altamirano et al. (2008); A09 = Altamirano et al. (2009); M09 = Markwardt et al. (2009).

LIST OF THE TWELVE KNOWN AMXPs					
Name	$P_s$ (ms)	$P_{orb}$ (hours)	Companion		Ref. <sup>1</sup>
			Class	Mass ( $M_\odot$ )	
SAX J1808.4–3658	2.5	2.01	BD	0.05	WV98
XTE J1751–305	2.3	0.71	DD	0.015	M02
XTE J0929–314	5.4	0.73	WD/He DD	0.02	G02
XTE J1807–294	5.2	0.67	DD	0.007	M03
XTE J1814–338	3.2	4.27	MS	0.17	M03b
IGR J00291+5934	1.7	2.46	BD	0.04	G05
HETE J1900.1–2455	2.7	1.39	BD	0.016	K05
SWIFT J1756.9–2508	5.5	0.90	He WD	0.007	K07
Aql. X-1 (4U 1908+005)	1.8	19	MS K-IV	$0.45 \div 0.8^a$	C08
SAX J1748.9–2021	2.3	8.7	MS	0.1	A08
New in NGC 6440	4.9	$0.7 \div 1.17$	–	–	A09
IGR J17511–305	4.1	3.5	–	0.13	M09

Table 1.1: Parameters of AMXPs. The fourth column indicates the star classes which companions, most likely, belong to: DD = Degenerate Dwarf, WD = White Dwarf, BD = Brown Dwarf, MS = Main Sequence star. The fifth column indicates the companion minimum masses, obtained by the mass function for  $\sin i = 1$ , hence for an inclination of  $90^\circ$ .

The process of mass transfer in a binary, obviously, changes its mass ratio  $q$  and, consequently, the orbital period,  $P_{orb}$ , and the separation,  $a$ , because of the redistribution of the angular momentum within the system. Since the Roche geometry is determined by  $a$  and  $q$ , it is important to ask whether the effect of these changes is to shrink or swell the Roche lobe of the mass-losing star. In the former case, the lobe overflow process will be self-sustaining at least for some time; in the latter case the mass transfer will switch off unless some effect, such as the nuclear evolution of the mass losing star, can increase its radius at a sufficient rate. The key quantity for these questions is the

orbital angular momentum  $J_b$ :

$$J_b = M_1 M_2 \sqrt{\frac{G a}{M}}, \quad (1.15)$$

where  $M = M_1 + M_2$  is the total mass of the system.

Following the approach of Verbunt (1993), the evolution can proceed along two different paths depending on whether the mass transfer is conservative or non-conservative.

### Conservative case

If the mass transfer is conservative, all the mass lost by the secondary is accreted by the primary, so that  $\dot{M}_1 + \dot{M}_2 = 0$  and  $\dot{M}_2 < 0$ .

Then logarithmically differentiating the Eq. 1.15 with respect to time, we obtain:

$$\frac{\dot{a}}{a} = \frac{2\dot{J}_b}{J_b} - \frac{2\dot{M}_2}{M_2} \left(1 - \frac{M_2}{M_1}\right). \quad (1.16)$$

Conservative mass transfer is characterized by constant binary mass and angular momentum; setting  $\dot{J}_b = 0$  in Eq. 1.16 and remembering that  $\dot{M}_2 < 0$ , we see that binary shrinks ( $\dot{a} < 0$ ) if conservative mass transfer takes place from the more massive to the less massive star. Conversely, if the mass transfer takes place from the less massive to the more massive, binary expands. Since the Roche lobe size is affected by the change in mass ratio as well as the separation, taking the logarithmic time derivative of Eq. 1.2, we obtain:

$$\frac{\dot{R}_{L_2}}{R_{L_2}} = \frac{\dot{a}}{a} + \frac{\dot{M}_2}{3M_2}, \quad (1.17)$$

and combining with Eq. 1.16,

$$\frac{\dot{R}_{L_2}}{R_{L_2}} = \frac{2\dot{J}_b}{J_b} - \frac{2\dot{M}_2}{M_2} \left(\frac{5}{6} - \frac{M_2}{M_1}\right). \quad (1.18)$$

Setting again  $\dot{J}_b = 0$ , we can easily see that there are two cases, depending on whether  $q$  is larger or smaller than  $\frac{5}{6}$ . For  $q > \frac{5}{6}$ , conservative mass transfer shrinks the Roche lobe down on the mass-losing star and, unless the star can contract rapidly enough to keep its radius smaller than  $R_{L_2}$ , the outflow process will become very violent, proceeding on a dynamical or

thermal timescale depending on whether the star's envelope is convective or radiative. The outflow stops once the mass ratio is reversed. This process certainly results short-lived to be typical of the mass-exchanging binaries we do observe, which must therefore correspond to the case  $q \lesssim \frac{5}{6}$ . In this case Eq. 1.18 shows that mass transfer will expand the Roche lobe of the mass-losing star. Mass transfer therefore only continues if either the star expands, or the binary loses angular momentum. The first case occurs when the secondary star evolves off the main sequence (MS): its radius will expand on a nuclear timescale,  $\tau_{\text{nuc}}$ , determined by hydrogen shell burning. The star can never greatly exceed its Roche lobe as mass is then lost on a dynamical timescale, so the lobe too will expand on the timescale  $\tau_{\text{nuc}}$ .

### Non-conservative case

The non-conservative case considers that:

- mass is lost from the binary,

$$\dot{M}_1 = -\beta\dot{M}_2 \quad \text{or} \quad \dot{M}_1 + \dot{M}_2 = (1 - \beta)\dot{M}_2;$$

- this mass carries angular momentum,

$$\frac{\dot{J}_M}{J} = \alpha(1 - \beta) \frac{M_1}{M_1 + M_2} \frac{\dot{M}_2}{M_2};$$

where we wrote the specific angular momentum of the mass that is lost as  $\alpha$  times the specific angular momentum of the mass-losing star.

In this way Eq. 1.16 may be replaced with:

$$\frac{\dot{a}}{a} = \frac{2\dot{J}}{J} - \frac{2\dot{M}_2}{M_2} \left[ 1 - \frac{\beta M_2}{M_1} - \frac{(1 - \beta)M_2}{2(M_1 + M_2)} - \alpha(1 - \beta) \frac{M_1}{M_1 + M_2} \right]; \quad (1.19)$$

where we indicated with  $\dot{J}$  other losses of angular momentum.

Eq. 1.19 displays the most general case of evolution driven by mass transfer in a binary system.

### Constraint on the orbital period from the donor mass

An approximate relation between orbital period and mass and radius of the Roche-lobe filling star ( $R_{L_2} = R_2$ ; with  $R_2$  the radius of the secondary star) can

be obtained by combining the third Kepler law, Eq. 1.1, with Eq. 1.2.

$$P_{\text{orb}} \simeq 8.9 \left( \frac{R_2}{R_\odot} \right)^{3/2} \left( \frac{M_\odot}{M_2} \right)^{1/2} \text{ hr.} \quad (1.20)$$

Considering the mass-radius relation for the donor star, Eq. 1.20 allows us to identify the orbital period as a function of the mass of the companion only.

### Evolution via angular momentum losses

A variety of effects can give  $\dot{J} < 0$ , the most important are:

*a.* emission of *gravitational radiation*, quite efficient in short systems;

*b.* *magnetic braking*, very meaningful for MS secondary stars.

*a.* This case was first analyzed by Kraft et al. (1962) and the loss of angular momentum via gravitational radiation may be written (Landau & Lifshitz 1975):

$$\left| \frac{\dot{J}}{J} \right|_{\text{GR}} = \frac{32G^3}{5c^5} \frac{M_1 M_2 (M_1 + M_2)}{a^4}. \quad (1.21)$$

It can be easily noticed that this process is more efficient in tighter orbits.

Now, considering a conservative ( $\beta = 0$ ) and stable ( $\dot{R}_{L_2} = \dot{R}_2$  and  $R_{L_2} = R_2$ ) mass transfer, and using the mass-radius relation of the secondary star,  $R_2 \propto M_2^n$ , Eq. 1.18 becomes:

$$-\frac{\dot{J}}{J} = -\frac{\dot{M}_2}{M_2} \left( \frac{5}{6} + \frac{n}{2} - \frac{M_2}{M_1} \right). \quad (1.22)$$

Combining Eq. 1.21 with Eq. 1.22 we may calculate the evolution of a LMXB. Fig. 1.4 (Verbunt 1993) shows results of this evolution for white dwarf, stars on the MS and on the helium MS.

For MS stars with masses between 0.2 and 1.2  $M_\odot$ , the mass transfer rate,  $\dot{M}$ , roughly stabilizes at the value of  $10^{-10} M_\odot \text{ yr}^{-1}$ .

Further evolution will lead the donor star to be less massive until it becomes too small to sustain significant hydrogen burning and the

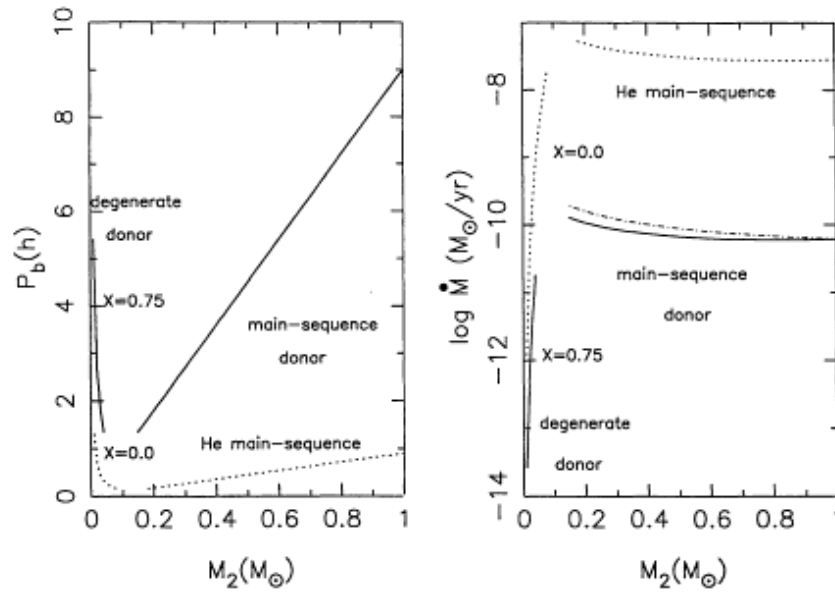


Figure 1.4: Orbital period (left) and mass-transfer rate (right) as a function of the donor mass,  $M_2$ , for binary evolution driven by angular momentum losses due to emission of gravitational radiation. For MS donors (solid and dashed lines for stars on the hydrogen and helium MS respectively), the orbital period decreases and the mass-transfer rate is roughly constant, as the donor mass decreases. The dash-dotted line indicates systems in which a half of matter lost by the donor star leaves the system,  $\beta = 0.5$ , with the specific angular momentum of the MS donor,  $\alpha = 1$ . Then, non-conservative mass transfer has roughly the same effect of the conservative one (Verbunt 1993).

core will become degenerate. Mass-radius relation for degenerate star reverses compared to that of MS star, then further mass loss causes it to expand. According to Eq. 1.20, the orbit will expand with it. Thus the evolution of the orbital period will pass through a minimum (Faulkner 1971), which is about 80 min (Paczynski & Sienkiewicz (1981), Rappaport et al. (1982)).

- b.* The other effect causing  $\dot{J} < 0$  is magnetic braking (MB). This mechanism is due to the anchorage of the particles of stellar wind to the magnetic field of the star, which forces them to corotate with the

star up to large distances from the surface. As the secondary is locked to the binary by the tidal forces, the secondary will not be able to rotate slower, and MB in a binary transfers the loss of angular momentum from the secondary to the binary system. The loss of binary angular momentum via MB from a MS donor in a binary system has been evaluated by Verbunt & Zwaan (1981):

$$\frac{j_{\text{mb}}}{J_{\text{b}}} = \frac{-3.8 \times 10^{-30} R_{\odot}^{4-\gamma} (M_1 + M_2) R_2^{\gamma} \Omega_{\text{b}}^2}{M_1 a^2}, \quad (1.23)$$

with  $\gamma = 4$ .

This mechanism is responsible for the enhancing of the mass transfer rate to higher values than  $10^{-10} M_{\odot} \text{ yr}^{-1}$ , as it can be shown substituting Eq. 1.23 in Eq. 1.22. In this way observations of a number of LMXB with luminosities in excess of  $10^{36} \text{ erg s}^{-1}$  ( $\equiv 10^{-10} M_{\odot} \text{ yr}^{-1}$ ) are well enlightened.

### 1.3.5 Disc accretion onto magnetized neutron stars

The description done in Sec. 1.2 about the mass transfer in a binary system can be relevant if the accretion disc extends right down the surface of the neutron star. Often this is not the case, as neutron stars possess a magnetic field of an order ( $10^{8-13} \text{ G}$ ) strong enough to disrupt the disc flow, as shown in Fig. 1.5. Even though interaction between disc and magnetic field is extremely complex, we can consider the rather simple case of an accretion flow which is quasi-spherical far from the star.

The magnetic field of a neutron star can be approximated to that of a magnetic dipole, whose intensity  $B$  is:

$$B \sim \frac{\mu}{r^3} \quad (1.24)$$

at a radial distance  $r$  from the neutron star of radius  $R_{\text{NS}}$ , where  $\mu$  is the magnetic moment. The magnetic pressure

$$\mathcal{P}_{\text{MAG}} = \frac{B^2}{8\pi} = \frac{\mu^2}{8\pi r^6}, \quad (1.25)$$

which increases steeply as the matter approaches the stellar surface, begins to control the matter flow and to disrupt the spherically symmetric in-fall

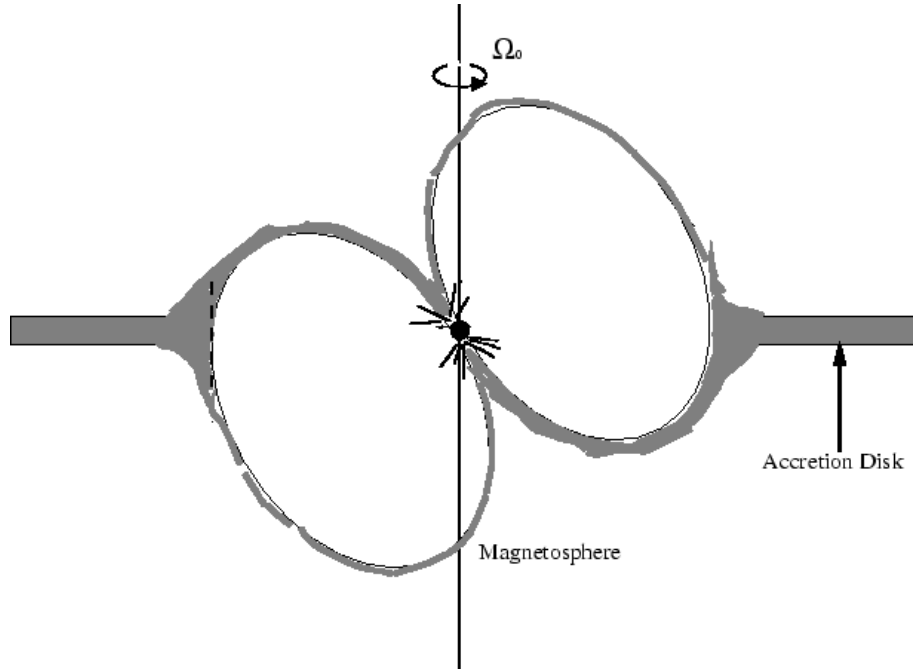


Figure 1.5: Disc accretion disrupted by the magnetic field of a neutron star. -  
<http://lheawww.gsfc.nasa.gov/users/audley/diss/node23.html>

at a radius  $R_A$ , where it first exceeds the gas ( $\mathcal{P}_{\text{gas}} = \rho c_s^2$ , with  $\rho$  and  $c_s$  the gas density and the sound velocity in this medium) and ram ( $\mathcal{P}_{\text{ram}} = \rho v^2$ , the inertia term) pressure of the matter. For highly supersonic accretion, as it is in the inner parts of the disc, the ram pressure is the prevalent term, hence the gas velocity,  $v$ , is supersonic and close to the free-free value,  $v_{\text{ff}} = (2GM_1/r)^{1/2}$ . Then, writing  $|\rho v|$  in terms of the accretion rate  $\dot{M}$ ,

$$|\rho v| = \frac{\dot{M}}{4\pi r^2}, \quad (1.26)$$

and equating the ram pressure to the magnetic pressure, Eq. 1.25, we obtain:

$$\frac{\mu^2}{8\pi r^6} = \frac{(2GM_1)^{1/2} \dot{M}}{4\pi r^{5/2}},$$

or:

$$\begin{aligned} R_A &= \mu^{4/7} \dot{M}^{-2/7} (2GM_1)^{-1/7} \\ &= 2.9 \times 10^8 m^{1/7} R_6^{-2/7} L_{37}^{-2/7} \mu_{30}^{4/7} \text{ cm}, \end{aligned} \quad (1.27)$$

which is known as the Alfvén radius and where  $L_{37}$  is the accretion luminosity in units of  $10^{37} \text{ erg s}^{-1}$  and  $\mu_{30}$  the magnetic moment in units of  $10^{30} \text{ G cm}^3$ . Within  $R_A$  we expect the matter flow will be totally governed by the magnetic field and channeled along its field-lines. But, this will happen if the torque exerted by the magnetic field on the disc is of the order of the viscous torques at a radius:

$$R_M \sim 0.5R_A, \quad (1.28)$$

called magnetospheric radius, even if the precise result depend on the inclination of the dipole axis to the disc plane.

From the above description clearly results that, under a stable accretion, the matter within  $R_M$  must follow the field lines, then their angular velocity must be lower than that of the matter,

$$\Omega_{\text{NS}} < \Omega_{\text{K}}, \quad (1.29)$$

where  $\Omega_{\text{K}}$  is the keplerian angular velocity, Eq. 1.3 (as the field lines corotate with the neutron star, and the matter is in keplerian orbit around the neutron star). However, if  $\Omega_{\text{NS}} > \Omega_{\text{K}}$  accretion is not allowed since matter would be pushed away by the centrifugal barrier in the so-called *propeller* phase.

Then, defining the corotation radius,

$$R_{\Omega} = \left( \frac{GM_1 P_S^2}{4\pi^2} \right)^{1/3} = 1.5 \cdot 10^8 P_S^{2/3} m^{1/3} \text{ cm}, \quad (1.30)$$

as the distance to the neutron star at which the keplerian velocity of the matter flow matches the spin velocity of the neutron star, an other way to require condition of Eq. 1.29 is:

$$R_{\Omega} \geq R_M. \quad (1.31)$$

Combining Equations 1.27 and 1.28, it can be shown that for typical parameters ( $m \sim R_6 \sim L_{37} \sim \mu_{30} \sim 1$ ) a magnetized neutron star will have  $R_A \sim R_M \sim 10^8 \text{ cm}$ , well outside the stellar radius. This means that the accretion flow near the neutron star surface is totally controlled by the magnetic field and a consequence is that the accreting matter is channeled onto the polar caps and then only on a little portion of star surface, as illustrated in Fig. 1.6. The in-falling matter, impacting on the star surface,

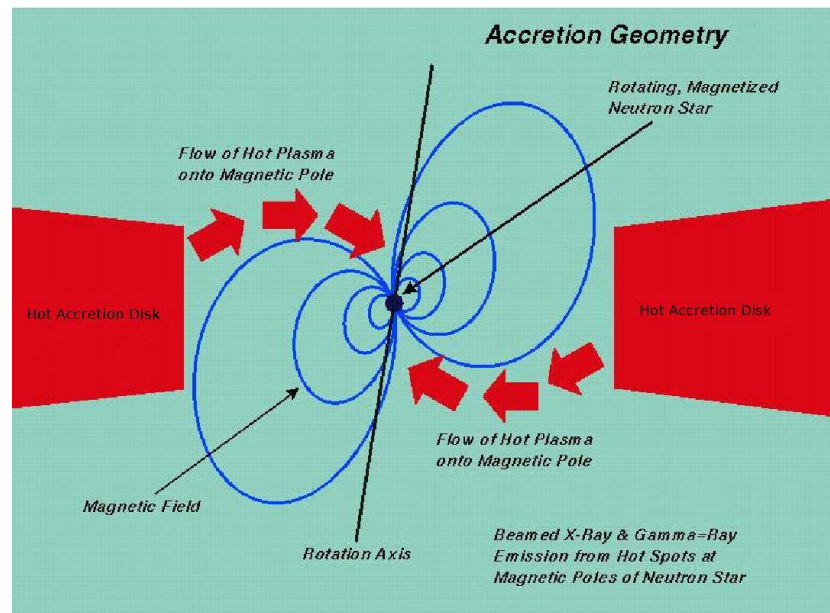


Figure 1.6: Artistic impression of accretion mechanism from a disc to the polar caps of a magnetized neutron star. - <http://www.astro.umd.edu/~miller/Gallery/compact/>

releases its gravitational energy in the form of X-rays, therefore every rotation of the accreting star will produce a periodic modulation in the observed flux at the spin period of the neutron star.

## 1.4 Rotation-powered millisecond pulsars

When the first type of pulsars was discovered, rotation-powered pulsars were originally known simply as pulsars, a term coined as a contraction of "pulsating star", although it was soon learned that the pulses were related to rotation rather than to physical expansion and contraction, as in true pulsating variable stars.

After the discovery of accretion-powered X-ray pulsars, rotation-powered pulsars were known as radio pulsars and it was realized that their emission goes mainly in the high energy part of the spectrum (X and  $\gamma$  ray; emission in radio band is just  $10^{-6}$  of the overall energy budget), and

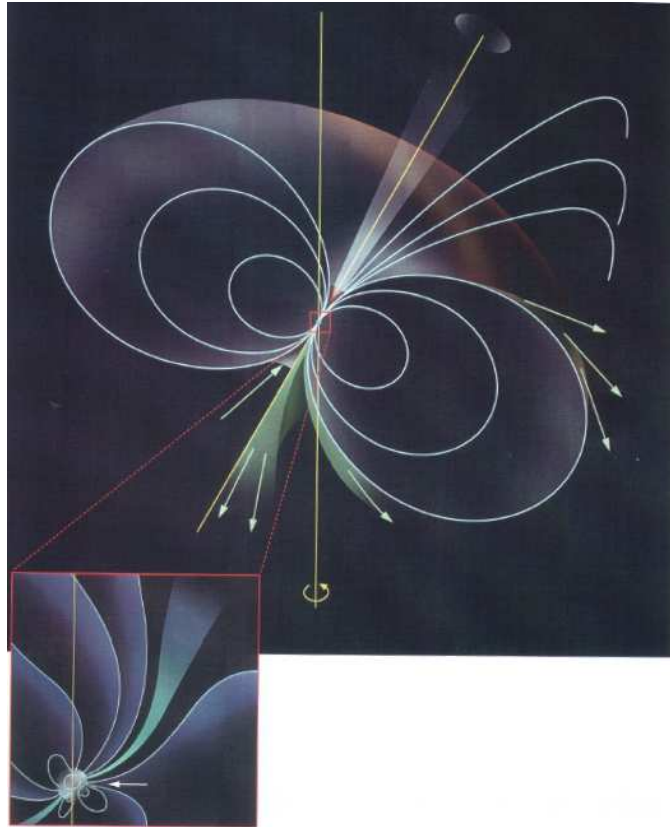


Figure 1.7: Artistic impression of the radio pulsar geometry. - [http://www.iasf-milano.inaf.it/Divulgazione/divulgazione/doc/pulsazioni\\_del\\_cielo\\_02.pdf](http://www.iasf-milano.inaf.it/Divulgazione/divulgazione/doc/pulsazioni_del_cielo_02.pdf)

when pulsars not emitting in the radio band were also discovered, the more physically motivated term “rotation-powered” started to be adopted; in fact, in addition to radio-loud pulsars, this last group includes radio-quiet systems like:

- the X-ray dim isolated NSs (XDINs), a group of seven soft X-ray sources originally discovered by the ROSAT satellite;
- the central compact objects (CCOs), isolated NS at the center of young ( $\sim 0.3 - 20$  kyears old) supernova remnants;
- the Geminga-like sources, NSs emitting X and gamma rays.

The emission site of the radio rotation-powered pulsars is most likely

concentrated on the magnetic polar caps of the neutron star. Magnetic and rotational axis are misaligned and this produces the observed pulsation, an artistic impression showing the geometry of these systems is displayed in Fig. 1.7.

The radio spectra of pulsars is a power law:  $S = \nu^{-\alpha}$ , where  $S$  is the flux density,  $\nu$  is the frequency and  $\alpha$  is the spectral index, generally between 1 and 3, but in average equal to  $\sim 1.7$ .

Radio rotation-powered pulsars can be subdivided in two main groups:

- the long period pulsars: with periods ranging from  $\sim 0.1$  to 8 seconds, magnetic fields  $B \sim 10^{11} - 10^{13}$  G and duty cycles (i.e. the duration of the pulse over the period) typically 1 – 5%;
- the millisecond (or recycled) pulsars: with periods  $P_s \leq 10$  ms, magnetic fields in the range  $10^8 - 10^9$  G and duty cycles from  $\sim 5\%$  up to  $\sim 30\%$ ;

Another class of pulsars is that of the magnetic-powered pulsars (magnetars), NSs with very strong magnetic fields  $B \gtrsim 10^{14}$  G; anomalous X-ray pulsars (AXPs) and soft gamma repeaters (SGR) belong to this pulsars class.

These groups can be visualized in the diagram of Fig. 1.8.

#### 1.4.1 Electrodynamics and radio emission properties

Since the magnetic axis of a radio pulsar is not aligned with its rotational axis, the neutron star magnetic dipole moment is time-varying and thus the star radiates a significant amount of energy in the form of electromagnetic waves at the rotation frequency  $\Omega_{\text{NS}}$  whose power is expressed by the Larmor's formula:

$$\dot{E}_{\text{dip}} = -\frac{2}{3} \frac{\mu_{\perp}^2 \Omega_{\text{NS}}^4}{c^3}, \quad (1.32)$$

where  $\mu_{\perp} = \mu \sin^2 \alpha$  is the component of the dipole moment perpendicular to the rotational axis.

This energy emitted by magneto-dipole radiation make the star to spin

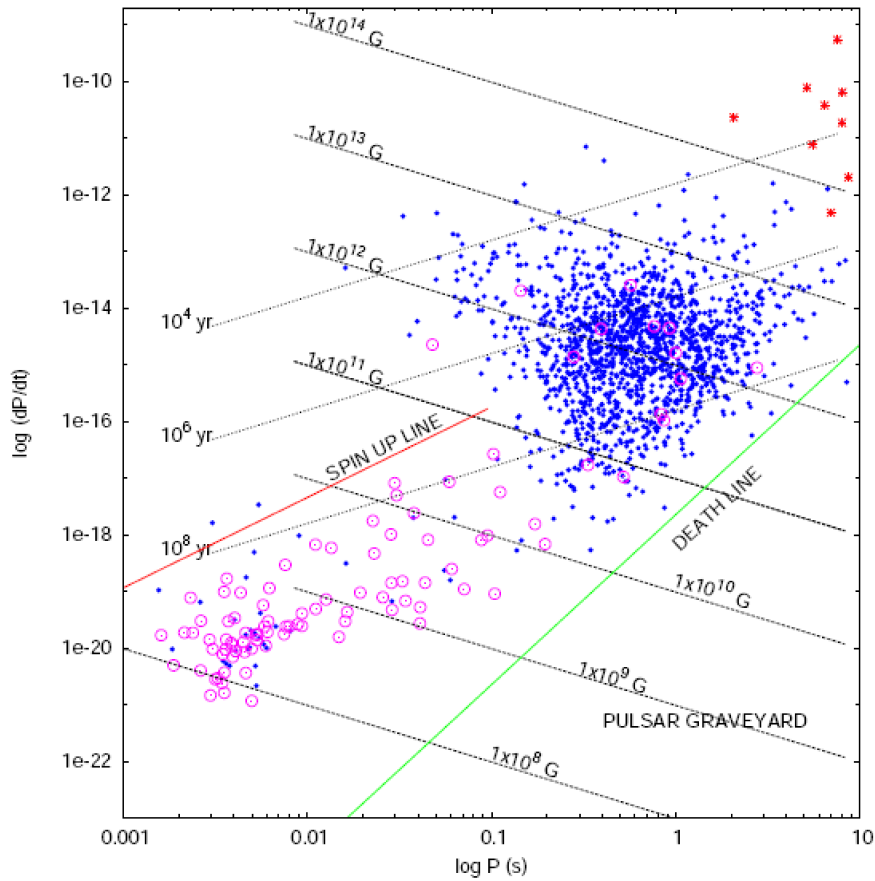


Figure 1.8: Diagram of spin period derivative versus spin period for the about 1800 pulsars discovered so far, as from the pulsar catalogue at <http://www.atnf.csiro.au/research/pulsar/psrcat/>. Red asterisks are the magnetic-powered pulsars (AXP and SGR), blue points are isolated rotation-powered pulsars and magenta circles refer to rotation-powered pulsars belonging to binary systems. The green and red solid lines represent the so-called *spin-up* and *death* lines (see Sec. 1.5). Isochrone (spin down age, see Sec. 1.4.1) and constant magnetic field lines are also plotted as dotted and dashed lines respectively.

down, losing its rotational energy:

$$\dot{E}_{\text{rot}} = I\dot{\Omega}_{\text{NS}}\Omega_{\text{NS}} = I\frac{\dot{P}_{\text{S}}}{P_{\text{S}}^3}, \quad (1.33)$$

where  $I$  is the moment of inertia of the star ( $\sim 10^{45}$  g cm<sup>2</sup>) and  $\dot{\Omega}_{\text{S}}$  is the

derivative of the spin frequency. Equating Eq. 1.32 and Eq. 1.33 and being  $\mu \sim Br^3$ , we obtain an estimate of the surface magnetic field of the neutron star in terms of its spin period  $P_S = 2\pi/\Omega_{NS}$  and the spin period derivative  $\dot{P}_S$  (Goldreich & Julian 1969):

$$B_{NS} = \sqrt{\frac{3c^3 I}{8\pi^2 R_{NS}^6} P_S \dot{P}_S} \simeq 3.2 \cdot 10^{19} \sqrt{\dot{P}_S P_S} \quad \text{G}, \quad (1.34)$$

where we adopted as typical values for neutron stars:  $R_{NS} = 10^6$  cm,  $\sin \alpha = 1$ .

One of the most commonly accepted models for the radio emission mechanism of pulsars, the polar-cap model (Ruderman & Sutherland 1975), predicts that the presence of the high magnetic fields ( $B \sim 10^8 \div 10^{13}$  G) in a fast spinning object produces an electric field so intense that it extracts charged particles from the neutron star surface. These particles are forced to corotate with the field lines of the magnetic field in the space surrounding the neutron star within the so-called *light-cylinder* radius:

$$R_{lc} = \frac{c}{\Omega_{NS}}. \quad (1.35)$$

Beyond this radius the speed of the particles attached to the field lines would be greater than the speed of light: the field lines must hence be open.

Considering the equation that describes the magnetic field lines of a dipolar field,  $(\sin^2 \theta)/r = \text{const}$ , we can derive the angle,  $\theta_m$ , that defines the closed magnetosphere delimiting a conal-like set of field lines:

$$\frac{\sin^2 \theta_m}{R_{NS}} = \frac{\sin^2 (90^\circ)}{R_{lc}}$$

and then:

$$\sin \theta_m = \sqrt{\frac{R_{NS}}{R_{lc}}} = \sqrt{\frac{2\pi R_{NS}}{c P_S}}. \quad (1.36)$$

Since the only charges that contribute to the radio emission are those which follow the open field lines, the radiation must result collimated within two conal beams of width  $\theta_m$ . Then, as magnetic and rotation axes are not aligned, the resulting emission is that of two lighthouse-like beams sweeping the surrounding space.

### The pulsar age estimate

The evolution of the spin period  $P_S$  of a pulsar can be expressed through the relation:

$$\dot{P}_S = KP_S^{2-n}, \quad (1.37)$$

where  $K$  is usually assumed to be constant and  $n$  is the so-called *braking index*, equal to 3 for pure magnetic dipole braking. Integrating this equation for  $n \neq 1$ , we can obtain an estimate for the age of the pulsar:

$$T = \frac{P_S}{(n-1)\dot{P}_S} \left[ 1 - \left( \frac{P_0}{P_S} \right)^{n-1} \right], \quad (1.38)$$

where  $P_0$  is the spin period at the birth. For long period pulsars we can assume that the spin period at the birth is much shorter than the present value (i.e.  $P_0 \ll P_S$ ) and the spin-down is due only to magnetic dipole radiation (i.e.  $n = 3$ ); in this way Eq. 1.38 simplifies into the *characteristic age*,  $\tau_c$ :

$$\tau_c \approx \frac{P_S}{2\dot{P}_S} \simeq 15.8 \text{ Myr} \left( \frac{P_S}{\text{s}} \right) \left( \frac{\dot{P}_S}{10^{-15}} \right)^{-1}. \quad (1.39)$$

The age evaluated in this way results overestimated for millisecond pulsars. In fact, for these sources the assumption that  $P_0 \ll P_S$  drops out.

### 1.4.2 The signal shape

Pulse shape is highly variable from pulse to pulse but the integrated profile (averaged over few hundreds of cycles) is extremely stable (Fig. 1.9).

The observed pulse shapes, because of the interaction between the broad band radio signal and the interstellar medium (ISM), usually appear different from the emitted pulses. The principal effects of the ISM on the radio emission are the dispersion and the scattering of the pulsed signal both producing a broadening of the pulse profile.

#### Dispersion

The dispersion effect on the radio signal is due to the fact that the group velocity,  $v_g$ , of the radio wave depends on the emission frequency,  $\nu$ , of the

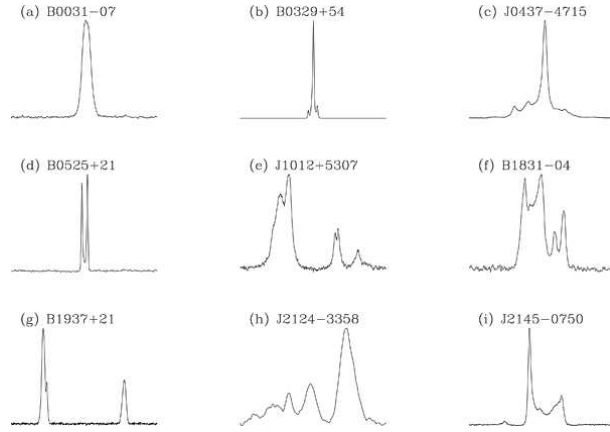


Figure 1.9: Examples of integrated pulse profiles for different pulsars, freely available from the online database: <http://www.jb.man.ac.uk/research/pulsar/Resources/epr/browser.html>.

signal:

$$\mathbf{v}_g = c \sqrt{1 - \left(\frac{\nu_p}{\nu}\right)^2}, \quad (1.40)$$

where  $c$  is the light velocity and  $\nu_p$  is the plasma frequency:  $\nu_p = \sqrt{e^2 n_e / \pi m_e} \sim 10$  kHz, below which the signal is totally absorbed by the medium, with  $e$ ,  $n_e$  ( $\approx 1 \text{ e}^- \text{ cm}^{-3}$ , typical of the ISM) and  $m_e$  the charge, the numerical density and the mass of electrons respectively.

For a frequency  $\nu \gg \nu_p$  we can write the group velocity as:

$$\mathbf{v}_g = c \left[ 1 - \frac{1}{2} \left(\frac{\nu_p}{\nu}\right)^2 \right] \quad (1.41)$$

and the time taken by a signal with a frequency  $\nu$  to reach an observer at a distance  $d$  will result:

$$t = \int_0^d \frac{dl}{\mathbf{v}_g} \approx \int_0^d \frac{1}{c} \left[ 1 + \frac{1}{2} \left(\frac{\nu_p}{\nu}\right)^2 \right] dl = \frac{d}{c} + \frac{1}{2} \frac{e^2}{\pi m_e c \nu^2} DM, \quad (1.42)$$

where  $DM = \int_0^d n_e dl$  is the *Dispersion Measure* which represents the column density of free electron in the direction of the source.

Since the radio observations are made over a broad band, the dependence of  $t$  on the frequency produces a broadening  $\Delta t_{DM}$  of the pulse

profile:

$$\Delta t_{\text{DM}} = \frac{e^2}{2\pi m_e c} \left( \frac{1}{\nu_1^2} - \frac{1}{\nu_2^2} \right) DM \approx 8.3 \cdot 10^3 \frac{\Delta \nu_{\text{MHz}}}{\nu_{\text{MHz}}^3} DM \quad \text{s}, \quad (1.43)$$

where  $\nu_{\text{MHz}}$  and  $\Delta \nu_{\text{MHz}}$  are the central observing frequency and the total bandwidth in MHz respectively and  $DM$  is given in  $\text{pc cm}^{-3}$ .

In order to minimize this effect it is necessary to subdivide the band pass of the receiver of a radio telescope in several channels of frequency width  $\delta \nu$ ; in each one of these channels the dispersion effect will be reduced and the signal in the different channels appears as in Figure 1.10, with the pulses arriving in each channel at a different time. In this way we have the so-called *pulse drift*.

Through the knowledge of the  $DM$  we can correct for this drift, integrating the signal over the whole bandwidth following the line joining the pulse peaks in the several channels (*dedispersion* of the signal) and obtaining a sharp and high signal-to-noise profile.

Since the  $DM$  is not *a priori* known, to obtain an estimate for known objects not observed in radio (e.g. NSs detected in x-rays in SNRs or in GCs) we refer to the models for the free electrons in the medium as those developed by Taylor & Cordes (1993) and Cordes & Lazio (2002). In fact, having an estimate the distance of the source (for example for near pulsars with the parallax method or for pulsars in the globular clusters), from these models we can derive an estimate of the  $DM$  and perform a search in a range centered in this estimate. Naturally, the dispersion measure of a pulsar is not known before its discovery, hence the search of new pulsars requires to explore a wide interval of DMs.

### Scattering

The second effect of the ISM on the radio emission is that of the scattering: because of the inhomogeneities in the ISM, the signal emitted from a pulsar interacts with clumps of matter and the radio waves follow different paths (Fig. 1.11) and arrive at the observer at different times, thus producing a broadening  $\delta t_{\text{scatt}}$  of the pulse, which, according with the “thin screen” model (see e.g. Lorimer & Kramer (2004)), scales as:

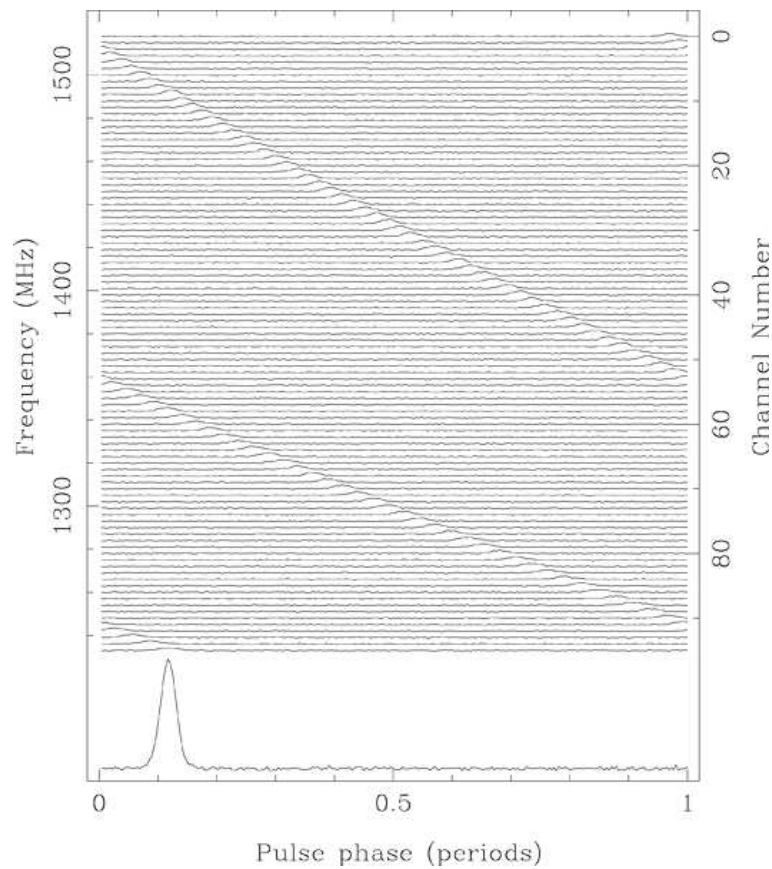


Figure 1.10: The typical pulse drift of a radio signal crossing the ISM. - [http://relativity.livingreviews.org/Articles/lrr-2008-8/fig\\_6.html](http://relativity.livingreviews.org/Articles/lrr-2008-8/fig_6.html)

$$\delta t_{\text{scatt}} \propto \frac{d^2}{\nu^{4.4}}. \quad (1.44)$$

Conversely to the case of the dispersion, no corrections can be made for the scattering effect on the observed time series, the only possibility to lessen the resulting broadening is to observe at high frequency. The choice of the observing frequency, hence, is a crucial point in any observational campaign.

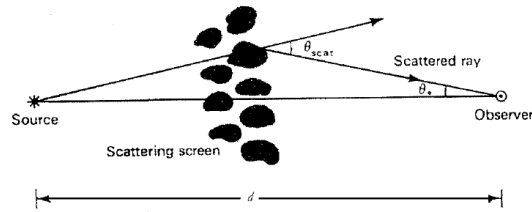


Figure 1.11: Schematic representation of the effect of the interstellar scattering on the photons emitted by a source.

## 1.5 Standard evolutionary link between accretion-powered and rotation-powered millisecond pulsars

### 1.5.1 Evolution of isolated rotation-powered pulsars

According to what depicted in Sec. 1.4.1 we can follow the evolution of an isolated pulsar using the  $P_S - \dot{P}_S$  diagram of Figure 1.8 which we report here for convenience (Fig. 1.12).

The formation of a pulsar is due to the supernova explosion; during this event, the core of a massive star is compressed and retains most of its angular momentum and magnetic flux. Thus the newly born neutron star is rapidly spinning and has a high magnetic field strength ( $\sim 10^{12} \div 10^{13}$  G), hence, according to Eq. 1.34, it has a high value of  $\dot{P}_S$ , placing it in the top-left side of the  $P_S - \dot{P}_S$  diagram.

As discussed in Sec. 1.4.1, during their evolution, pulsars slow down losing their rotational energy and move rightwards in the diagram, following the constant  $B$  field lines, or slightly turning downwards if the magnetic field decays, (cyan arrow in Fig. 1.12). The time scale to complete this step of evolution is very rapid because of the very low spin period and the very high values of the magnetic field and, then, of the spin period derivative. This is evident in the  $P_S - \dot{P}_S$  diagram as the most part of rotation-powered pulsars are in the right side.

When the pulsar crosses the so-called *death-line*, the green line in Fig. 1.12, the emission mechanism is no more efficient and the radio pulsar

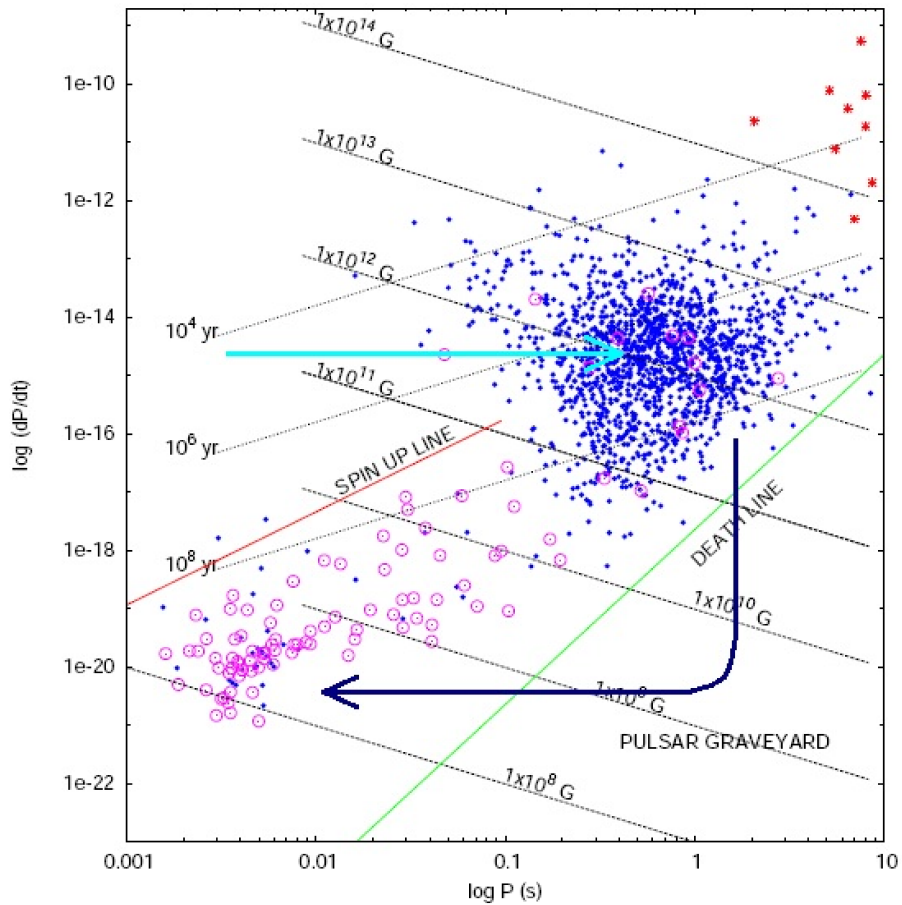


Figure 1.12:  $P_S - \dot{P}_S$  diagram. The evolution of an isolated pulsar follows the cyan arrow. Its spin period increases until it crosses the death line. Spin up line is drawn for Eddington rate mass transfer and for standard values of all the parameters.

switches off, joining the pulsars *graveyard*.

### 1.5.2 Evolution of binary pulsars: the *recycling* model

When a pulsar is part of a binary system with a low mass companion, the evolution can be different from the scenario depicted above. In fact after the crossing of the death-line, a neutron star in a binary can undergo accretion of matter and angular momentum from the companion star with the formation of an accretion disk, as we have already discussed in Sec. 1.3.4.

During this accretion phase the neutron star is visible as X-ray source,

its period decreases (the star is spun-up by angular momentum transfer) and its magnetic field decays probably because of the accretion itself (see e.g. Geppert & Urpin (1994) and Jahan Miri (1996)). In the  $P_S - \dot{P}_S$  diagram this corresponds to a shift towards the bottom-left part, as represented by the blue arrow in the plot of Fig. 1.12.

The minimum spin period achievable by the neutron star is the equilibrium period (Ghosh & Lamb 1992):

$$P_{\text{eq}} = 0.95 \text{ sec } \zeta^{3/2} \mu_{30}^{6/7} \dot{m}_e^{-3/7} \kappa_{0.4}^{3/7} R_6^{-3/7} M_{1.4}^{-5/7}, \quad (1.45)$$

where  $\dot{m}_e$  is the mass accretion rate in units of the Eddington rate (spherical accretion is assumed),  $\kappa_{0.4}$  is the opacity of the accreting material in units of  $0.4 \text{ cm}^2 \text{ g}^{-1}$  (the Thomson opacity for ionized hydrogen),  $M_{1.4}$  is the neutron star's mass in units of  $1.4 M_\odot$  and  $\zeta \equiv \xi/\omega_s^{2/3}$  is of order unity, where  $\xi \sim 0.5$  incorporates uncertainty in the Alfvén radius and  $\omega_s \leq 1$  is the fastness parameter (see e.g. Frank et al. (2002)).

Eq. 1.45 and Eq 1.34 define the spin-up line showed as the red line in Fig. 1.12:

$$\begin{aligned} \dot{P}_S &= \alpha P_S^{4/3}, \\ \alpha &= 1.10 \times 10^{-15} \eta \zeta^{-7/2} \dot{m}_e \kappa_{0.4}^{-1} R_6 M_{1.4}^{5/3} I_{45}^{-1}, \end{aligned} \quad (1.46)$$

where  $\eta \leq 1$  is a geometrical factor,  $P_S$  is in seconds, and  $I = I_{45} 10^{45} \text{ g cm}^2$ . It is now clear that the endpoint of spin-up by accretion depends from the accretion rate, limited by the Eddington limit (see Sec. 1.3.1).

Depending on the mass of the companion and hence on the duration of the mass transfer phase (generally about  $10^7 \div 10^9$  years), at the end of the accretion the spin period can reach values of the order of millisecond and magnetic field decays to values between  $\sim 10^8$  and  $\sim 10^9$  G, and they can be such that the neutron star is again above the death line, and then able again to emit radiation in the radio band.

The objects formed in this way are called *recycled* or *millisecond* (because of their short spin period) pulsars and the model describing their formation is the so-called *recycling* model, developed by Ali Alpar and collaborators (Alpar et al. 1982). This model argues that progenitors of recycled pulsars are the LMXBs, binary systems which, during the accretion phase via Roche

lobe overflow are visible as X-ray sources. However, the radio emission from a recycled pulsar is possible only if the surrounding space is free of matter, i.e. if the matter released from the companion is beyond the light cylinder radius,  $R_{lc}$ .

$$R_M \geq R_{lc}. \quad (1.47)$$

This occurs in transiently accreting systems during their quiescence phases.

In fact during the first stage of quiescence, the magnetospheric radius  $R_M$ , depending on  $\dot{M}^{-2/7}$ , considerably increases its sizes. Consequently the spin velocity of the magnetic field lines at  $R_M$  becomes higher than the keplerian velocity, establishing the propeller phase. At this point, the accretion luminosity notably decays (Burderi et al. 2001), and we observe drastic variations in the time and spectral profiles (Gilfanov et al. 1998).

Meanwhile the magnetospheric radius becomes larger than the light cylinder radius allowing the possibility for the radio emission to switch on.

Although in principle this alternance of X-ray and radio pulsed emission may occur in a broad class of X-ray transient binaries, a particularly interesting case of study is that of the AMXPs (see Sec. 1.3.3). In fact in these systems we precisely know the spin period of the accreting object and it results in the millisecond range, favoring these binaries as natural progenitors of at least a subsample of the rotation-powered millisecond pulsars.

### 1.5.3 Magnetic evolution in accreting binary NSs

The evolution of the magnetic field in a NS undergoing accretion processes is not well understood so far. Observative evidences show that, the majority of the known NS population, i.e. the non-recycled pulsars (with spin periods higher than tens of millisecond), have an average dipole field strength at the surface of  $\sim 10^{12}$  G, while the field strengths of the radio MSPs are at least three orders of magnitude lower than this value ( $\sim 10^8$ – $10^9$  G). Indirect measurements of the surface magnetic field in AMXPs, thought to be progenitors of at least a subsample of the radio MSPs, provide a low value ( $< 10^{10}$  G). Moreover, as it can be shown in Fig. 1.13, magnetic fields of binary

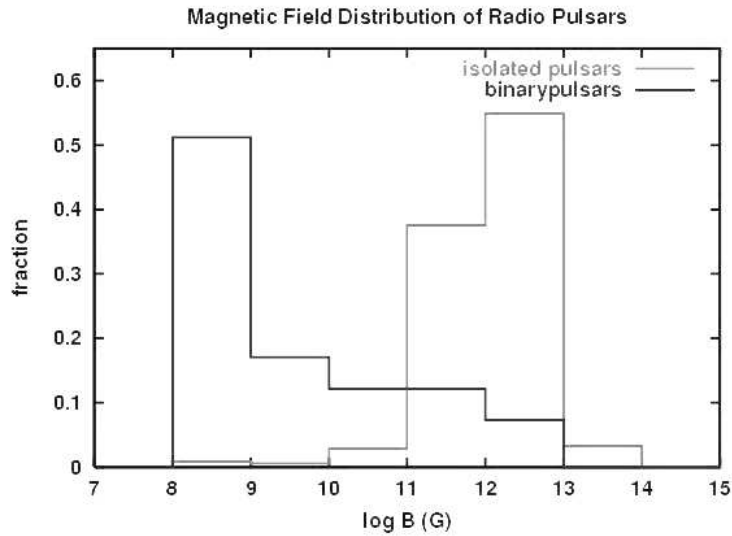


Figure 1.13: Normalized distribution of the magnetic field strengths of isolated radio pulsar (black line) and those in binary system (gray line). The peak of the field distribution of pulsars in binaries lies at  $\sim 10^8$  G, about four orders of magnitudes below that of isolated pulsars.

NSs are much lower than those of the isolated pulsar population, suggesting that evolution in a binary system causes the magnetic field of a NS to decay.

In this section we briefly review some of the most important models trying to explain the decay of the magnetic field in accreting NS, which have been proposed over the years.

### Tectonic processes

This model (see e.g. Sauls (1989), Jahan Miri & Bhattacharya (1994)) argues the possibility that the spin evolution of the NS is coupled with its magnetic evolution.

If the magnetic field of the NS is initially distributed through its core, then, in the superfluid-superconducting interior of the star, the magnetic flux will be carried by quantized proton fluxoids. As suggested by Srinivasan et al. (1990), as the star spins down (mainly during the spin-down propeller phase), they will be dragged out and the associated flux will be deposited in

the NS crust. This deposited flux could then undergo ohmic decay.

A different consequence of fluxoids dragging has been explored by Ruderman (1991). The stress on the fluxoids would be transmitted to their foot points anchored in the inner crust, causing cracking and migration of crustal plates. The movement of the crustal plates bearing the magnetic poles can cause secular change in the magnetic field of the NS, lowering the magnetic dipole moment.

This mechanism predicts magnetic dipole axis to be either fully aligned or, more commonly, orthogonal to the spin axis in millisecond pulsar population. It also predicts that the accretion onto such stars will produce hot spots very close to the rotational poles, which seems to be required to explain some of the behaviour seen in AMXPs (Poutanen 2008).

### Ohmic processes

The Ohmic model works only for magnetic fields confined to the crust of the NS. If the field is originally in the interior, then it needs to be expelled to the crust, possibly due to the so-called vortex-fluxoid coupling in the superfluid-superconducting interior. Once the field is in the crust, the heating due to accretion can cause accelerated ohmic decay, while the accreted overburden leads to its eventual freezing to a bottom value (Konar & Bhattacharya 1997, 1999). A correlation between the average mass accretion rate and the residual field is predicted.

### Diamagnetic screening

One of the most popular models of the evolution of NS magnetic field is its screening by matter accreting on its surface (Bisnovatyi-Kogan & Komberg 1974). The main idea is that the accreting matter is a highly conducting, non-magnetized plasma. The matter arrives at the surface of the NS, guided by the stellar magnetic field to its magnetic polar caps. As the matter accumulates, gravity would cause it to spread sideways. In doing so, it will push magnetic field away, eventually burying it underneath. The field does not actually decay, but gets screened from the view of an outside observer. The *bottom field* in this picture has been linked to the loss of

magnetic guidance of accreting plasma flow at surface fields  $\lesssim 10^8$  G (Konar & Choudhuri (2004), Zhang & Kojima (2006)).

The popularity of this scenario stems from the relative simplicity of the idea, and the fact that the result is relatively independent of the distribution of the magnetic field inside the NS.

However the process is subject to numerous plasma instabilities, many of which need full investigation.

## **Chapter 2**

# **New evolutionary scenarios**

In this Chapter we discuss the evolutionary connection between LMXBs and radio MSPs in the framework of the recycling model and how the onset of the so-called radio-ejection mechanism can overcome the main difficulties of this model.

My work focuses on provide observational support to the radio-ejection mechanism by inspecting the orbital and spin parameters of the known population of fully recycled radio pulsars and compare these with the expectation for the occurrence of this mechanism.

## 2.1 Introduction

As we have already seen in Chapter 1, the recycling model argues the existence of an evolutionary connection between LMXBs, binary systems containing a low magnetized ( $B < 10^{10}$  G) NS accreting mass from a low mass ( $M < 1 M_{\odot}$ ) companion, and radio MSPs, asserting that LMXBs are progenitors of MSPs. In this evolutionary scenario, AMXPs, a subclass of LMXBs periodically showing accretion episodes with short phases of coherent pulsed X-ray emission, constitute a bridge between LMXBs and radio MSPs, being matter accretion during the AMXP phase the only way to attain the spin parameters suitable for a radio MSP to switch on.

AMXPs are transient systems, exhibiting quiescence phases, lasting periods of the order of years, in which their X-ray luminosity is in the range  $10^{31} \div 10^{34}$  erg s<sup>-1</sup>, and short (at most a few tens of days) outburst phases, in which their luminosity reaches  $10^{36} \div 10^{38}$  erg s<sup>-1</sup>, in the range 0.5-10 keV. This last stage is associated to the matter falling onto the NS surface, since X-rays are powered by the gravitational energy of the infalling matter, whose angular momentum spins up the NS to period of the order of millisecond.

Several attempts have been made in order to obtain a conclusive proof of recycling model (e.g. Burgay et al. (2003a)), but until very recently all of these have failed. In fact, in 2009 May, Archibald et al. detected radio pulsations at a period of 1.69 ms from the source PSR J1023–0038<sup>1</sup>, a NS binary around to which optical observations indicate that an accretion disk was present until

---

<sup>1</sup>FIRST J102347.67+003841.2 (Szkody et al. 2003).

2002, suggesting that the radio MSP has switched on after a recent phase of LMXB.

Despite the large number of supporting evidences for the recycling scenario, in the following we will highlight some surviving open issues of this model.

### 2.1.1 Open issues

Observations of the present population of MSPs provide some constraints on the parameters of the systems, that are not in line with the simple evolutionary scenario depicted above.

- The minimum observed spin period in the radio MSPs results larger than the critical limit for mass-shedding of a NS at its equator, so that there exist a gap of permitted spin period between that resulting from mass-shedding of the NS and that minimum observed, which is that of PSR J1748–2446ad (Hessels et al. 2006), the fastest spinning known MSP. Its spin period is  $P_s = 1.40$  ms, and the critical limit for the stability of an accreting NS is  $\approx 0.5$  ms (Cook et al. 1994) for most (but the ultra-stiff) equations of state of the ultra dense nuclear matter.
- The amount of mass accreted onto the NS in the AMXP phase results so large that the NS should attain the limit for the collapse to a black hole (BH). We can quantify the mass lost from the NS companion, evaluating that at the beginning of the accretion phase its mass is  $\sim 1.0 \div 2.0 M_\odot$  (Webbink, Rappaport & Savonije 1983; Tauris & Savonije 1999), while donor stars in binary systems containing a MSP have mass  $\sim 0.15 \div 0.30 M_\odot$  (Taam, King & Ritter 2000). Then, as the mass lost from the companion star results  $M_{\text{lost}} \sim 0.70 \div 1.85 M_\odot$ , which is the final mass that the NS should attain? A simple calculation leads to NSs with mass  $\sim 2.1 \div 3.2 M_\odot$  (values larger than the maximum allowed in most of soft equation of state) spinning at a period of  $\sim 0.3 \div 0.14$  ms (see Burderi, Possenti et al. 1999 and e.g. Cook et al. (1994)).

It is clear from the above considerations that we are facing a dilemma: is the equation of state for nuclear matter really ultra-stiff (implying NS as

massive as  $3 M_{\odot}$  and limiting spin periods of about 1.3 ms), or are there observational biases which prevent us from detecting systems containing a rapidly rotating NS, or there must be some mechanism able to explain this observational lack? In this paper we speculate on the third possibility, however the first and the second will be treated in less detail in the last part of this report.

## 2.2 The mechanism of “radio-ejection”

Several mechanisms have been proposed so far in order to give a possible solution to these theoretical issues, as e.g. constraints imposed by the dependence of the spin frequency from the energy losses due to the emission of gravitational radiation (Bildsten 1998).

However, in 2001, Burderi et al. proposed a model, which we revisit in this Section, able to explain the evolution of this kind of systems within the recycling scenario and allowing to clarify the aforementioned main issues.

During the AMXP phase, the mass in accretion via Roche lobe overflow, in attempt to reach the NS surface, has to push against the outward (from the NS in the radial direction) pressure of the rotating magneto-dipole. For  $r < R_{lc}$ , this outward pressure is mainly due to the dipolar magnetic field,  $B$ , and is:

$$\mathcal{P}_{MAG} = \frac{B^2}{8\pi} = 7.96 \times 10^{14} \mu_{26}^2 r_6^{-6} \quad \text{dy cm}^{-2}; \quad (2.1)$$

while, for  $r > R_{lc}$ , the radiation pressure of the rotating magneto-dipole is mainly acting, and is given by:

$$\mathcal{P}_{DIP} = 2.04 \times 10^{12} P_{-3}^{-4} \mu_{26}^2 r_6^{-2} \quad \text{dy cm}^{-2}. \quad (2.2)$$

The accretion flow, in turns, exerts an inward (toward the NS in the radial direction) pressure on the field, which, for a Shakura-Sunyaev accretion disk is:

$$\mathcal{P}_{DISK} = 1.02 \times 10^{16} \alpha^{-9/10} n_{0.615}^{-1} L_{37}^{17/20} m^{1/40} R_6^{17/20} f^{17/5} r_6^{-21/8} \quad \text{dy cm}^{-2}. \quad (2.3)$$

Where in these three Equations:  $\alpha$  is the Shakura-Sunyaev viscosity parameter,  $n_{0.615} = n_p/0.615 \sim 1$  for a gas with abundances of stars of

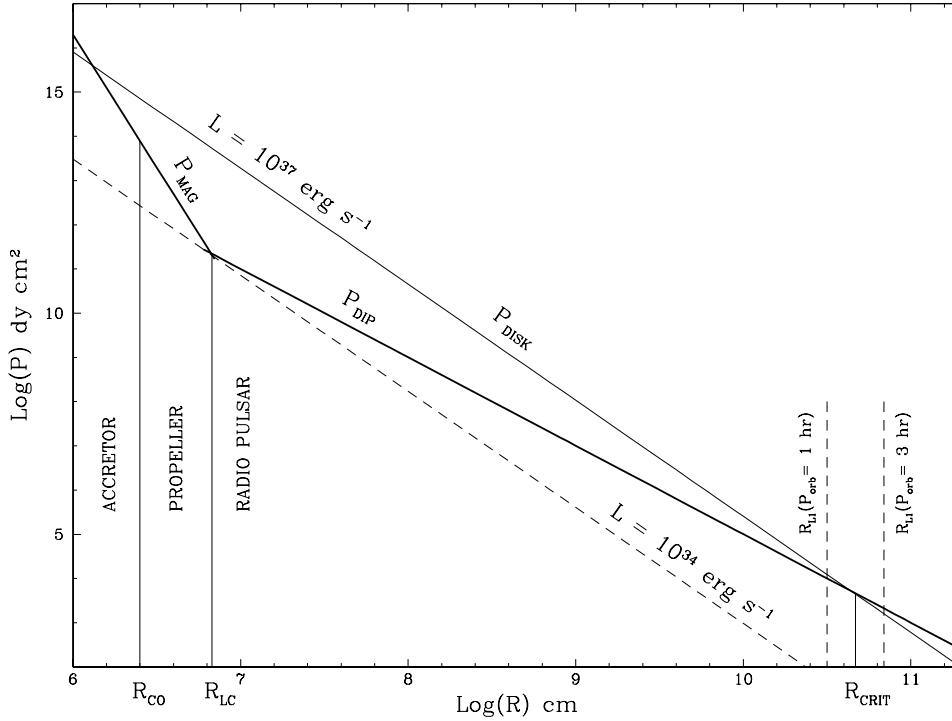


Figure 2.1: Radial dependence of the pressures relevant for the evolution of accreting and recycled NSs. The parameters adopted are:  $\mu_{26} = 5$ ,  $P_{-3} = 1.5$ ,  $\alpha = 1$ ,  $n_{0.615} = 1$ ,  $R_6 = 1$ ,  $m = 1.4$ ,  $f = 1$ .

population II (where  $n_p$  is the mean particle mass in units of the proton mass),  $L_{37}$  is the accretion luminosity in units of  $10^{37}$  erg  $s^{-1}$  that measures  $\dot{M}$  in the hypothesis that all the transferred mass accretes onto the NS,  $m$  is the NS mass in  $M_\odot$ ,  $r_6$  is the distance from the NS center in units of  $10^6$  cm,  $P_{-3}$  is the spin period in milliseconds,  $\mu_{26}$  is the magnetic moment of the NS in units of  $10^{26}$  G  $cm^3$  ( $\mu = B_s R^3$  with  $R$  and  $B_s$  NS radius and surface magnetic field along the magnetic axis, respectively), and  $f = [1 - (R_6/r_6)^{1/2}]^{1/4} \leq 1$ .

In Figure 2.1,  $\mathcal{P}_{DISK}$  is represented by the thin solid line for a value of the luminosity  $L_{max} = 10^{37}$  erg  $s^{-1}$ , corresponding to a high mass accretion rate, for a system with parameters:  $\mu_{26} = 5$ ,  $P_{-3} = 1.5$ ,  $\alpha = 1$ ,  $n_{0.615} = 1$ ,  $R_6 = 1$ ,  $m = 1.4$ ,  $f = 1$ . While the  $\mathcal{P}_{DISK}$  line passing across the point of intersection between  $\mathcal{P}_{MAG}$  and  $\mathcal{P}_{DIP}$  (bold solid lines), defines a critical

luminosity,  $L_{\text{switch}} = 10^{34} \text{ erg s}^{-1}$  (dashed line in Fig. 2.1), at which the radio pulsar can switch on.

As derived by Burderi et al. (2001a, b), the balance between the inward disk pressure,  $\mathcal{P}_{\text{DISK}}$ , and the outward radiation pressure at values of the distance larger than  $R_{\text{lc}}$  determines a strict classification of this kind of binary systems during their evolution. In fact, for a luminosity equal to  $L_{\text{max}}$  (equating Equations 2.3 and 2.2) a *critical* radius,  $R_{\text{crit}}$ , can be defined:

$$R_{\text{crit}} = 8.26 \times 10^{11} \alpha^{-36/25} n_{0.615}^{-8/5} R_6^{34/25} L_{37}^{34/25} m^{1/25} \mu_{26}^{-16/5} P_{-3}^{32/5} \text{ cm.} \quad (2.4)$$

$R_{\text{crit}}$  is a point of *unstable* equilibrium, where small fluctuations of  $\mathcal{P}_{\text{DISK}}$  can determine accretion, if  $\mathcal{P}_{\text{DISK}} \gtrsim \mathcal{P}_{\text{DIP}}$ , or ejection of matter, if  $\mathcal{P}_{\text{DISK}} \lesssim \mathcal{P}_{\text{DIP}}$ . However, it is clear that for  $r > R_{\text{crit}}$  no disk can exist for any luminosity less than approximately  $L_{\text{max}}$ .

The size of  $R_{\text{crit}}$  compared to that of the first Lagrangian point of the binary system,  $R_{L_1}$ , leads to a definition of two kinds of systems, *compact* and *wide*. As illustrated in Fig. 2.2, the firsts are those in which  $R_{L_1}$  lies inward  $R_{\text{crit}}$ , the opposite for the seconds.

Being  $R_{L_1}$  related to orbital parameters through the relation (Paczynski 1971):

$$R_{L_1} = 3.5 \times 10^{10} P_h^{2/3} (m + m_2)^{1/3} \left[ 1 - 0.462 \left( \frac{m_2}{m + m_2} \right)^{1/3} \right] \text{ cm,}$$

where  $P_h$  is the orbital period in hours and  $m$ ,  $m_2$  are the NS and the companion masses in  $M_{\odot}$ , at the equilibrium, for  $R_{\text{crit}}/R_{L_1} = 1$ , the *critical* period  $P_{\text{crit}}$  results to be the orbital period that separates compact and wide systems:

$$P_{\text{crit}} = 1.05 \times (\alpha^{-36} n_{0.615}^{-40} R_6^{34})^{3/50} L_{36}^{51/25} m^{1/10} \mu_{26}^{-24/5} P_{-3}^{48/5} \times \left[ 1 - 0.462 \left( \frac{m_2}{m + m_2} \right)^{1/3} \right]^{-3/2} (m + m_2)^{-1/2} \text{ hr,} \quad (2.5)$$

where  $L_{36}$  is the accretion luminosity in units of  $10^{36} \text{ erg s}^{-1}$ .

The behavior of these two classes of systems is quite different (see also Burderi et al. (2001) for a review). In the case of a compact system, the

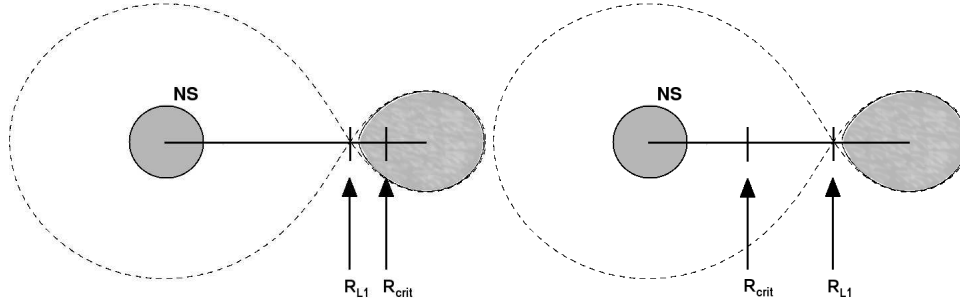


Figure 2.2: Left: case of a compact system,  $R_{\text{crit}}$  lies outside the Roche lobe of the NS, then the disk pressure,  $\mathcal{P}_{\text{DISK}}$ , in  $R_{L1}$  can overcome the radiation pressure of the radio pulsar,  $\mathcal{P}_{\text{DIP}}$ , starting the accretion phase. Right: case of a wide system, the critical radius,  $R_{\text{crit}}$ , lies inside the Roche lobe of the NS; when the luminosity attains its maximum value,  $L_{\text{max}}$ , in  $R_{L1}$  the disk pressure cannot overcome the radio pulsar radiation pressure, for any value of the luminosity less than approximately  $L_{\text{max}}$ , then the matter will be ejected from the system.

alternate of the luminosity (or its corresponding accretion rate) between its maximum,  $L_{\text{max}}$ , and minimum,  $L_{\text{min}}$ , value leads to a cyclic behavior, during which, at first, the NS normally accretes matter and angular momentum, thus increasing its spin velocity (accretion phase,  $\mathcal{P}_{\text{DISK}} > \mathcal{P}_{\text{DIP}}$ ). Afterward, when the luminosity drops to its minimum value, the radiation pressure prevents mass accretion, despite matter is still overflowing through  $L_1$ , and then mass will be ejected from the system ( $\mathcal{P}_{\text{DISK}} < \mathcal{P}_{\text{DIP}}$ ): we are facing the so-called *radio ejection* phase. These two phases follow one after the other during evolution, completing one or more cycles as shown in Figure 2.3, in which we considered a minimum luminosity  $L_{\text{min}} = 10^{33} \text{ erg s}^{-1} < L_{\text{switch}}$ . The complete cycle accomplished by a compact system is illustrated by the two bold dashed arrows, which identify the two phases of accretion (upper arrow) and radio-ejection (lower arrow).

In particular, during the outburst, the magnetospheric radius,  $R_M$  (delimiting the inner radius of the disk), is smaller than both the corotation and the light cylinder radius and the NS will normally accrete matter and

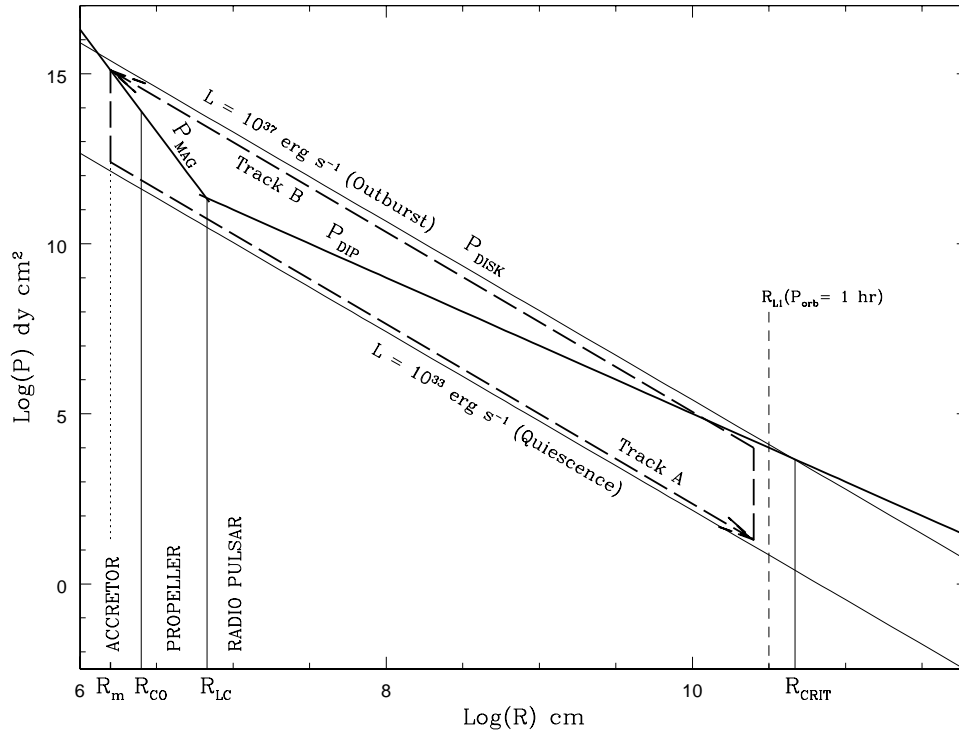


Figure 2.3: Radial dependence of the pressures relevant for the evolution of accreting and recycled NSs. Case of a compact system. The parameters adopted are:  $\mu_{26} = 5$ ,  $P_{-3} = 1.5$ ,  $\alpha = 1$ ,  $n_{0.615} = 1$ ,  $R_6 = 1$ ,  $m = 1.4$ ,  $f = 1$ .

angular momentum thus decreasing its spin period. The sudden drop in the mass-transfer rate, and then in the luminosity, (quiescence) initiates the radio-ejection phase, in which the mass overflow from the first Lagrangian point,  $L_1$ , is still going on, but the radiation pressure of the rotating magnetodipole prevents mass accretion. In fact, as the new pressure drops below  $\mathcal{P}_{\text{switch}}$  (defined as the disk pressure corresponding to the switch luminosity),  $R_M$  expands beyond  $R_{lc}$  and the radiation pressure,  $\mathcal{P}_{\text{DIP}}$ , becomes higher than the disk pressure pushing the disk away from the system until  $R_{L_1}$  is reached starting the radio-ejection phase (track A in Fig. 2.3).

When a new outburst occurs the mass transfer rate rises back to its original value (corresponding to  $L_{\text{max}} = 10^{37} \text{ erg s}^{-1}$ ), the disk follows track B, and accretion resumes.

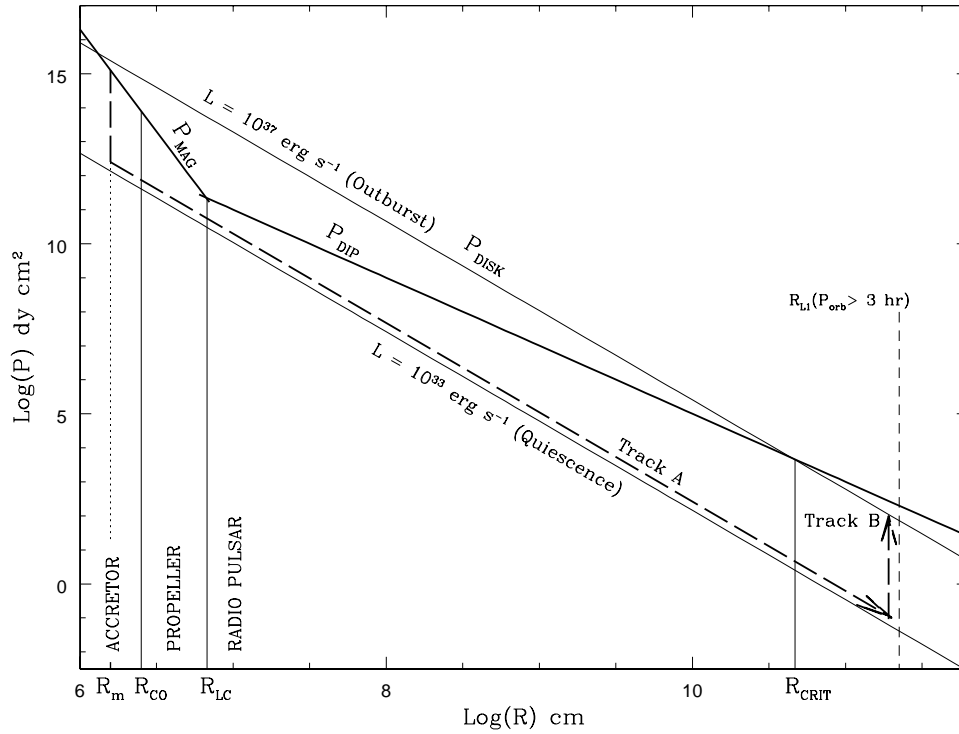


Figure 2.4: Radial dependence of the pressures relevant for the evolution of accreting and recycled NSs. Case of a wide system. The parameters adopted are:  $\mu_{26} = 5$ ,  $P_{-3} = 1.5$ ,  $\alpha = 1$ ,  $n_{0.615} = 1$ ,  $R_6 = 1$ ,  $m = 1.4$ ,  $f = 1$ .

The evolution of this kind of systems, is driven by gravitational radiation (GR) emission process (see Section 2.2.1) and leads the orbital period to values lower than those derived from the orbital evolution without loss of angular momentum (see Verbunt (1993)). On the other hand, the critical period, because of its rapid response to the variation of the spin period (which becomes lower in a cycle because of accretion), decreases as well and more quickly, being the dependence  $P_{\text{crit}} \propto P_{\text{S}}^{48/5}$ , until it matches the  $P_{\text{orb}}$  value and the system becomes part of the wide systems class.

The response of such last systems to the same variation of accretion rate is not cyclic, in fact when the luminosity recovers its maximum value, the accretion flow pressure cannot overcome the radiation pressure, and mass accretion onto the NS cannot resume. In particular, following the scheme of

Fig. 2.4, for an initially high mass transfer rate corresponding to  $L_{\max} = 10^{37}$  erg s<sup>-1</sup>, the NS accretes matter and decreases its spin period; the drop in the luminosity to the value of  $L_{\min} = 10^{33}$  erg s<sup>-1</sup>, as in the case of the compact system previously seen, triggers the radio-ejection mechanism. When the luminosity recovers its previous high value, the cyclic behaviour is lost. In fact, for wide systems  $R_{L_1}$  is located beyond  $R_{\text{crit}}$  and  $\mathcal{P}_{\text{DISK}} < \mathcal{P}_{\text{DIP}}$  even for  $L = 10^{37}$  erg s<sup>-1</sup> and accretion cannot resume. The growth of the pressure indicated by track B in Fig. 2.4 is not enough to allow disk formation.

This means that, if the accretion rate fluctuates, there exist a minimum spin period and the NS cannot be spun up at a lower value.

In summary, when a compact system evolves, its spin period decreases until its corresponding critical period become lower than the orbital period. At this point the system assumes the orbital characteristics of a wide system and when radio-ejection phase starts, mass-accretion has to stop definitely, in fact an increase of mass-transfer rate is not able to quench the ejection process.

Once accretion ends, the neutron star is spinning very rapidly and emerges as a millisecond radio pulsar with a very low spin down rate, as its resulting low magnetic field makes dipole radiation very weak.

The aim of this work is to provide observational support to the radio-ejection mechanism by inspecting the orbital and spin parameters of the known population of fully recycled radio pulsars and compare these with the expectation for the occurrence of this mechanism.

### 2.2.1 Luminosity during accretion

In order to understand the behavior of these systems in phase of accretion we have to consider that the AMXPs belong to the class, examined e.g. by Verbunt (1993), of LMXBs evolving via loss of angular momentum, driven by the GR emission process, a very important physical mechanism allowing matter transfer between the two stars at this phase. Without this mechanism mass-transfer would stop, as the binary orbit would tend to widen, thus preventing the contact between the donor star surface and its Roche lobe.

As explained in a more detailed way in Section 1.3.4, during a

conservative mass-transfer driven by GR emission, as the donor mass decreases, the orbital period decreases as well and the mass-transfer rate stabilizes at about the value of  $10^{-10} M_{\odot} \text{ y}^{-1}$ <sup>2</sup>, corresponding to an accretion luminosity  $L_{\text{acc}} = L_{36}$ . In fact, following Di Salvo et al. (2008) and assuming a totally conservative mass transfer, we calculated the accretion luminosity due to GR evolution for typical values of this kind of system with the formula:

$$L_{\text{acc GR}} = 4.77 \times 10^{37} \left[ \frac{1}{n - 1/3 + 2g} \right] m^{8/3} q^2 (1 + q)^{-1/3} P_{2\text{h}}^{-8/3} \text{ erg/s}, \quad (2.6)$$

where  $P_{2\text{h}} = 1$  is the orbital period in units of 2 h,  $g = 1 - q$  with  $q = m_2/m = 0.1$  the mass ratio,  $m = 1.4$ , and  $n = -1/3$  is the index of the mass-radius relation of the secondary  $R_2 \propto M_2^n$ , and obtained  $L_{\text{acc GR}} = 1 \times 10^{36} M_{\odot} \text{ y}^{-1}$ .

### 2.3 Comparisons with observations

In this scenario we can imagine to compare the orbital characteristics of the radio MSPs and the AMXPs with the values of their corresponding critical period placing them in a plot along with the curve identifying the critical period in function of the spin period.

The first case, with the radio MSPs, is shown in Fig. 2.5, where the horizontal axis represents the spin period in milliseconds and in the vertical axis we have:

- the critical orbital period in hours times the magnetic moment,  $\mu_{26}$  (being the magnetic field a parameter independent from the spin period and not constant for the various sources), for three values of the maximum accretion luminosity,  $L_{36} = 1, 10, 100$ . This is represented by the solid lines in the plot and is derived from Eq. 2.5 with parameters:  $\alpha = 1$ ,  $n_{0.615} = 1$ ,  $R_6 = 1$ ,  $m = 1.4$ ,  $\langle m_2 \rangle = 0.2$ , which are typical parameters for the radio MSPs (variations of these parameters will be discussed in Section 2.6);
- the orbital period in hours times the magnetic moment,  $\mu_{26}$ , for the 42

<sup>2</sup>If the mass-transfer is not conservative the effect of the mass loss from the system on the mass-transfer rate is moderate (see Verbunt (1993)).

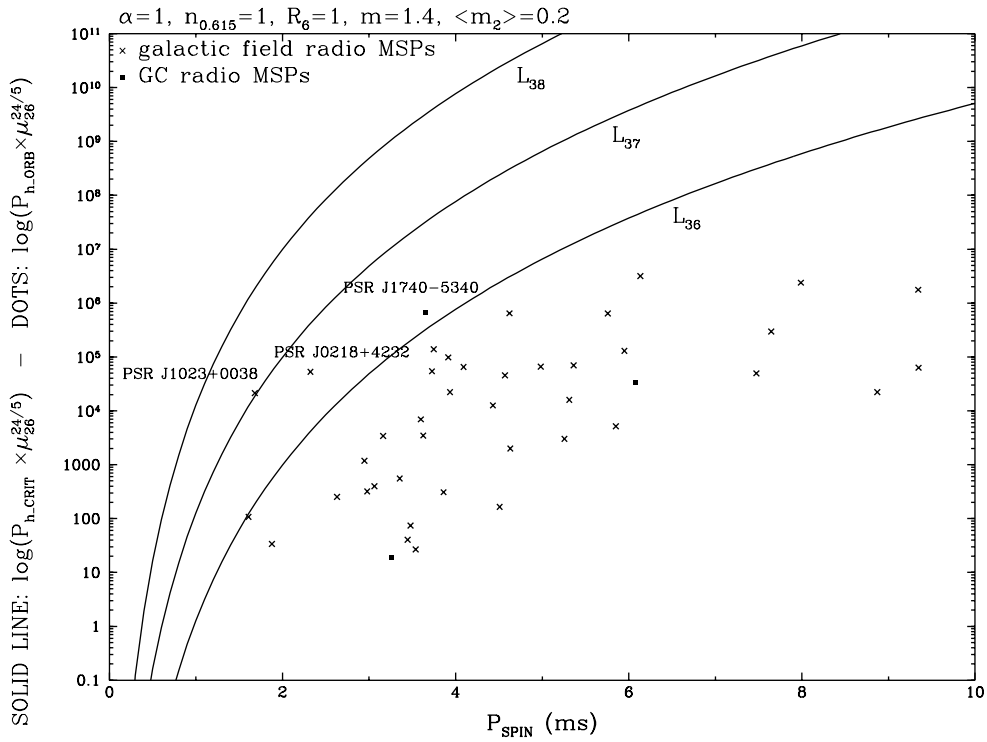


Figure 2.5: Solid lines: critical orbital period in hours times the magnetic moment in  $G \text{ cm}^3$  (logarithmic axis),  $\log[P_{h\_CRIT} \times \mu_{26}^{24/5}]$  (see Equation 2.5), versus spin period in millisecond,  $P_S$ , for three values of the maximum luminosity,  $L_{36} = 1, 10, 100$ . Crosses: orbital period in hours times the magnetic moment versus spin period for MSPs (39 galactic field's and 3 GC's, filled squares). Adopted parameters for Equation 2.5 are indicated on the top of the plot.

radio MSPs listed in Table 2.1<sup>3</sup>, which is represented by crosses for 39 galactic field's and filled squares for 3 of globular clusters (GC).

The choice of the sample of the MSPs has been done considering that evolution of the binary MSPs located in GC should be distinguished from that in the galactic disk because of the potentially very different formation scenarios. In the cores of GCs there is a reasonably high probability of exchange interactions occurring wherein an ordinary star in a close binary

<sup>3</sup>Values derived from ATNF catalogue <http://www.atnf.csiro.au/research/pulsar/psrcat/>; Manchester et al. 2005.

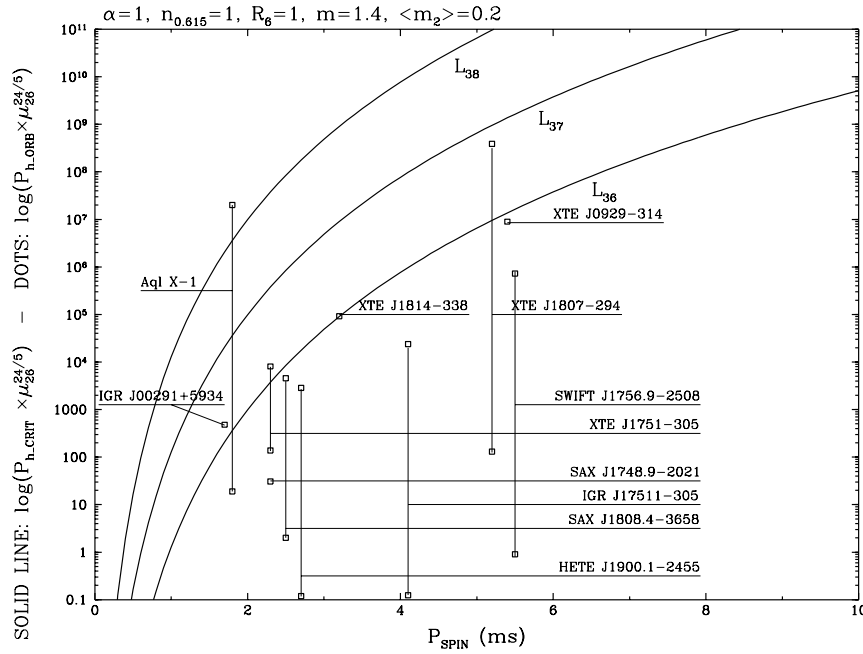


Figure 2.6: Solid lines: critical orbital period in hours times the magnetic moment in  $\text{G cm}^3$  (logarithmic axis),  $\log[P_{h\_CRIT} \times \mu_{26}^{24/5}]$  (see Equation 2.5), versus spin period in millisecond,  $P_S$ , for three values of the maximum luminosity,  $L_{36} = 1, 10, 100$ . Empty squares: orbital period in hours times the magnetic moment versus spin period for eleven of the twelve known AMXPs listed in Table 2.2. Adopted parameters for Equation 2.5 are indicated on the top of the plot.

is exchanged for a NS. Moreover, the presence of an intense gravitational field of the GC core, attracting the sources toward the center of the GC, hampers the precise determination of the spin period derivative and then that of magnetic field of the sources. Then, because dynamics plays such an important role in the evolution of GCs, we will only focus our understanding on the formation and evolution of galactic systems.

Nevertheless we have plotted positions of three of them chosen so that their distance from the GC center is at least ten times the core radius of the GC ( $r_c$ ), PSR J1910-5959A (NGC 6752), PSR J1750-3703B (NGC 6441) and PSR J1740-5340 (NGC 6397), in this way we can consider negligible their interaction with the GC which they belong to.

The second plot, reporting the case of the AMXPs, is shown in Fig. 2.6 in which the solid lines are represented with the same parametrization of the plot of Fig. 2.5, and in which we placed positions of the AMXPs considering the range of values of the magnetic field inferred from literature (see the Table 2.2 for the list of the AMXPs and the corresponding values of magnetic field with their references).

## 2.4 Results

As we can notice, the scenario depicted in Section 2.2 is supported by Fig. 2.5, where all of the MSPs, but three, are below the curve of critical period corresponding to  $L_{36}$ , and most of these are quite far away from it. We can in fact suppose that the MSPs were initially located on one of the critical period lines and since there they are moving to the right in the plot, in complete correspondence with what discussed before.

One exception to this trend is represented by the system PSR J0218+4232, a very luminous binary radio MSP (Navarro et al. 1995), the youngest binary MSP in the galactic field, in which also pulsed X-ray emission (unrelated to an accretion process) has been discovered by Kuiper et al. (1998).

In our graphic we also placed PSR J1023–0038; its position in the plot of Fig. 2.5 results very near, but above, to the critical curve at  $L_{37}$  and is in very good agreement to our model, since it is starting the MSP phase and two things could be happening:

- if its maximum luminosity,  $L_{\max}$ , is  $> L_{37}$ , the system is in the phase in which radio-ejection alternate with accretion, and accretion can shortly resume;
- if  $L_{\max} \lesssim L_{37}$ , likely it has just become part of the class of wide systems and accretion cannot resume.

In any case we expect to find it in the left part of the plot, near to the critic curve at its maximum accretion luminosity. But, as no X-ray burst has been observed so far, we do not have any indications on this last parameter.

Regarding the MSPs belonging to a GC, for PSR J1910–5959A and PSR J1750–3703B, we can observe that their positions are not particularly

different from those of the others sources. However, PSR J1740–5340, on the other hand, indicated in Fig. 2.5, has a peculiar position. This system is in fact believed to be in radio-ejection phase (Burderi et al. 2002) and there is evidence for the fact that the companion is filling its Roche lobe. Its position in the plot is in very good agreement with the proposed scenario, in fact it is located upper the critical curve at  $L_{36}$ , but no so far from it, and its evolutionary stage could be the same of PSR J1023–0038, with the exception that the probable accretion luminosity for PSR J1740–5340 is  $\sim L_{36}$ .

Following what depicted in §2.2, in the AMXPs mass-transfer is occurring to the NS and they are generally found in the spin-up phase. Their spin period is decreasing until they reach the spin period corresponding to their critical orbital period, then we expect that in the plot of Fig. 2.6 they are located near that critical orbital period curve corresponding to their accretion luminosity  $L_{acc}$ , which most likely is equal to  $L_{36}$ , as we derived in §2.2.1.

Positions we got in Fig. 2.6 support very well this evolutionary path, in fact the most part of AMXPs are below the critical curve corresponding to  $L_{36}$ .

## 2.5 New estimates for parameters of MSPs and AMXPs

Results obtained by this work and presented in the previous Section suggest that comparisons with observations totally support the radio-ejection scenario. Therefore we can obtain several information on the evolutionary status of the MSPs and the AMXPs and derive new estimates for some of their several parameters.

### 2.5.1 Age of MSPs

The age of pulsars, assuming that spin-down is only due to magnetic dipole radiation, is calculated with the formula (e.g. Lorimer & Kramer (2004)):

$$\tau = \frac{P_s}{2 \dot{P}_s} \left[ 1 - \left( \frac{P_0}{P_s} \right)^2 \right], \quad (2.7)$$

where  $P_s$  and  $P_0$  are the spin period at present and at birth and  $\dot{P}_s$  is the spin period derivative.

For the ordinary pulsars ( $P_S > 10$  ms) we can assert that  $P_0 \ll P_S$ , and calculate the so-called characteristic age,  $\tau_c = P_S/2 \dot{P}_S$ . But for the MSPs this is not true, in fact, if for ordinary pulsars the spin period at birth is that at the time of the NS formation after the supernova event, for the MSPs it corresponds to that at the end of accretion, which is the spin period corresponding to the critical orbital period, for each MSP.

In this way we can calculate the age of the MSPs deriving  $P_0$  from Eq. 2.5 and using the Eq. 2.7 without approximations.

Results are listed in Table 2.1, and compared to the estimated characteristic ages, which are regarded as an upper limit to the age of the pulsar. It is noticeable that the age arising from this model results shorter, typically of the 30%, than the canonical estimate. Then, thank to this method we can provide a more accurate evaluation of radio MSPs ages, since we can exploit a plausible value for the spin period at the birth of the MSP.

A further evaluation of the age of this kind of systems can be made through the cooling models of the white dwarf (WD) companion, which are based on the value of its mass and temperature, assuming suitable masses of its envelope. Hence, given a cooling model, one can use the measured mass and temperature to determine the “cooling age” of the WD, which provides an indirect estimate of the age of the MSP. The possible use of comparing pulsar and white dwarf ages was realized immediately upon the first detection of optical emission from white dwarf counterparts (Kulkarni 1986) and the first systematic comparison between spin-down and cooling ages was done by Hansen & Phinney (1998a,b).

In Table 2.1 are listed the cooling ages of the detected WD companions in order to compare them with our estimates. In general we can see that measurements of the cooling ages of the white dwarfs provide further evidence that millisecond pulsars have typical ages of a few Gyr which are typically closer to our evaluations than to the characteristic ages.

### 2.5.2 Magnetic field of AMXPs

In the plot of Fig. 2.6 we can think to place the AMXPs on the line corresponding to  $L_{\text{acc}} = L_{36}$ , as resulted in 2.2.1, and derive an estimate of

their surface magnetic field,  $B_s$ , using Eq. 2.5.

Results are reported in Table 2.2, for each source, along with the known estimates corresponding to their position in Fig. 2.6.

For XTE J1751–305 we obtained  $B_s = 6.0 \times 10^8$  G, this value is in good agreement with constraints provided by Wijnands et al. (2005) for a distance of  $\approx 8$  kpc, which is a plausible value according Markwardt et al. (2002). Wijnands et al. (2005) also provided an estimate for the surface magnetic field of XTE J0929–314:  $B_s \approx 3 \times 10^9$  G, for a distance of 10 kpc, slightly lower than our estimate, but the distance toward XTE J0929–314 is not known, only constrained to be  $>5$  kpc (Galloway et al. 2002).

Our estimate of the XTE J1814–338 surface magnetic field is  $B_s = 8.0 \times 10^8$  G, just the same value derived by Papitto et al. (2007) from the spin-down behavior of this source. The same for IGR J00291+5934: Torres et al. (2008) have drawn an upper limit of  $3.0 \times 10^8$  G for its surface magnetic field, which is in very good agreement with our evaluation.

Assuming a constant dipolar magnetic field, Altamirano et al. (2008) estimated the magnetic field to be  $\gtrsim 1.3 \times 10^8$  G for SAX J1748.9–2021, very close to our estimate which is  $B_s = 3.6 \times 10^8$  G.

For the two AMXPs, SAX J1808.4–3658 and Aql. X-1, we have strict constraints on their surface magnetic field, defining ranges that we put in the graphic of Fig. 2.6, using values obtained by Di Salvo & Burderi (2003) and Casella et al. (2008). For SAX J1808.4–3658, Di Salvo & Burderi (2003) obtained  $B_s = (1 - 5) \times 10^8$  G. This estimate places SAX J1808.4–3658 in graphic of Fig. 2.6 very near to the curve corresponding to  $L_{36}$ , then we can strongly argue that, during its evolution, this source is reaching its critical orbital period and its corresponding minimum spin period, accreting matter at a luminosity  $L_{\text{acc}} = L_{36}$ , in very good agreement with the model displayed above.

For the system Aql. X-1, we have to consider a large values range, intercepting three critical curves corresponding to  $L_{36}$ ,  $L_{37}$ ,  $L_{38}$ . This range arises from calculations of the NS surface magnetic field,  $B_s$ . We have, in fact, two values: an upper limit in quiescence,  $B_{s \text{ upper}} \sim 1.8 \times 10^9$  G (see Di Salvo & Burderi (2003)), and a lower limit in outburst,  $B_{s \text{ lower}} \sim 10^8$  G (Casella et al. 2008).

Compared to the other AMXPs, Aql. X-1 can show an higher accretion luminosity since, as secondary is a MS star, magnetic braking (MB) can efficiently act in this system driving its evolution and enhancing the mass-transfer rate compared to the values given by gravitational radiation alone (see e.g. Verbunt 1993). In fact, being Aql. X-1 the AMXP with the longest orbital period (19 hours), it is not part of the aforementioned class undergoing detectable effects of GR emission process.

To check the plausibility of our estimates of magnetic field for the systems XTE J1807–294, HETE J1900.1–2455, SWIFT J1756.9–2508 and the newly discovered IGR J17511–305, for which there are not previous estimates, we compared our results with the magnetic field obtained considering that, in order to have pulsed accretion, the magnetospheric radius (the distance to the NS at which the ram pressure of the infalling matter from the accretion disk balances the pressure of the NS magnetic field) has to lie outside the NS and to be smaller than the corotation radius (at which the disc matter in Keplerian motion rotates with the same angular speed of the NS), i.e.  $R_{\text{NS}} \leq R_{\text{M}} \leq R_{\Omega}$ . Then, considering that  $R_{\text{M}} = \phi R_{\text{A}}$ , where:

$$R_{\text{A}} = 2.23 \times 10^6 R_6^{-2/7} m^{1/7} \mu_{26}^{4/7} \epsilon^{2/7} L_{37}^{-2/7} \text{ cm}, \quad (2.8)$$

with  $\phi \sim 0.2$  and  $\epsilon$  the ratio between the specific luminosity and the specific binding energy ( $L = \epsilon \times GM\dot{M}/R_{\text{NS}}$ ,  $M$  is the NS mass,  $\dot{M}$  is the accretion rate) and using for the distance of IGR J17511–305 the average value of the other AMXPs distances ( $\sim 7$  kpc), we obtained the value range of magnetic field listed in Table 2.2.

For the other newly discovered AMXP in NGC 6440, the mass function has not been estimated yet and we did not insert it in our calculations, but its parameters are anyway shown in Table 2.2.

## 2.6 Effects of the uncertainties on the pulsar parameters and of the equation of state and observational biases

In this Section we will discuss on the possible effects due to the uncertainties on parameters of the radio MSPs that can affect the value of the critical period

(Eq. 2.5) and on the possible alternative explanations that could clarify the lack of detection of the ultra-rapidly spinning radio MSPs.

### 2.6.1 Effects of the parameters uncertainties

In the plots of Figures 2.5 and 2.6 we represented the lines of the critical period with parameters  $\alpha = 1$ ,  $n_{0.615} = 1$ ,  $R_6 = 1$ ,  $m = 1.4$ ,  $m_2 = 0.2$ , also indicated on top of the plot, and here we evaluate the possible changes due to their possible range of variability.

The dependence of the critical period from these parameters results:

$$P_{\text{crit}} \propto (\alpha^{-36} n_{0.615}^{-40} R_6^{34})^{3/50} m^{1/10} \left[ 1 - 0.462 \left( \frac{m_2}{m + m_2} \right)^{1/3} \right]^{-3/2} (m + m_2)^{-1/2}$$

and possible ranges of variation are:  $m \approx 1 \div 2.1 M_{\odot}$  (Lattimer & Prakash 2007) and  $R_6 \approx 0.6 \div 1.5$  (van Paradijs 1982), setting the minimum value for the mass when the maximum value for the radius is settled and vice versa. Their exact values depend on the equation of state (EOS) for the nuclear matter. A suitable range of values for  $\alpha$  is between about 0.1 and 1.0 (see King et al. (2007)), whereas the companion mass spans the interval between few hundredths of solar mass and about 0.9 solar mass (the observed range of mass for the secondary star can be derived inspecting Table 2.1). The variation of  $n_{0.615}$ , is related to the type of star with which we are dealing, the one adopted so far is for stars of population II, but, as for stars of solar type its values is not appreciably different, we estimated that this change does not affect the variation of the critical period and we kept the previous value.

Even a variation in all the parameters (but  $\alpha$ ) at their maximum and minimum values does not affect significantly the critical period. This can be shown in Figure 2.7, where the critical period times the magnetic moment versus the spin period is plotted considering the variations of the aforementioned parameters. The *solid lines* are plotted for the typical parameters at the corresponding luminosity of  $L_{36} = 1, 10$ , while the *dashed* and *dashed and dotted* lines are plotted respect to the luminosity  $L_{36} = 10$ , adopting the values of the parameters at upper and lower limits of their ranges of variation, and keeping equal to 1 the value of  $\alpha$ .

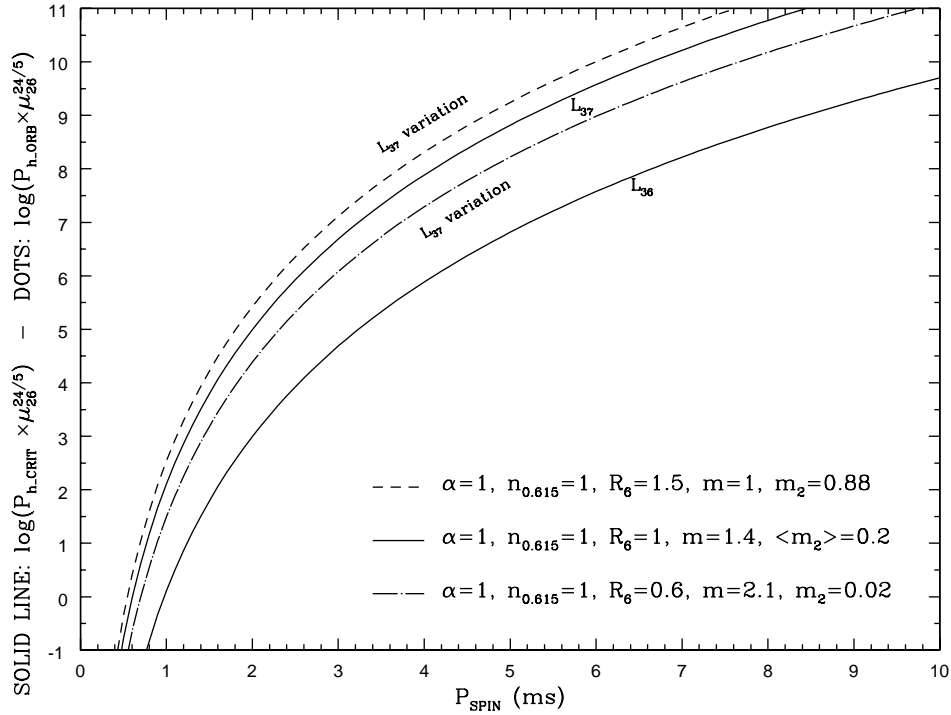


Figure 2.7: Critical period times the magnetic moment versus the spin period plotted adopting typical values (*solid* line) for two values of the accretion luminosity,  $L_{36}$  and  $L_{37}$ , and upper and lower values (*dashed* and *dashed and dotted* lines) of the range of their variation, for  $L_{37}$  and keeping  $\alpha = 1$ . The other values are: for the *dashed* line,  $n_{0.615} = 1$ ,  $R_6 = 1.5$ ,  $m = 1$ ,  $m_2 = 0.88$ , and for the *dashed and dotted* line,  $n_{0.615} = 1$ ,  $R_6 = 0.6$ ,  $m = 2.1$ ,  $m_2 = 0.02$ .

The variation of the curves obtained in this way from those with typical parameters is well within the uncertainty of the maximum accretion luminosity, being this variation of about the 25% of this last uncertainty. However, its value increases significantly adopting the lower limit on  $\alpha$ .

In Figure 2.8 we represented the critical period times the magnetic moment versus the spin period (*dashed* line) respect to the luminosity  $L_{36} = 1$ , for the upper variation of parameters, setting  $\alpha = 0.1$ . This shift is more than one times the uncertainty on the maximum accretion luminosity.

This is not a problem for the theory on radio MSPs, as they still result

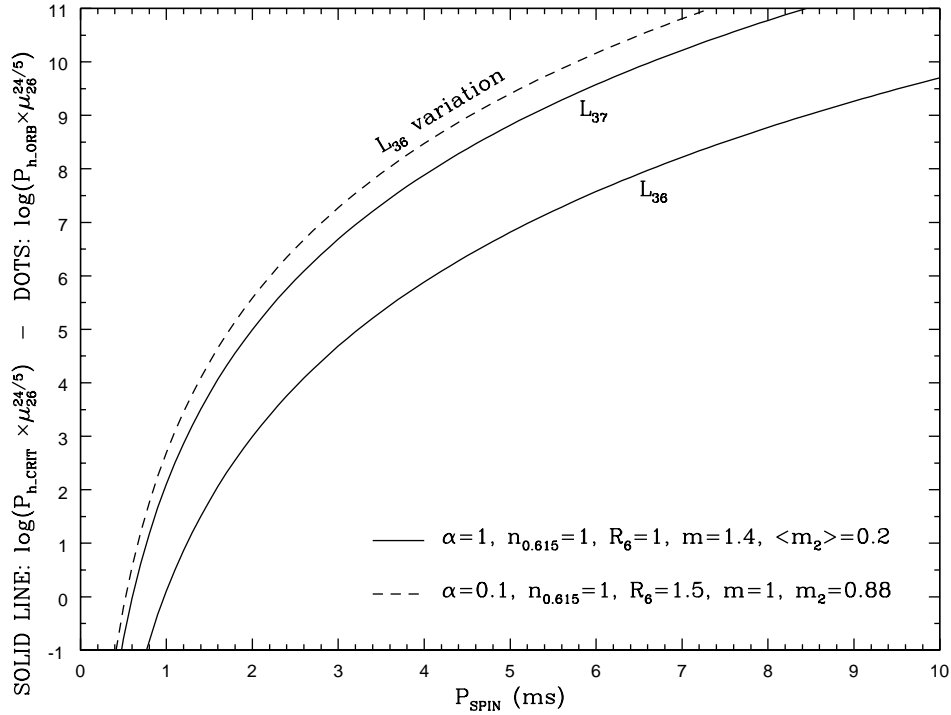


Figure 2.8: Critical period times the magnetic moment versus the spin period plotted adopting typical values (*solid line*) for two values of the accretion luminosity,  $L_{36}$  and  $L_{37}$ , and upper values (*dashed line*) of the range of their variation,  $R_6 = 1.5, m = 1, m_2 = 0.88$ , for  $L_{36}$  and adopting  $\alpha = 0.1$ .

below the line of the critical period corresponding to the lowest value of the luminosity and the age calculated in this way still constitutes a lower limit; but prediction on the magnetic field of AMXPs can result rather different. However it is very difficult to obtain a precise theoretical estimate of parameters of these last systems, in fact even the accretion luminosity is not precisely measured as typically only one burst has been detected and the other bursts could be occurred at different luminosities. For example, in the case of SAX J1808.4–3658, the only AMXPs for which five outburst have been detected, the accretion luminosity variates in a range between  $\sim 0.09 \div \sim 10 \times 10^{36} \text{ erg s}^{-1}$  in the outbursts of 1996, 1998, 2000, 2002 and 2008 (see e.g. Burderi et al. (2009) and Papitto et al. (2005)).

### 2.6.2 The effects of the equation of state and observational biases

So far we have only dealt with the recycling mechanism as a way for explaining the lack of observed MSPs spinning at a period of about or less than 1 ms.

As already briefly mentioned at the end of the Sec. 2.1.1, one can imagine alternative explanations for that observational result. We investigated on some possible mechanisms and observational biases that could prevent the detection of signals accruing from rapidly rotating NSs.

A detailed study of the decreasing of the spin period of a NS experiencing mass accretion (Burderi, Possenti et al. 1999) led to affirm that in a unmagnetized NS the minimum reachable spin period depends on the equation of state (EOS) of the nuclear matter following the behaviour represented in Figure 2.9, where the relation between the spin period and the accreted baryonic mass for three different equations of state is shown.

If the EOS is ultra-stiff, corresponding to a maximum mass of the NS of  $\sim 3 M_{\odot}$ , the minimum achievable spin period (dashed line) is about 1.3 ms and the observed limiting spin period of the known population of MSPs may be well interpreted as a direct consequence of this theoretical prediction.

If the EOS is ultra-soft, corresponding to a maximum mass of the NS of  $\sim 2 M_{\odot}$ , the theoretical minimum achievable spin period (dotted line) is  $\sim 0.6$  ms. In the case of such a soft EOS (as well as for any EOS of intermediate stiffness, like the FPS represented by the solid line in Fig. 2.9), one could expect the existence of some MSP spinning at period larger than  $\sim 0.6$  ms but shorter than the current limit of 1.39 ms. These objects are not observed yet. In principle a possible explanation calls for the effects of the orbital Doppler shift on the signal accruing from a pulsar in binary systems with close orbits, as those generated by the accretion mechanism depicted in Sec. 2.2. That can provide a natural observational bias, disfavoring the discovery of rapidly spinning sources. The bias can be additionally enhanced in the presence of eclipses, also favored in very close binary systems. This effect can be reduced by collecting short data sets, but at the price of a limitation in the reachable minimum observable flux density (e.g. Camilo et al. (2000)) and for this reason systems with periods shorter than  $\sim 90$  min may have been poorly

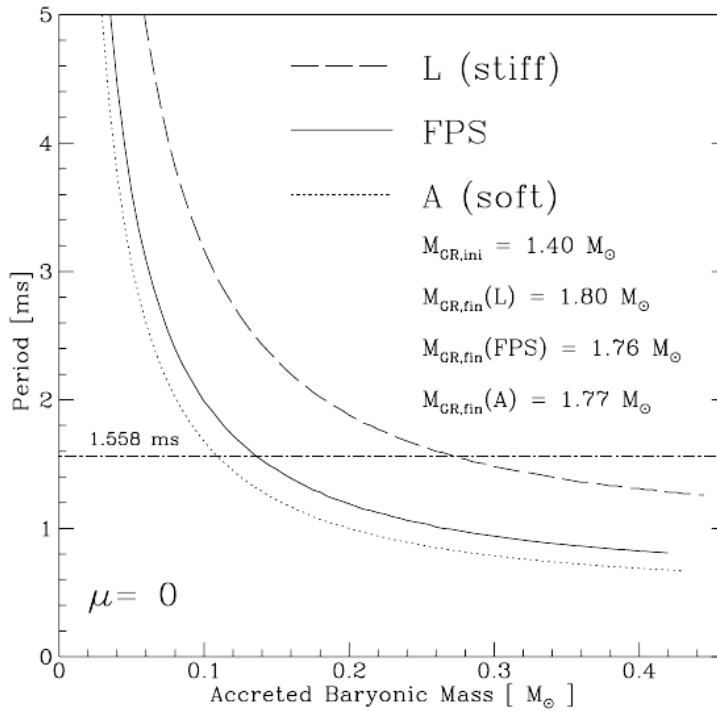


Figure 2.9: Spin period vs accreted baryonic mass relations for the case of an unmagnetized NS considering three selected equations of state: L (stiff: *dashed line*), A (soft: *dotted line*), and FPS (intermediate: *solid line*) (Burderi, Possenti et al. 1999).

searched so far.

## 2.7 Conclusions

The aim of this work was to provide experimental evidences for the so-called radio-ejection mechanism, a mechanism able to overcome the main difficulties found by the recycling model.

The detailed study of orbital and spin characteristics of the current known population of the radio MSPs reveals that this mechanism is totally compatible with the observational data, confirming this scenario.

This result allows us to provide new estimates for the age of the radio MSPs, resulting typically of the 30% shorter than the ordinary estimate, and the magnetic fields of the AMXPs, in line with the previous ones.

## LIST OF RADIO MILLISECOND PULSARS

N.	Name	$P_S$ (ms)	$P_{orb}$ (days)	$B_S$ ( $10^8$ G)	$M_c$ ( $M_\odot$ )	$\tau$ (Gyr)	$\tau_c$ (Gyr)	$\tau_{cooling}$ (Gyr)	Ref. $\tau_{cooling}$
1	PSR J1959+2048	1.607	0.3820	1.67	0.02	0.37	1.51		
2	PSR J1023-0038	1.680	4.5600	3.00	0.13	—	2.22		
3	PSR J0034-0534	1.877	1.5893	0.98	0.14	2.63	6.00	4.4÷14.9	HP98
4	PSR J0218+4232	2.323	2.0288	4.29	0.17	—	0.48	0.7	BV03a
5	PSR J1125-6014	2.630	8.7526	1.04	0.28	5.90	10.4		
6	PSR J1909-3744	2.947	1.5334	2.06	0.20	1.74	3.33		
7	PSR J2229+2643	2.978	93.0159	0.67	0.12	21.0	32.3	$\geq 1$	LC95
8	PSR J0613-0200	3.062	1.1985	1.73	0.13	3.30	5.06		
9	PSR J1640+2224	3.163	175.4607	0.96	0.25	8.55	17.7	3.2÷12.2	HP98
10	PSR J1933-6211	3.354	12.8194	1.13	0.32	9.84	15.2		
11	PSR J2317+1439	3.445	2.4593	0.92	0.17	18.7	22.6		
12	PSR J0751+1807	3.479	0.2631	1.67	0.13	5.72	7.08	$> 0.8$	HP98
13	PSR J1216-6410	3.539	4.0367	0.77	0.16	29.4	34.7		
14	PSR J1600-3053	3.598	14.3485	1.87	0.20	3.22	6.00		
15	PSR J1911-1114	3.626	2.7166	2.29	0.12	2.45	4.06		
16	PSR J2129-5721	3.726	6.6255	3.37	0.13	0.67	1.98		
17	PSR J1741+1351	3.747	16.3353	3.40	0.24	0.40	1.97		
18	PSR J0610-2100	3.861	0.2860	2.21	0.02	3.90	4.95		
19	PSR J1751-2857	3.915	110.7465	2.12	0.19	1.76	5.51		
20	PSR J2019+2425	3.935	76.5116	1.68	0.31	4.50	8.88	3.4÷13.9	HP98
21	PSR J1853+1303	4.092	115.6538	1.93	0.24	3.14	7.33		
22	PSR J1813-2617	4.430	8.1598	2.38	0.19	3.67	5.62		
23	PSR J2051-0827	4.509	0.0991	2.42	0.03	4.87	5.61		
24	PSR J1713+0747	4.570	67.8251	2.00	0.28	4.88	8.49	6.3÷6.8	HP98
25	PSR J1643-1224	4.622	147.0174	2.96	0.12	1.10	3.96		
26	PSR J1709+2313	4.631	22.7119	1.31	0.27	15.9	20.2		
27	PSR J1910+1256	4.984	58.4667	2.23	0.19	4.96	8.08		
28	PSR J1012+5307	5.256	0.6047	3.04	0.11	3.98	4.86	$< 0.4$	HP98
29	PSR J1732-5049	5.313	5.2630	2.74	0.18	4.56	6.10		
30	PSR J1857+0943	5.362	12.3272	3.12	0.24	3.18	4.80	$> 1.4$	HP98
31	PSR J0437-4715	5.757	5.7410	5.81	0.14	0.85	1.59	0.3	HP98
32	PSR J1738+0333	5.850	0.3548	3.80	0.09	3.21	3.85		
33	PSR J2033+17	5.949	56.3080	2.59	0.19	5.90	8.57		
34	PSR J1955+2908	6.133	117.3491	4.32	0.18	1.40	3.27		
35	PSR J1045-4509	7.474	4.0835	3.66	0.16	5.67	6.75	10	SD00
36	PSR J1918-0642	7.646	10.9132	4.33	0.24	3.92	5.05		

## LIST OF RADIO MILLISECOND PULSARS

N.	Name	$P_S$ (ms)	$P_{orb}$ (days)	$B_S$ ( $10^8$ G)	$M_c$ ( $M_\odot$ )	$\tau$ (Gyr)	$\tau_c$ (Gyr)	$\tau_{cooling}$ (Gyr)	Ref. $\tau_{cooling}$
37	PSR J1455–3330	7.987	76.1746	4.46	0.25	3.55	5.21		
38	PSR J1757–5322	8.870	0.4533	4.89	0.56	4.83	5.34		
39	PSR J1804–2717	9.343	11.1287	6.25	0.20	2.83	3.62		
40	PSR J1435–6100	9.348	1.3549	4.84	0.88	5.39	6.05		
1 GC	PSR J1910–5959A (GC)	3.266	0.8371	0.99	0.19	14.7	17.6	< 2	BV03b
2 GC	PSR J1740–5340A (GC)	3.650	1.3541	7.92	0.18	—	0.34		
3 GC	PSR J1750–3703B (GC)	6.075	3.6051	3.45	0.17	3.89	5.02		

HP98 = Hansen & Phinney (1998b), BV03a = Bassa et al. (2003a), LC95 = Lundgren et al. (1995),

SD00 = Schönberner et al. (2000), BV03b = Bassa et al. (2003b)

Table 2.1: Values derived from “The ATNF Pulsar Database”, available at website <http://www.atnf.csiro.au/research/pulsar/psrcat/> (Manchester et al. 2005). GC indicates pulsars belonging to Globular Clusters.

<b>LIST OF THE TWELVE KNOWN AMXPs</b>							
Name	$P_S$ (ms)	$P_{orb}$ (hours)	Companion - Ref.		Ref.	$B_{s\text{ our}}$ (G)	$B_s$ - Ref. ( $10^8$ G)
			Class	$M_c$ ( $M_\odot$ )			
SAX J1808.4–3658	2.5	2.01	BD CM98	0.05	WV98	$5.7 \times 10^8$	$1 \div 5$ D07
XTE J1751–305	2.3	0.71	DD M02	0.015	M02	$6.0 \times 10^8$	$3 \div 7$ W05
XTE J0929–314	5.4	0.73	WD/He DD G02	0.02	G02	$3.3 \times 10^9$	$\lesssim 30$ W05
XTE J1807–294	5.2	0.67	DD F05	0.007	M03	$3.1 \times 10^9$	$3 \div 67$
XTE J1814–338	3.2	4.27	MS K05	0.17	M03b	$8.0 \times 10^8$	8.0 P07
IGR J00291+5934	1.7	2.46	BD T08	0.04	G05	$2.5 \times 10^8$	$\lesssim 3$ T08
HETE J1900.1–2455	2.7	1.39	BD K05b	0.016	K05b	$7.2 \times 10^8$	$0.6 \div 4.9$
SWIFT J1756.9–2508	5.5	0.90	He WD K07	0.007	K07	$3.3 \times 10^9$	$1 \div 17$
Aql. X-1 (4U 1908+005)	1.8	19	MS K-IV S97	$0.45 \div 0.8^a$	C08	$1.8 \times 10^8$	$1 \div 18$ C08
SAX J1748.9–2021	2.3	8.7	MS A08	0.1	A08	$3.6 \times 10^8$	$\lesssim 1.33$ A08
New in NGC 6440	4.9	$0.7 \div 1.17$	–	–	A09	–	–
IGR J17511–305	4.1	3.5	–	0.13	M09	$1.4 \times 10^9$	$0.5 \div 6.3$

<sup>a</sup>Value range derived from spectral classification of K type star (Habets & Heintze 1981).

CM98 = Chakrabarty & Morgan (1998), WV98 = Wijnands & van der Klis (1998), D07 = Di Salvo et al. (2007),

M02 = Markwardt et al. (2002), W05 = Wijnands et al. (2005), G02 = Galloway et al. (2002),

M03 = Markwardt et al. (2003), F05 = Falanga et al. (2005), M03b = Markwardt & Swank (2003),

K05 = Krauss et al. (2005), G05 = Galloway et al. (2005), T08 = Torres et al. (2008), K05b = Kaaret et al. (2006),

K07 = Krimm et al. (2007), C08 = Casella et al. (2008), S97 = Shahbaz et al. (1997), A08 = Altamirano et al. (2008),

A09 = Altamirano et al. (2009), M09 = Markwardt et al. (2009)

Table 2.2: Parameters of AMXPs. The fourth column indicates the star classes which companions, most likely, belong to: DD = Degenerate Dwarf, WD = White Dwarf, BD = Brown Dwarf, MS = Main Sequence star. The fifth column indicates the companion minimum masses, obtained by the mass function for  $\sin i = 1$ , hence for an inclination of  $90^\circ$ . The seventh column indicates the estimates of the surface magnetic field  $B_s$ , derived by Eq. 2.5, for  $L_{36} = 1$ .

## **Chapter 3**

# **Search for radio pulsed emission from four accreting millisecond X-ray pulsars**

In this chapter I present the search for millisecond radio pulsations from four AMXPs, firstly I will briefly introduce in order to understand the main goal of this work, hence I will describe how data analysis has been carried out, I will discuss the results and, finally, I will report on the conclusions.

## 3.1 Introduction

As described in Section 1.3.3, AMXPs are transient binary systems hosting a weakly magnetized ( $B \sim 10^{8-9}$  G) NS, spinning at a period of the order of milliseconds, and accreting matter from its low mass ( $M \leq 1 M_{\odot}$ ) companion.

As we have already seen above, it is commonly believed that AMXPs are the progenitors of the radio MSPs, as argued by the recycling model, which asserts that the NS in these systems is spun-up by the transfer of matter and angular momentum from a companion star via the formation of an accretion disk. When this process ends the NS switches on as a radio MSP.

A strong proof of the recycling model has been obtained by Archibald et al. (2009), who recently detected radio pulsed emission from the binary NS PSR J1023–0038, whose X-ray and optical characteristics are typical of a quiescent AMXP, although X-ray pulsations or outbursts have never been observed.

Despite this last detection, the recycling scenario reveals some issue, as those discussed in Chapter 2, and a ultimate proof would be to observe a system in which X-ray emission alternates with radio emission. The aim of this work is, in fact, to search for radio millisecond pulsations from a sample of AMXPs in their quiescence phase; a positive result would unambiguously establish that AMXPs are the progenitors of at least some of the radio MSPs.

### 3.1.1 Constraints for the switch-on of radio emission

A basic requirement for the switching on of the radio emission is that the light cylinder of the NS has to be free of matter. In other words, the radius of the inner rim of the accretion disk has to be larger than  $R_{lc}$  (Eq 1.35). The radius of the disk inner rim is commonly assumed be equal to the magnetospheric radius,  $R_M$ , which is in turn a fraction  $\phi \leq 1$  of the Alfvén radius at which

the pressure of the NS magnetic field balances the ram pressure of the matter flowing from the accretion disk:

$$R_M = 1 \times 10^6 \phi \mu_{26}^{4/7} \dot{m}_e^{-2/7} m^{-1/7} R_6^{-2/7} \text{ cm}, \quad (3.1)$$

where  $\dot{m}_e$  is the mass accretion rate in Eddington units (for  $R_6 = 1$ ,  $\dot{M}_{\text{Edd}} = 1.5 \times 10^{-8} M_\odot \text{ yr}^{-1}$  and scales with the radius of the compact object) and  $m$  is the NS mass in  $M_\odot$ .

During the quiescence phase of AMXPs, this condition,  $R_M > R_{\text{lc}}$ , can be fulfilled since  $\dot{m}_e \sim 10^{-4}$ . Therefore this phase constitutes the most promising one to investigate for a confirmation of the recycling model. In the last decade, from 1998 April, the date of the discovery of the first AMXP SAX J1808.4–3658 (Wijnands & van der Klis 1998), several attempts were made in order to obtain this confirmation (e.g. Burgay et al. (2003b)), but, despite the fact that eleven additional systems have been discovered since (e.g. Galloway et al. (2002); Casella et al. (2008); Altamirano et al. (2008)), we have not obtained a positive result yet.

### 3.1.2 The effect of the matter enclosing the system

A possible explanation of some of these failures has been given by Burderi et al. (2001), asserting that the detection of radio pulsations from AMXPs could be hampered by matter surrounding the system. In fact, during the so-called *radio-ejection* phase (see Section 2.2), the pressure of the rotating magneto-dipole could prevent the infalling matter from the companion of the NS in the binary system to reach the NS Roche lobe forcing it to leave the system from the Lagrangian point  $L_1$ . Once this happens, such matter, still carrying the angular momentum which it had before leaving the system, will rotate around the two stars embedding the system. Then, if the pulsar radio emission is switched on it could be absorbed by free-free mechanism.

The optical depth for the free-free absorption can be written as (e.g. Burderi et al. (2001)):

$$\tau_{\text{ff}} = 1.6 \times 10^3 \times \frac{\gamma^2 \dot{m}_{-10}^2 (X + 0.5Y)^2 F(m, m_2) Ga}{m^{5/3} T_4^{3/2} P_h^{4/3} \nu_9^2 (1 + m/m_2)^{5/3}}, \quad (3.2)$$

where  $\dot{m}_{-10}$  is the mass transfer rate in outburst in units of  $10^{-10} M_{\odot} \text{ y}^{-1}$ ,  $X$  and  $Y$  are the mass fraction of hydrogen and helium respectively,  $\gamma$  is the fraction of ionized hydrogen,  $T_4$  the temperature of the outflowing matter in units of  $10^4 \text{ K}$ ,  $\nu_9$  the frequency of the radio emission in units of  $10^9 \text{ Hz}$ ,  $P_h$  is the orbital period in hours,  $m$  and  $m_2$  are the masses of the NS and its companion in solar masses,  $F(m, m_2) = 1 - 0.462 m_2 / (m + m_2)$ ,  $Ga = 1.00 + 0.48 (\log T_4 - \log Z) - 0.25 \log \nu_9$  takes into account the dependencies of the Gaunt factor from the temperature, the atomic number  $Z$ , and the frequency. According to this equation, since the optical depth depends on the square inverse of the frequency, signals at higher frequency can avoid complete absorption due to the matter around the system.

With this scenario in mind we have undertaken a campaign of observation at a frequency higher than that typical employed to observe pulsar, 1.4 GHz, on a sample of four AMXPs: XTE J0929–314, XTE J1751–305, XTE J1814–338 and SAX J1808.4–3658.

In fact, applying Eq. 3.2 to these four sources at 1.4, 5,  $\sim 6.5$  and 8.5 GHz we obtained the values listed in Table 3.1, where we used  $m \sim 1.4$ ,  $X = 0.7$ ,  $Y = 0.3$ ,  $\gamma \sim 1$ ,  $T_4 \sim 1$ , and parameters for the single sources indicated in the caption of the Table.

With values of  $\tau_{\text{ff}}$  at 1.4 GHz much higher than unity, the radiation would be totally absorbed, while for frequencies higher than 5 GHz we obtained values less or next to unity for all the sources and, reasonably assuming that the matter enclosing the system is clumpy (i.e. there are favourable directions where the optical depth is lower than the average given by Equation 3.2), we have an higher probability to detect the radio signal.

### 3.2 The sources, the observations and the data analysis

Two series of radio observations were taken on 2003 December 19–23 for XTE J0929–314, XTE J1751–305 and XTE J1814–338, and on 2002 August 5–7 for SAX J1808.4–3658, using the Parkes 64 m radio telescope. Observation parameters are listed in Tables 3.5 and 3.6. The signal was subdivided into several channels to lessen the dispersion effect of the interstellar medium (ISM), then summed in polarization pairs and finally digitized.

Source	$\tau_{\text{ff}}$		
	1.4 GHz	6.5 GHz	8.5 GHz
XTE J0929–314	5	0.2	0.1
XTE J1751–305	27.8	1.1	0.7
XTE J1814–338	2.2	1.2	0.05
	1.4 GHz	5 GHz	6 GHz
SAX J1808.4–3658	9.3	0.7	0.5

Table 3.1: Optical depth at various radio frequencies, for the four analyzed sources. Parameters used are: for XTE J0929–314,  $\dot{m}_{-10} \sim 2.9$ ,  $m_2 \sim 0.02$ ,  $P_h = 0.73$  (Galloway et al. 2002); for XTE J1751–305,  $\dot{m}_{-10} \sim 8.5$ ,  $m_2 \sim 0.015$ ,  $P_h = 0.71$  (Markwardt et al. 2002); for XTE J1814–338,  $\dot{m}_{-10} \sim 1.2$ ,  $m_2 \sim 0.17$ ,  $P_h = 4.27$  (Markwardt & Swank 2003); and for SAX J1808.4–3658,  $\dot{m}_{-10} \sim 3.7$  (which is the average mass transfer rate for the 1998, 2000 and 2002 outbursts, see Papitto et al. (2005)),  $m_2 \sim 0.05$ ,  $P_h = 2.01$ .

The resulting time series were stored on digital linear tapes (DLT) for off-line analysis. The data analysis methodology was chosen on the basis of the precise knowledge of the orbital and spin parameters for the four sources, obtained from the X-ray observation. The original ephemerides were presented by Galloway et al. (2002) for XTE J0929–314, Markwardt et al. (2002) for XTE J1751–305, Markwardt & Swank (2003) for XTE J1814–338 and by Chakrabarty & Morgan (1998) for SAX J1808.4–3658, and subsequently refined by Di Salvo et al. (in prep.; see also Di Salvo et al. 2008b) for XTE J0929–314, Papitto et al. (2008 and 2007) for XTE J1751–305 and XTE J1814–338, and by Hartman et al. (2009) (but also by Burderi et al. (2009), Di Salvo et al. (2008a) and Hartman et al. (2008)) for SAX J1808.4–3658, respectively. Table 3.4 reports the most updated ephemerides used in this work.

For XTE J0929–314, in order to reduce the computational time, we rebinned the data series with  $2^{28}$  samples digitized at one bit every  $100 \mu\text{s}$ , to obtain series with  $2^{27}$  samples and then with a time resolution of  $200 \mu\text{s}$ .

Off-line analysis was made by means of a software suite that, in the first stage, aimed to reduce the dispersion effects on the signal due to the interstellar medium, starting from the DM nominal value obtained by the models of the galactic electron distribution by Taylor & Cordes (1993) and Cordes & Lazio (2001).

We chose to dedisperse the time series with DMs ranging from 1/4 to 4 times the nominal DM value. This range has been chosen accounting the possibility of an increase of the DM value due to the presence of the local matter surrounding the system. The value of the local DM was calculated considering the density of the matter located around the system starting from the area neighbouring the Roche lobe of the NS to a distance from the NS at which this density equates that of the ISM. For SAX J1808.4–3658, we considered the highest mass transfer rate assumed in quiescence,  $\dot{m} \sim 10^{-9} M_{\odot}/\text{y}$ , proposed by Di Salvo et al. (2008a).

The result turns out to be well consistent with our choice of the adopted range for all the three sources which also takes into account the errors in the estimate of the sources distance and of the ISM models. The steps, the ranges of DMs used, and the values of the local DMs for the three sources are indicated in Tables 3.5 and 3.6.

The second part of the data analysis is to correct the effects of the orbital motion of the pulsar in the binary system and the earth in the solar system, deorbiting and barycentring the data series in order to obtain time series as if they were emitted from a source located at the barycentre of its binary systems and collected from a telescope placed at the solar system barycentre.

In doing the deorbiting we have to take into account the propagation of the uncertainties in the original ephemerides over the time range between X-ray and radio observations. This time range corresponds to  $\sim 20000$  orbits for XTE J0929–314 and XTE J1751–305,  $\sim 1000$  orbits for XTE J1814–338. For SAX J1808.4–3658, the adopted X-ray ephemerides are derived from the analysis of the secular evolution reported by Hartman et al. (2009), which refers to the time of  $\sim 100$  orbits after the radio observations.

In order to study the effect of these uncertainties, we simulated four dedispersed time series produced by four pulsars with the same characteristics of the analyzed sources (as refined by Di Salvo et al. (in prep.)),

Papitto et al. (2007 and 2008), and Hartman et al. (2009)). We then deorbited and barycentred these simulated time series using upper and lower limits of the orbital parameters listed in Table 3.4.

For XTE J0929–314, even a variation in all the parameters (but the orbital period, see later) at  $1\sigma$  level does not affect the detectability of the pulsations, since that produced a maximum broadening of the pulse much smaller than 0.1 in pulsar phase. The only exception is for the orbital period:  $1\sigma$  variation in  $P_{\text{orb}}$ , propagated over the  $\sim 20000$  orbits occurred between X-ray and radio observations, produces a broadening of 0.4 in pulsar phase for our observation. Therefore, to obtain a maximum broadening of the pulse of 0.1 in phase, we corrected the time series using 8 trial values of  $P_{\text{orb}}$  (4 above and 4 below the nominal value), covering the  $1\sigma$  uncertainty range.

Also for XTE J1751–305, the uncertainty in all the parameters (except for the orbital period) produced a pulse broadening less than 0.1 in phase, not significantly affecting the detectability of the radio signal. Only the propagation of the orbital period error (90% confidence level) affected the time series losing the possibility of detection of the signal: i.e. producing a broadening of the pulse of 0.9 in pulsar phase. In order to reduce this broadening to at least 0.1 in pulsar phase, one has to search for the signal at 18 trial values of the orbital period, 9 above and 9 below the nominal value, covering the uncertainty range.

For XTE J1814–338 and SAX J1808.4–3658, the uncertainty in all the parameters within the 90% confidence level for XTE J1814–338 and  $1\sigma$  level for SAX J1808.4–3658 does not affect the detectability of the pulsation. We then corrected the data series only using the nominal values of the parameters.

The last step in this search is to fold the time series using the spin parameters reported in Table 3.4. The spin period range explored has to be chosen considering that the nominal value of the spin period at the epoch of the radio observations is:

$$P_{\text{radio}} = P_X \pm \Delta T \dot{P}_X, \quad (3.3)$$

where  $P_X$  is the nominal value of the spin period at the epoch of the X observation,  $\dot{P}_X$  its derivative,  $\Delta T$  the time between the X and radio

observations, and the sign + (−) takes into account the spin-up (spin-down) of the pulsar. Then, maximizing (minimizing) the Equation 3.3 with errors on the measure of  $P_X$  and  $\dot{P}_X$ , the maximum (minimum) value to search for radio signal is  $P_1 = P_X \pm \delta P_X \pm \Delta T(\dot{P}_X + \delta \dot{P}_X)$ , where  $\delta P_X$  and  $\delta \dot{P}_X$  are errors of  $P_X$  and  $\dot{P}_X$ , and the resulting range is  $\Delta P_{\text{tot}} = |P_1 - P_2|$ , where  $P_2 = P_X \mp \delta P_X$ . The values of  $P_X$  and  $\dot{P}_X$  and their errors are reported in Table 3.4.

For SAX J1808.4–3658, which is the only AMXP that showed more than one outburst, we considered the value of  $P_X$  derived by Hartman et al. (2009) and the value of  $\dot{P}_X$  measured during the outburst closest to the radio observations time, reported by Burderi et al. (2006), which results higher than that derived by the analysis of the secular evolution obtained by Hartman et al. (2009) and constitutes an upper limit in the search (see also Sections 3.2.1 and 3.2.2).

The trial values inside  $\Delta P_{\text{tot}}$  have been chosen considering that the pulse broadening for an error equal to the step between two consecutive trial values,  $\delta t$ , has to be less than 0.1 in phase over the whole observation. Then, for XTE J0929–314 we obtained 41 trial values of folding period, for XTE J1751–305 we investigated for 11 trial values of folding period, while for XTE J1814–338 and SAX J1808.4–3658,  $\delta t$  is greater than  $\Delta P_{\text{tot}}$  hence we folded only at the nominal period.

### 3.2.1 Constraints from the surface magnetic field

The spin period derivative, used in the previous section to calculate the possible spin period searching range, is measured during the outburst phase. Once this phase stops, several mechanism could start to drive the changing rate of spin parameters, as magnetic braking or the onset of the propeller phase. Consequently the spin period derivative in quiescence could be different from that in the outburst phase. In order to check whether  $\Delta P_{\text{tot}}$  drawn from the outburst values of  $\dot{P}_X$  is safely large to encompass spin down values observable during quiescence, where  $\dot{P}_S$  is driven only by dipolar emission ( $\dot{P}_{\text{dip}}$ ), we derived the spin period derivative for the four sources from several constraints resulting in the quiescence phase.

For XTE J0929–314, XTE J1814–338 and SAX J1808.4–3658, which are

found to spin-down, we calculated the expected spin period derivative in quiescence considering the magnetic torque acting on the neutron star in this phase.

In the framework of the threaded disk theory applied to MSPs (Rappaport et al. 2004), the torque exerted on the NS by the matter accreting from the disk can be written as:

$$\tau(t) = \dot{M}(t) \sqrt{GMR_{\text{CO}}} - \frac{\mu^2}{9R_{\text{CO}}^3}, \quad (3.4)$$

where  $\dot{M}$  is the mass accretion rate,  $G$  the gravitational constant,  $M$  the NS mass,  $\mu$  the magnetic dipole moment, and  $R_{\Omega}$  the corotation radius (at which the disk matter in Keplerian motion rotates with the same angular speed of the NS), in cgs units. As the source is found to spin down, the first term of Eq. 3.4, the positive contribution to spin up, can be neglected, and the magnetic field results comparing Eq. 3.4 with:

$$\tau(t) = 2\pi I \frac{\dot{P}_S(t)}{P_S^2}, \quad (3.5)$$

where  $I$  (assumed to be  $10^{45}$  g cm<sup>2</sup>) is the NS moment of inertia.

Hence, we obtained an estimate of the dipolar spin down,  $\dot{P}_{\text{dip}}$  through the relation:

$$B_S = 3.2 \times 10^{19} \sqrt{P_S \dot{P}_{\text{dip}}} \text{ G}, \quad (3.6)$$

assumed for spin-down driven by magneto-dipole braking. For XTE J1814–338 the values obtained are  $B_S = 4.3 \times 10^8$  G, consequently, being  $\dot{P}_{\text{dip}} = 6 \times 10^{-20} < \dot{P}_X$ ,  $\dot{P}_{\text{dip}}$  (derived from Equation 3.6) results safely contained in our interval of spin period trial values. For XTE J0929–314 we obtained  $B_S = 6.6 \times 10^8$  G and  $\dot{P}_{\text{dip}} = 7.9 \times 10^{-20}$  and, hence, also in this case, the adopted interval results safely large.

The same conclusions holds for SAX J1808.4–3658, as Burderi et al. (2006) calculated the value of the magnetic field considering that during the last part of the 2002 outburst (the closest to our radio observations), the source has been found to spin-down. They obtained  $B_S \sim (3.5 \pm 0.5) \times 10^8$  G, hence it results that  $\dot{P}_{\text{dip}} = 5.5 \times 10^{-20} < \dot{P}_X$ .

For XTE J1751–305 Wijnands et al. (2005) derived an estimate of the magnetic field during its quiescence phase constrained to be  $< (2.5-6) \times 10^8$  G,

depending on assumed spectral model for the quiescent spectrum and using for the distance the value reported in Table 3.4. The spin period derivative resulted from Eq. 3.6 is, hence,  $< (2.7 - 15) \times 10^{-20}$  which results lower than  $\dot{P}_X$  and, consequently, the adopted  $\Delta P_{\text{tot}}$  is again safely large.

### 3.2.2 Constraints from optical observations

A further check of the validity of the derived  $\dot{P}_S$  (hence of the adopted  $\Delta P_{\text{tot}}$ ), can be obtained from optical observations of the sources in their quiescence phase (except for XTE J1751–305, for which optical observations have never provided any evidence for detection).

In fact, the optical counterparts of the companions of XTE J0929–314, XTE J1814–338 and SAX J1808.4–3658, typically result in a luminosity one order of magnitude higher than expected (Monelli et al. (2005), D’Avanzo et al. (2008), Deloye et al. (2008)). This luminosity excess can be interpreted as the luminosity,  $L_{\text{PSR}}$ , isotropically irradiated by the rotating magneto-dipole, intercepted, and reprocessed by the companion star, as observed e.g. by Burderi et al. (2003) and Campana et al. (2004) for SAX J1808.4–3658, and by D’Avanzo et al. (2007) for IGR J00291+5934.

The excess luminosity can be written as the fraction  $f = f_C + f_D$  of dipolar radiation intercepted by the companion star and the disk (see Burderi et al. 2003):

$$L_{\text{exc}} = f \cdot L_{\text{PSR}} = f \cdot \frac{2\mu^2 \Omega_{\text{NS}}^4}{3c^3} = f \cdot 3.85 \times 10^{35} P_{-3}^{-4} \mu_{26}^2 \text{ erg s}^{-1}, \quad (3.7)$$

where  $\Omega_{\text{NS}}$  is the rotational frequency of the NS and  $f_C$  can be written as  $f_C = 2\pi a^2(1 - \cos \theta)/(4\pi a^2)$ , where  $a$  is the orbital separation and  $\theta$  the angle subtended by the companion star as seen from the central source. If the companion star fills its Roche lobe, this can be written as  $\sin \theta = R_{L_2}/a$ , where  $R_{L_2}$  is the Roche lobe radius of the secondary and  $R_{L_2}/a = 0.49q^{2/3}/[0.6q^{2/3} + \ln(1 + q^{1/3})]$  (Eggleton 1983).

$f_D$  is evaluated adopting a standard Shakura-Sunyaev disk model (Shakura & Sunyaev 1973) and is given by the projected area of the disk as seen by the central source,  $2\pi R \times 2H(R)$  (where  $R$  is the disk outer radius and  $H(R)$  the disk semi-thickness at  $R$ ), divided by the total area,  $4\pi R^2$ .

Source	$f$	$L_{\text{exc}}$ (erg s $^{-1}$ )	$\dot{P}_S$ (s s $^{-1}$ )
XTE J0929–314	$1.5 \times 10^{-2}$	$\sim 3 \times 10^{32}$	$8.9 \times 10^{-20}$
XTE J1814–338	$3 \times 10^{-2}$	$\sim 1 \times 10^{34}$	$2.7 \times 10^{-19}$
SAX J1808.4–3658	$2 \times 10^{-2}$	$\sim 1 \times 10^{34}$	$1.3 \times 10^{-19}$

Table 3.2: Spin period derivative (fourth column) obtained for XTE J0929–314, XTE J1814–338 and SAX J1808.4–3658, considering the excess of optical luminosity,  $L_{\text{exc}}$  (third column). The second column indicates the fraction  $f$  of dipolar radiation intercepted by the companion star and the disk (Burderi et al. 2003), calculated with parameters indicated in Table 3.4 and adopting: for XTE J0929–314,  $\dot{m}_{-10} \sim 2.9$ ,  $m_2 \sim 0.02$ ; for XTE J1814–338,  $\dot{m}_{-10} \sim 1.2$ ,  $m_2 \sim 0.17$ ; and for SAX J1808.4–3658,  $\dot{m}_{-10} \sim 3.7$ ,  $m_2 \sim 0.05$ .

In Table 3.2 the spin period derivatives, obtained combining Equations 3.7 and 1.33, are indicated, considering the values of the optical luminosities reported by Monelli et al. (2005) (see also D’Avanzo et al. (2008)) for XTE J0929–314, D’Avanzo et al. (2008) for XTE J1814–338 and by Deloye et al. (2008) for SAX J1808.4–3658.

The values obtained are in all the three cases lower than the observed ones, preserving our safely large choice of the folding period interval.

### 3.3 Results

At the end of the three step analysis we produced  $\sim 51000$  folded profiles for XTE J0929–314, whose results have been published by Iacolina et al. (2009),  $\sim 67000$  for XTE J1751–305,  $\sim 330$  for XTE J1814–338, and  $\sim 200$  for SAX J1808.4–3658, reporting the results from the folding of the dedispersed, deorbited and barycentred time series.

The best ones have been displayed for visual inspection searching for possible pulsar suspects.

An example of these plots is shown in Figures 3.1 and 3.2, left panel (for XTE J0929–314 and XTE J1751–305, see below). The bottom diagram

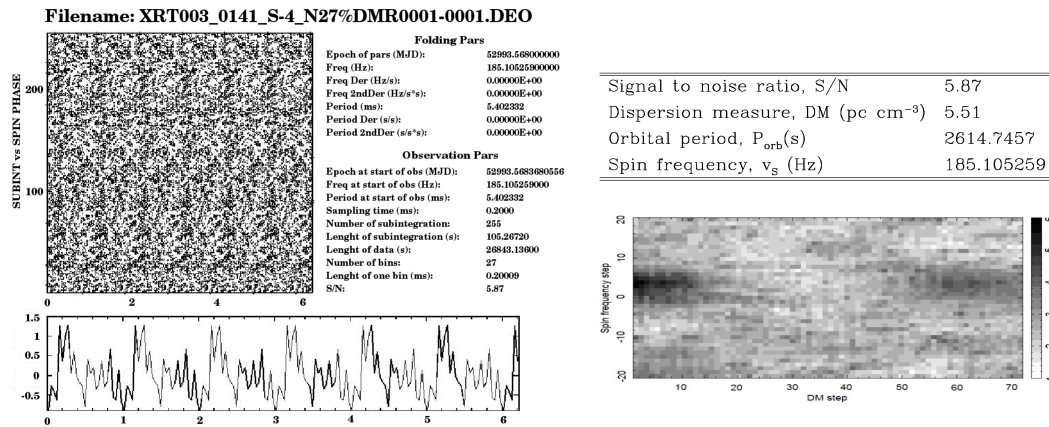


Figure 3.1: Left panel: plot with the highest  $S/N$  for XTE J0929–314. The grayscale *on the left* shows the signal in the 255 subintegrations of the whole observation vs the spin phase. *On the right* are indicated the parameters used for the folding. The diagram *on bottom* displays about 6 phases of the integrated pulse profile. Top right panel: parameters for the candidate with the highest  $S/N$ . Bottom right panel:  $S/N$  in function of the spin frequency (20 step above and 20 below the nominal value, corresponding to 0) and the dispersion measure (72 steps corresponding to values interval from 5.51 to 396.74 cm<sup>-3</sup>· pc) at  $P_{\text{orb}} = 2614.74575$  s (Iacolina et al. 2009).

shows the integrated pulse profile, while the grayscale on the left represents the signal in the 255 subintegrations in which the observation has been subdivided. A good candidate should display a roughly linear trend in the grayscale and a high signal-to-noise ratio pulse profile. On the right, the parameters used for the folding of this candidate are shown, along with the parameters of the observation.

A useful diagnostic tool that can be adopted to further evaluate the plausibility of a suspect is shown in Fig. 3.1 and 3.2, bottom right panel, where a grayscale of the strength of the signal (with darker points at higher  $S/N$ ), plotted as a function of dispersion measure DM and spin frequency  $\nu_s$ , should define a clear peak around the correct parameters of the putative pulsar. The same kind of plot can be created at a constant DM with  $\nu_s$  and  $P_{\text{orb}}$  on the axes or at a constant  $\nu_s$ , tracing the  $S/N$  trend at varying DMs and

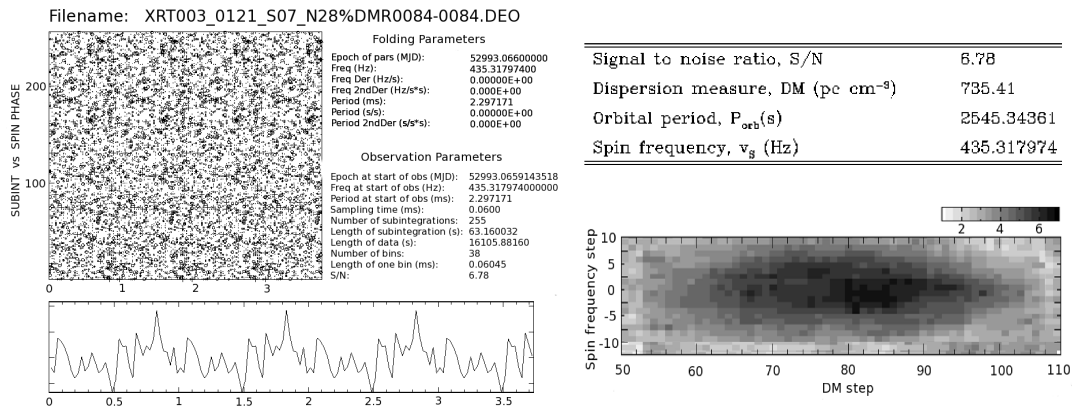


Figure 3.2: Left panel: plot with the highest  $S/N$  for XTE J1751–305. The grayscale *on the left* shows the signal in the 255 subintegrations of the whole observation vs the spin phase. *On the right* are indicated the parameters used for the folding. The diagram *on bottom* displays about 4 phases of the integrated pulse profile. Top right panel: parameters for the candidate with the highest  $S/N$ . Bottom right panel:  $S/N$  in function of spin frequency (10 step above and 11 below the nominal value, corresponding to 0) and DM (60 steps corresponding to the interval between 485.22 and 932.54  $\text{pc cm}^{-3}$ ) at  $P_{\text{orb}} = 2545.34361$  s (Iacolina et al., submitted).

$P_{\text{orb}}S$ .

For XTE J0929–314, the highest  $S/N$  obtained in this search is 5.87 corresponding to a peak at  $3.4\sigma$  significance, that, over the 26568 trial foldings performed on the 6.5 GHz dataset ( $72 \text{ DMs} \times 9 P_{\text{orb}}S \times 41 P_sS$ ), has a probability of not being randomly generated by noise of  $\sim 10^{-6}$ .

In the grayscale of Fig. 3.1 (bottom right panel) we note that the decreasing  $S/N$  trend is not particularly defined, although a maximum is present. Also, the effect that the DM that maximises the  $S/N$  is close to zero (w.r.t an expected value of  $\gtrsim 100 \text{ pc/cm}^3$ ) weakens the credibility of the signal. Finally, this signal suspect is not confirmed in the observations at higher frequency (8.5 GHz), elaborated with the same parameters. From the above considerations we can conclude that no radio pulsation with the expected periodicity has been found in the source XTE J0929–314 during its quiescent phase.

For XTE J1751–305, the highest  $S/N$  obtained was 6.78 corresponding to a peak at  $4\sigma$  significance, the corresponding plot is shown in Fig. 3.2 with its parameters. This peak has a probability of 40% of not being randomly generated over the 40755 trial foldings of its dataset. Analysing the behaviour of the  $S/N$  in function of the spin frequency and DM trial values, a decreasing trend from a peak at  $S/N = 6.78$  is found. Since this peak was at the limit of our search interval in spin frequency, we considered it appropriate to investigate for further 11 steps in the spin frequency, discovering, in this way, the whole trend. In this way the maximum, which is resulted to correspond to the same  $S/N$ , is defined in all the directions. The result is displayed in Fig. 3.2 (bottom right panel), where a clear maximum is well defined supporting the plausibility of the suspect.

This result is not confirmed in the other observation (at the same frequency) elaborated with the same parameters, but this could be due to the clumpiness of the matter around the system. Then, this suspect may deserve additional investigation in the future.

The highest  $S/N$ s reached for XTE J1814–338 and for SAX J1808.4–3658 were 4.67 and 4.41, corresponding to a peak at  $2.6\sigma$  and  $2.2\sigma$  significance respectively, with a probability of being real radio signals and not produced by noise of 18% and 20% over the 186 and 57 trial foldings of their single dataset, respectively. Unfortunately visual inspection of these two results and others at lower  $S/N$ s did not provide any evidence for the pulsed signal, and, moreover, further investigations have not even shown the positive signs on the trend of the  $S/N$  obtained for XTE J0929–314 and XTE J1751–305. Finally, the observations at the other frequency, folded with the same parameters, did not displayed any suitable shape of the signal, hence, for these two sources, we can conclude that no pulsed radio signal at their spin period has been detected in our observations.

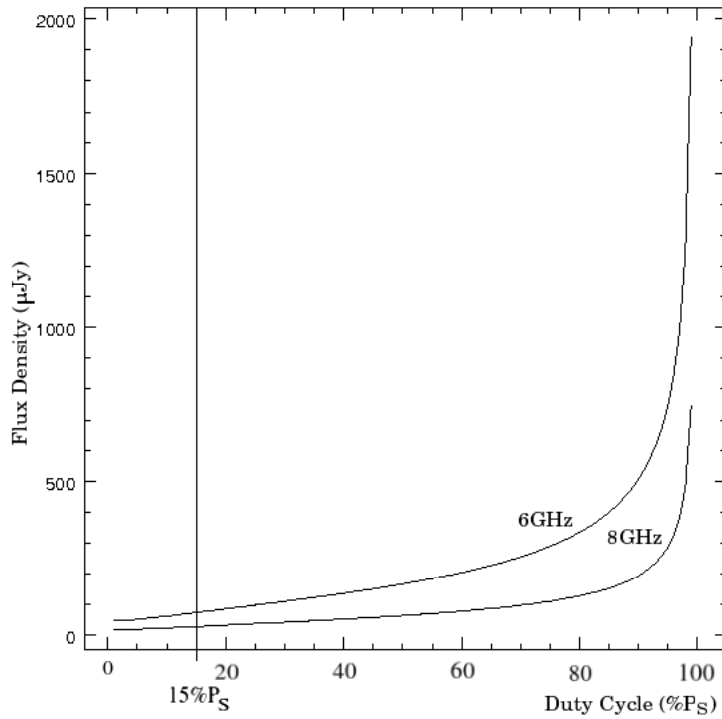


Figure 3.3: Flux density upper limits in  $\mu\text{Jy}$  for XTE J0929–314 obtained with Eq. 3.8 for increasing values of the duty cycle (Iacolina et al. 2009).

### 3.3.1 Upper limit on the flux density

The upper limit on the flux density for the four observed sources can be estimated through the relation (Manchester et al. 1996):

$$S = \frac{\epsilon n_\sigma (T_{\text{sys}} + T_{\text{sky}})}{G (N_p \Delta t \Delta \nu_{\text{MHz}})^{1/2}} \left( \frac{W_e}{P_S - W_e} \right)^{1/2} \text{ mJy}, \quad (3.8)$$

where  $n_\sigma$  is the threshold  $S/N$  considered in the search,  $T_{\text{sys}}$  is the system noise temperature,  $T_{\text{sky}}$  is the temperature of the sky in Kelvin at the frequencies of the observations obtained from that at a frequency of 408 MHz and scaled as  $\nu^{-2.7}$ ;  $G$  is the gain of the radio telescope,  $\Delta t$  is integration time,  $N_p$  the number of polarizations (here 2),  $\Delta \nu_{\text{MHz}} = 576 \text{ MHz}$  is the bandwidth in MHz, and finally  $\epsilon \sim 1.4$  is a factor representing digitization and other processing losses. The term  $W_e$  is the effective pulse width and is given by:

$$W_e = \left( W^2 + (\beta \delta t_{\text{sam}})^2 + \delta t_{\text{DM}}^2 + \delta t_{\text{scatt}}^2 \right)^{1/2}, \quad (3.9)$$

where  $W$  is the intrinsic pulse width,  $\delta t_{\text{sam}}$  the sampling time,  $\beta$  a factor depending on the technical characteristics of the receiver, and  $\delta t_{\text{DM}}$  and  $\delta t_{\text{scatt}}$  are the pulse broadening due to the dispersion of the signal in each channel and the scattering induced by inhomogeneities of the ISM respectively. All of these parameters and their units are listed in Tables 3.5 and 3.6 for the four sources.

Assuming a duty cycle,  $W/P_s$ , of 15% for all the four sources, we obtained the flux density upper limits, calculated at the nominal DM and indicated in Table 3.3, while the dependence of the minimum flux density achievable from the duty cycle is shown in Fig.3.3, as an example, for XTE J0929–314.

Source	$S_{\text{max}} (\mu\text{Jy})$	
	6.5 GHz	8.5 GHz
XTE J1814–338	52	25
XTE J1751–305	–	31 - 30
XTE J0929–314	68	26
	5 GHz	6 GHz
SAX J1808.4–3658	59	59

Table 3.3: Flux density upper limits for the four sources at the analyzed frequencies, calculated at the nominal values of DM.

### 3.4 Discussion

We have analyzed eight data series containing the radio observations of XTE J0929–314, XTE J1751–305, XTE J1814–338, and SAX J1808.4–3658 at high frequency. In this Section we will discuss our results about our findings.

A part for the result obtained for the 8.5 GHz observation of XTE J1751–305, deserving additional investigation, no radio pulsed emission has been found in the data analyzed. Assuming that the radio emission was switched on during the observations of the four sources, we investigated on the possible reasons that prevented the detection of the radio signals.

### 3.4.1 The geometric factor

The radio emission of a pulsar is strongly anisotropic, in fact the pulses are formed by a beam of emission which sweeps across a narrow portion of the sky. The lack of the detection of radio signals from our sources, then, could be due to the possibility that the pulsar beam does not intersect our line of sight.

Emmering & Chevalier (1989) calculated the average value of the fraction of the solid angle swept from two conal radio beams as a function of their half width  $\beta$ :

$$f(\beta) = \int_0^{\pi/2} f(\beta, \eta) \sin \eta \, d\eta = (1 - \cos \beta) + \left(\frac{\pi}{2} - \beta\right) \sin \beta, \quad (3.10)$$

where  $\eta$  is the angle between the rotational axis and the magnetic axis (aligned with the radio beams), and  $f(\beta, \eta) = \cos[\max(0, \eta - \beta)] - \cos[\min(0, \eta + \beta)]$ .

Considering a range of pulse width of 10% ÷ 30% of  $P_s$ , which means to have  $9^\circ \leq \beta \leq 27^\circ$ , we obtain  $0.05 \leq f(\beta) \leq 0.37$ . Assuming a typical duty cycle of 15% for each source,  $f(\beta) \approx 0.34$  and the probability that the beams of all the four sources are missing our line of sight is  $\sim 19\%$ .

In order to exclude this geometric bias we have to perform the analysis of the whole known sample of twelve AMXPs, since, for a duty cycle of 15% for each source, the probability to miss all the beam of the whole sample is about 0.1%.

### 3.4.2 The luminosity upper limits

As the true luminosity of pulsars cannot be measured because of the unknown beaming fraction, a 'pseudo luminosity',  $L$ , is defined as the observed flux density,  $S$ , multiplied by the square of the pulsar distance,  $d$  (Taylor & Manchester 1977):  $L = S \times d^2$ .

In Fig. 3.4 the logarithmic distribution of the pseudoluminosity at 1.4 GHz of the sample of 46 known galactic field MSPs is shown<sup>1</sup>. The vertical

<sup>1</sup>Data taken from the ATNF pulsar catalogue – <http://www.atnf.csiro.au/research/pulsar/psrcat/>; Manchester et al. (2005).

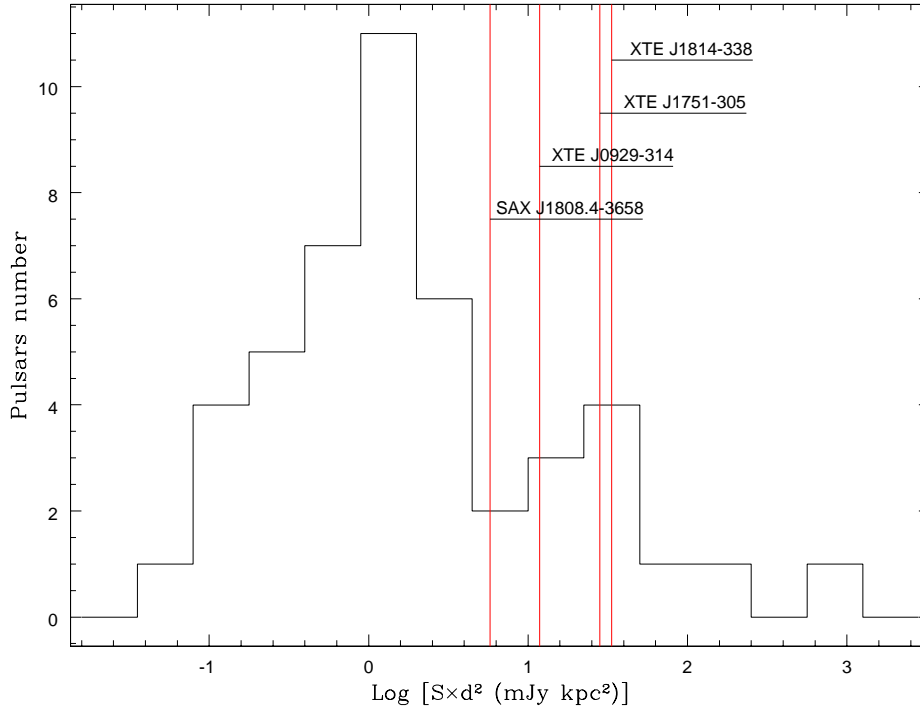


Figure 3.4: Pseudoluminosity distribution of a sample of 46 MSPs of galactic field. The red lines indicate the upper limits related to the four sources analyzed in this work.

red lines indicate the lower values of the upper limits on  $L$  of XTE J0929–314, XTE J1751–305, XTE J1814–338 and SAX J1808.4–3658 (for the observations at 8.5 GHz and 5 GHz), scaled at 1.4 GHz, considering a dependence on the frequency  $S(\nu) \propto \nu^{-\alpha}$ , with an index  $\alpha = 1.7$ , and for the distances indicated in Table 3.4.

These limits determine the probability that the true pseudo luminosity of each source is too faint for detection in our search. We calculated that this probability is about 90% for XTE J1814–338 and XTE J1751–305 and  $\sim 80\%$  for SAX J1808.4–3658 and for XTE J0929–314. The combined probability of the non detection due to the luminosity threshold of our survey is  $\sim 50\%$ . This percentage is not negligible and can be reduced by a deeper search and/or by a larger sample.

Expanding the sample to all the twelve known AMXPs, with a

probability equal to about 80% for each one, the combined probability would result of  $\sim 10\%$ , not enough for a safe detection. In order to have a combined probability less than  $\sim 0.1\%$ , we have to also perform a deeper search. The upper limit in pseudo-luminosity for each source for having such a probability is  $L \approx 2$  mJy kpc<sup>2</sup>, and, for an average distance of 7 kpc,  $S \approx 0.04$  mJy at 1.4 GHz which, scaled at 4.7 GHz (as, for example, for the observation of SAX J1808.4–3658) becomes  $S \approx 0.003$  mJy. Such a limit can be reached performing observations using telescopes with a larger bandwidth and a larger instantaneous sensitivity. In fact the 4.7 GHz observation of SAX J1808.4–3658, performed using a 2 GHz bandwidth and 2.01 K Jy<sup>-1</sup> gain at the Green Bank radio telescope (GBT) (at the  $S/N$  threshold), would have reached a flux density limit of  $\approx 0.003$  mJy.

### 3.5 Conclusions

We have performed a search for radio millisecond pulsations in four accreting millisecond X-ray pulsars, XTE J0929–314, XTE J1751–305, XTE J1814–338 and SAX J1808.4–3658, in their quiescence phase at high frequencies, overcoming in this way the problem of the free-free absorption.

As previously reported, despite for XTE J1751–305 for which further investigations are needed, no pulsations with the expected periodicity have been detected in the analyzed data. The flux density upper limits determined by our search are:

- for XTE J0929–314: 68  $\mu$ Jy at 6.5 GHz and 26  $\mu$ Jy at 8.5 GHz;
- for XTE J1751–305: 30  $\mu$ Jy at 8.5 GHz;
- for XTE J1814–338: 52  $\mu$ Jy at 6.5 GHz and 25  $\mu$ Jy at 8.5 GHz;
- for SAX J1808.4–3658: 59  $\mu$ Jy at 5 – 6 GHz.

Presuming that the radio emission from the pulsar was on during our observations, we investigated on some possible mechanisms that might have hampered the observation of the pulsed signal, concluding that the low luminosity of the four analyzed sources is the determinant factor, being

~50% the combined probability of the non detection due to the luminosity threshold of our survey. The anisotropic nature of the pulsar emission also implies a probability of ~19% that the beam of all the four sources does not intersect our line of sight.

In order to overcome these two observational biases we have to perform observations of the whole known sample of AMXPs, using a telescope with larger bandwidth and instantaneous sensitivity, as, for example, the GBT.

Source parameters	XTE J1814–338	XTE J1751–305
Right ascension (J2000.0)	18 <sup>h</sup> 13 <sup>m</sup> 39 <sup>s</sup> .04	17 <sup>h</sup> 51 <sup>m</sup> 13 <sup>s</sup> .49
Declination (J2000.0)	−33°46′22″.3	−30°37′23″.4
Orbital period, $P_{\text{orb}}$ (s)	15388.7229(2)	2545.342(2)
Projected semi-major axis, $a \sin i$ (lt-ms)	390.633(9)	10.125(5)
Eccentricity, $e$	$< 2.4 \times 10^{-5}$ <sup>a</sup>	$< 1.3 \times 10^{-3}$
Spin period <sup>b</sup> , $P_S$ (s)	0.0031811056698(1)	0.002297172972(2)
Mean spin period derivative, $\dot{P}_S$ (s s <sup>−1</sup> )	$6.7(7) \times 10^{-19}$	$-1.95(10) \times 10^{-18}$
Ascending node passage, $T_0$ (MJD)	52797.8101689(9)	52368.0129023(4)
Distance, $d$ (kpc)	8	6.7
Nominal DM (pc cm <sup>3</sup> )	~200	~400

Source parameters	XTE J0929–314	SAX J1808.4–3658
Right ascension (J2000.0)	09 <sup>h</sup> 29 <sup>m</sup> 20 <sup>s</sup> .19	18 <sup>h</sup> 08 <sup>m</sup> 27 <sup>s</sup> .54
Declination (J2000.0)	−31°23′3″.2	−36°58′44″.3
Orbital period, $P_{\text{orb}}$ (s)	2614.748(3)	7249.156980(4)
Projected semi-major axis, $a \sin i$ (lt-ms)	5.988(10)	62.812(2)
Eccentricity, $e$	$< 0.007$	$< 1.2 \times 10^{-4}$ <sup>c</sup>
Spin period <sup>b</sup> , $P_S$ (s)	0.0054023317856(4)	0.00249391975978(6)
Mean spin period derivative, $\dot{P}_S$ (s s <sup>−1</sup> )	$1.63(12) \times 10^{-18}$	$4.7(9) \times 10^{-19}$
Ascending node passage, $T_0$ (MJD)	52405.48676(1)	52499.9602472(9)
Distance, $d$ (kpc)	6	3.5
Nominal DM (pc cm <sup>3</sup> )	~100	~100

<sup>a</sup>  $3\sigma$  upper limit

<sup>b</sup> The reported values are referred at epoch MJD for XTE J0929–314, at  $T_0$  for SAX J1808.4–3658, at 52797.27387859868 MJD for XTE J1814–338 and at 52368.653 MJD for XTE J1751–305.

<sup>c</sup> 95% confidence upper limit

Table 3.4: Orbital and spin parameters for XTE J0929–314 (Di Salvo et al. in prep.), XTE J1751–305 (Papitto et al. 2008), XTE J1814–338 (Papitto et al. 2007) and SAX J1808.4–3658 (Hartman et al. 2009). For XTE J0929–314, the errors on the last quoted digit(s), reported in parentheses, are intended to be at  $1\sigma$ . For XTE J1751–305 and XTE J1814–338, the errors are at the 90 per cent confidence level and are reported in parentheses, except where explicitly indicated. For SAX J1808.4–3658 the spin period derivative is referred to the outburst closest to our radio observations (Burderi et al. (2006), with error at the 90% confidence level; see the text for further explanations), while the other parameters are referred to the timing after the 2008 outburst (Hartman et al. (2009), with errors at  $1\sigma$  level.

Table 3.5: Parameters for the observations and data analyses for XTE J1814–338 and XTE J1751–305, taken with Parkes radio telescope.

<b>Pulsar names</b>	<b>XTE J1814–338</b>		<b>XTE J1751–305</b>	
<b>Observation parameters</b>			<b>1<sup>st</sup></b>	<b>2<sup>nd</sup></b>
Central radio frequency, $\nu_{\text{obs}}$ (GHz)	6.4105	8.4535	8.4535	8.4535
Data series time, $\Delta t$ (s)	25053	10669	17145	22864
Sampling time, $\delta t_{\text{sam}}$ ( $\mu\text{s}$ )	92	50	60	100
Samples number, $N_s$	$2^{28}$	$2^{27}$	$2^{28}$	$2^{27}$
Nominal gain <sup>a</sup> , $G$ ( $\text{K Jy}^{-1}$ )	0.46	0.59	0.59	
System temperature <sup>a</sup> , $T_{\text{sys}}$ (K)	50	25	25	
Number of 3 MHz channels, $N_c$	192		192	
<b>Data analysis parameters</b>				
Number of DMs	186	151	195	127
DM range ( $\text{pc cm}^3$ )	$\sim 50 \div 1000$		$\sim 100 \div 1700$	
Local DM ( $\text{pc cm}^3$ )	$\sim 20$		$\sim 260$	
Number of $P_{\text{orb}}$ steps	1		19	
Number of folding steps	1		11	
<b>Other parameters</b>				
Sky temperature, $T_{\text{sky}}$ (K)	0.06	0.03	0.09	
Dispersion broadening, $\delta t_{\text{DM}}$ ( $10^{-8}\text{s}$ )	$9.5 \times \text{DM}$	$4.2 \times \text{DM}$	$4.2 \times \text{DM}$	
Scattering broadening, $\delta t_{\text{scatt}}$ (s)	$9.3 \times 10^{-9}$	$3.2 \times 10^{-9}$	$4.4 \times 10^{-7}$	

<sup>a</sup>Values derived from the Parkes website:

<http://www.parkes.atnf.csiro.au/observing/documentation/>.

Table 3.6: Parameters for the observations and data analyses for XTE J0929–314 and SAX J1808.4–3658, taken with Parkes radio telescope.

Pulsar names	XTE J0929–314		SAX J1808.4–3658	
<b>Observation parameters</b>				
Central radio frequency, $\nu_{\text{obs}}$ (GHz)	6.4105	8.4535	4.7495	6.3515
Data series time, $\Delta t$ (s)	27001	27224	35685	35051
Sampling time, $\delta t_{\text{sam}}$ ( $\mu\text{s}$ )	100	100	125	125
Samples number, $N_s$	$2^{28}$	$2^{28}$	$2^{28}$	$2^{28}$
Nominal gain <sup>a</sup> , $G$ (K Jy <sup>-1</sup> )	0.46	0.59		0.46
System temperature <sup>a</sup> , $T_{\text{sys}}$ (K)	50	25		50
Number of 3 MHz channels, $N_c$		192		192
<b>Data analysis parameters</b>				
Number of DMs	72	33	135	57
DM range (pc cm <sup>3</sup> )	~ 10÷400		~ 20÷400	
Local DM (pc cm <sup>3</sup> )	~100		~230	
Number of $P_{\text{orb}}$ steps	9		1	
Number of folding steps	19		1	
<b>Other parameters</b>				
Sky temperature, $T_{\text{sky}}$ (K)	0.02	0.01	0.13	0.06
Dispersion broadening, $\delta t_{\text{DM}}$ (10 <sup>-8</sup> s)	$9 \times \text{DM}$	$4 \times \text{DM}$	$23 \times \text{DM}$	$9.7 \times \text{DM}$
Scattering broadening, $\delta t_{\text{scatt}}$ (s)	~ $1 \times 10^{-9}$		$9.6 \times 10^{-9}$	$3 \times 10^{-9}$

<sup>a</sup>Values derived from the Parkes website:

<http://www.parkes.atnf.csiro.au/observing/documentation/>.

# Conclusions

This PhD thesis work has been developed in the framework of the studies focused on the recycling model, a scenario primarily elaborated in the early 80s by Ali Alpar and collaborators (Alpar et al. 1982).

The main subject of this scenario is the evolution of the radio millisecond pulsars (MSPs), and the evolutionary link between them and the low mass X-ray binaries (LMXBs): the recycling model asserts that LMXBs are the progenitors of radio MSPs.

In particular my work has been subdivided in two main parts.

- **Evolution in recycling scenario**

The first part of my work refers to the main difficulties which the original version of the recycling model finds in predict the parameters of the fully recycled MSPs, as mass and spin period. In fact,

- there exist a gap of permitted spin periods, as the minimum observed spin periods are longer than the critical limit for mass-shedding of the neutron star at its equator for most equation of state of the nuclear matter;
- the mass accreted onto the neutron star during the low-mass X-ray binary phase is large enough to overcome the maximum mass allowed for a neutron star, implying a collapse into a black hole, for most equation of state of nuclear matter.

Various possibilities have been proposed in literature for solving these issues. Here I explored the so-called radio-ejection mechanism, which naturally overcomes these problems. In fact, during the accretion phase, the balance between the pressure of the accreting matter and the radiation pressure of the rotating magneto-dipole determines a critical orbital period above which the accretion of matter is inhibited by the pulsar radiation pressure, determining in this way a limit on the accreted mass onto the neutron star and hence on its spin-up.

During this work I inspected the orbital and spin parameters of the known population of fully recycled radio pulsars and compared these with the expectation for the occurrence of the radio-ejection mechanism.

Results of this search totally support the possibility that this mechanism can occur in this kind of systems, allowing to derive new estimates for several parameters as the age of the radio MSPs (which resulted typically of the 30% shorter than the canonical estimate) and the magnetic field for the accreting millisecond X-ray pulsars (AMXPs), in line with the previous estimates.

- **Search for radio millisecond pulsations in four accreting millisecond X-ray pulsars**

The second part of the work concerned the search for radio millisecond pulsations in a sample of four AMXPs (XTE J0929–314, XTE J1751–305, XTE J1814–338 and SAX J1808.4–3658) in their quiescence phase at high frequencies; this in order to minimize the problem of the free-free absorption.

The search has been carried out on the basis of the precise knowledge of the orbital and spin ephemerides, refined with a timing technique which allows to perform an accurate determination of these parameters from X-ray data.

I analyzed data contained in eight time series, taken at Parkes radio-telescope in Australia, two for each source, subdividing the search in three steps. The first step has been to correct the time series for the dispersion effects on the signal due to the interstellar medium. The second was to deorbit and barycentre the time series to eliminate the effects of the orbital motion of the neutron star in the binary system and the earth in the solar system. The last step was to fold the (already deorbited and barycentred) time series according to the spin parameters.

Results of this search has been that, except the case of XTE J1751–305 for which further investigations are needed, no pulsations with the expected periodicity have been detected in the analyzed data. The flux density upper limits determined in this search are the best even determined for these sources:

- for XTE J0929–314:  $68 \mu\text{Jy}$  at 6.5 GHz and  $26 \mu\text{Jy}$  at 8.5 GHz;
- for XTE J1751–305:  $30 \mu\text{Jy}$  at 8.5 GHz;
- for XTE J1814–338:  $52 \mu\text{Jy}$  at 6.5 GHz and  $25 \mu\text{Jy}$  at 8.5 GHz;

- for SAX J1808.4–3658:  $59 \mu\text{Jy}$  at 5–6 GHz.

Presuming that the radio emission from the pulsar was on during our observations, I investigated on some possible mechanisms that might have hampered the observation of the pulsed signal. I concluded that the luminosity of the four analyzed sources is the determinant factor, being  $\sim 50\%$  the combined probability of the non detection due to a luminosity of the sources not being large enough for reaching (at their distance) the flux density threshold of the survey. The anisotropic nature of the pulsar emission also implies a probability of  $\sim 19\%$  that the radio beam of all the four sources does not intersect our line of sight.

In order to overcome these two observational biases it is necessary to perform observations of the whole known sample of AMXPs, using a telescope with larger bandwidth and instantaneous sensitivity, as, for example, the Green Bank radio telescope.

## **Appendix A**

# **Physical and astronomical constants and units**

<b>Physical and astronomical constants</b>		
Gravitational constant	$G$	$= 6.67259 \times 10^{-8} \text{ dyne cm}^2 \text{ g}^{-2}$
Boltzmann's constant	$k$	$= 1.38 \times 10^{-16} \text{ erg K}^{-1}$
Plank constant	$h$	$= 6.63 \times 10^{-27} \text{ erg s}$
Stefan-Boltzmann constant	$\sigma$	$= 5.67 \times 10^{-5} \text{ erg cm}^{-2} \text{ s}^{-1} \text{ K}^{-4}$
Speed of light in vacuum	$c$	$= 2.99792 \times 10^{10} \text{ cm s}^{-1}$
Radiation constant	$a$	$= 4\sigma/c = 7.565767 \times 10^{-15} \text{ erg cm}^{-3} \text{ K}^{-4}$
Neutron mass	$m_n$	$= 1.6749 \times 10^{-24} \text{ g}$
Proton mass	$m_p$	$= 1.6726 \times 10^{-24} \text{ g}$
Hydrogen mass	$m_H$	$= 1.6735 \times 10^{-24} \text{ g}$
Electron mass	$m_e$	$= 9.1093 \times 10^{-28} \text{ g}$
Solar luminosity	$L_\odot$	$= 3.826 \times 10^{33} \text{ erg s}^{-1}$
Solar radius	$R_\odot$	$= 6.9599 \times 10^{10} \text{ cm}$
Solar mass	$M_\odot$	$= 1.989 \times 10^{33} \text{ g}$
Solar effective temperature	$T_\odot$	$= 5770 \text{ K}$
<b>Astronomical units</b>		
Astronomical unit	AU	$= 1.496 \times 10^{13} \text{ cm}$
Light year	ly	$= 9.4605 \times 10^{17} \text{ cm}$
Parsec	pc	$= 3.0857 \times 10^{18} \text{ cm}$ $= 3.2616 \text{ ly}$

## **Appendix B**

# **The Parkes radiotelescope**



Figure B.1: The Parkes radiotelescope (New South Wales, Australia). - <http://www.parkes.atnf.csiro.au/>

The Parkes Observatory, is a 64 metre telescope used for radio astronomy. It is located about 20 kilometres north of Parkes, in the New South Wales (Australia) and is part of The Australia Telescope National Facility (ATNF) a division of the Commonwealth Scientific and Industrial Research Organisation (CSIRO).

It was one of several radio antennas used to receive images of the Apollo 11 moon landing in July 1969.

The telescope has an altazimuth mount. It is guided by a small mock-telescope placed within the structure at the same rotational axes as the dish, but with an equatorial mount. The two are dynamically locked when tracking an astronomical object by a laser guiding system.

The collecting area of the telescope is a 64 m diameter paraboloid (the dish). The surface is high precision aluminium millimetre wavepanels to a diameter of 17 m (for operation to 43 GHz), then perforated aluminium plate out to 45 m, and rectangular galvanised steel 5/16 inch mesh for the remainder of the surface. The focal ratio is 0.41 for the full 64 m surface, the focus being located 26 m above the centre. The aerial cabin, which houses feeds and receiver equipment, is supported by a tripod. Access to the aerial cabin is either by the lift on one of the tripod legs (the "lift leg") or by a ladder on one of the other legs. The feed platform translator, which holds up to four

receivers, at the base of the aerial cabin has both up/down (focus), lateral and rotational movement. Further properties of the radio telescope and the list of receiver used for the observation of the four sources analyzed in this work are shown below.

Table B.1: Properties of the Parkes radio telescope.

Diameter of dish	64 m
Weight of dish	300 tons
Weight of counterweights	475 tons
Total weight of the dish	1000 tons
Surface area of reflecting mesh	0.004 km <sup>2</sup>
Height of concrete tower	10.7 m
Height to centre of dish	27.4 m
Height to top of aerial cabin	58.6 m
Power of Azimuth/Zenith drives	11 kW
Pointing accuracy	better than 20 arcsec
Coverage	Az 0 – 360°, El 30.5 – 88.5°

Table B.2: Receivers used for the observations of the four AMXPs analyzed in this work at Parkes 64–meters radiotelescope.

Receiver	Band (cm)	Range (GHz)	FWHP (')	T <sub>sys</sub> (K)	Sen [a] (Jy/K)	Pols [b]	Bandw (MHz)
Multiband [c]	6	4.5 – 5.1	4.2	50	2.2	C	500
Methanol	5	5.9 – 6.3	3.3	50	2.2	2xC	300
Methanol	5	6.4 – 6.8	3.3	50	2.2	2xC	300
Mars [d]	3	8.0 – 8.9	2.45	25	1.7	2xC	500

# List of Figures

1.1	Galactic distribution of the known population of radio pulsars. - <a href="http://www.astro.wisc.edu/goat/article/7/">http://www.astro.wisc.edu/goat/article/7/</a> . . . . .	5
1.2	A three-dimensional representation of the Roche potential in a binary star. The droplet-shaped figures in the equipotential plot at the bottom of the figure are called the Roche lobes of each star. $L_1$ , $L_2$ and $L_3$ are the Lagrangian points where forces cancel out. Mass can flow through the saddle point $L_1$ from one star to its companion, if the latter fills its Roche lobe. - <a href="http://hemel.waarnemen.com/Informatie/Sterren/hoofdstuk6.html\#mtr">http://hemel.waarnemen.com/Informatie/Sterren/hoofdstuk6.html\#mtr</a> . . . . .	6
1.3	Graphic illustration of an X-ray binary system. - <a href="http://www.redorb">http://www.redorb</a> . . . . .	7
1.4	Orbital period (left) and mass-transfer rate (right) as a function of the donor mass, $M_2$ , for binary evolution driven by angular momentum losses due to emission of gravitational radiation. For MS donors (solid and dashed lines for stars on on the hydrogen and helium MS respectively), the orbital period decreases and the mass-transfer rate is roughly constant, as the donor mass decreases. The dash-dotted line indicates systems in which a half of matter lost by the donor star leaves the system, $\beta = 0.5$ , with the specific angular momentum of the MS donor, $\alpha = 1$ . Then, non-conservative mass transfer has roughly the same effect of the conservative one (Verbunt 1993).	18

1.5	Disc accretion disrupted by the magnetic field of a neutron star. - <a href="http://lheawww.gsfc.nasa.gov/users/audley/diss/node23.html">http://lheawww.gsfc.nasa.gov/users/audley/diss/node23.html</a> . . . . .	20
1.6	Artistic impression of accretion mechanism from a disc to the polar caps of a magnetized neutron star. - <a href="http://www.astro.umd.edu/~miller/Gallery/compact/">http://www.astro.umd.edu/~miller/Gallery/compact/</a> . . . . .	22
1.7	Artistic impression of the radio pulsar geometry. - <a href="http://www.iasf-milano.inaf.it/Divulgazione/divulgazione/doc/pulsazioni_del_cielo_02.pdf">http://www.iasf-milano.inaf.it/Divulgazione/divulgazione/doc/pulsazioni_del_cielo_02.pdf</a> . . . . .	23
1.8	Diagram of spin period derivative versus spin period for the about 1800 pulsars discovered so far, as from the pulsar catalogue at <a href="http://www.atnf.csiro.au/research/pulsar/psrcat/">http://www.atnf.csiro.au/research/pulsar/psrcat/</a> . Red asterisks are the magnetic-powered pulsars (AXP and SGR), blue points are isolated rotation-powered pulsars and magenta circles refer to rotation-powered pulsars belonging to binary systems. The green and red solid lines represent the so-called <i>spin-up</i> and <i>death</i> lines (see Sec. 1.5). Isochrone (spin down age, see Sec. 1.4.1) and constant magnetic field lines are also plotted as dotted and dashed lines respectively. . . . .	25
1.9	Examples of integrated pulse profiles for different pulsars, freely available from the online database: <a href="http://www.jb.man.ac.uk/research/pulsar/Resources/epn/browser.html">http://www.jb.man.ac.uk/research/pulsar/Resources/epn/browser.html</a> . . . . .	28
1.10	The typical pulse drift of a radio signal crossing the ISM. - <a href="http://relativity.livingreviews.org/Articles/lrr-2008-8/fig_6.html">http://relativity.livingreviews.org/Articles/lrr-2008-8/fig_6.html</a> . . . . .	30
1.11	Schematic representation of the effect of the interstellar scattering on the photons emitted by a source. . . . .	31
1.12	$P_S - \dot{P}_S$ diagram. The evolution of an isolated pulsar follows the cyan arrow. Its spin period increases until it crosses the death line. Spin up line is drawn for Eddington rate mass transfer and for standard values of all the parameters. . . . .	32

1.13	Normalized distribution of the magnetic field strengths of isolated radio pulsar (black line) and those in binary system (gray line). The peak of the field distribution of pulsars in binaries lies at $\sim 10^8$ G, about four orders of magnitudes below that of isolated pulsars. . . . .	35
2.1	Radial dependence of the pressures relevant for the evolution of accreting and recycled NSs. The parameters adopted are: $\mu_{26} = 5, P_{-3} = 1.5, \alpha = 1, n_{0.615} = 1, R_6 = 1, m = 1.4, f = 1$ . . . . .	42
2.2	Left: case of a compact system, $R_{\text{crit}}$ lies outside the Roche lobe of the NS, then the disk pressure, $\mathcal{P}_{\text{DISK}}$ , in $R_{L_1}$ can overcome the radiation pressure of the radio pulsar, $\mathcal{P}_{\text{DIP}}$ , starting the accretion phase. Right: case of a wide system, the critical radius, $R_{\text{crit}}$ , lies inside the Roche lobe of the NS; when the luminosity attains its maximum value, $L_{\text{max}}$ , in $R_{L_1}$ the disk pressure cannot overcome the radio pulsar radiation pressure, for any value of the luminosity less than approximately $L_{\text{max}}$ , then the matter will be ejected from the system. . . . .	44
2.3	Radial dependence of the pressures relevant for the evolution of accreting and recycled NSs. Case of a compact system. The parameters adopted are: $\mu_{26} = 5, P_{-3} = 1.5, \alpha = 1, n_{0.615} = 1, R_6 = 1, m = 1.4, f = 1$ . . . . .	45
2.4	Radial dependence of the pressures relevant for the evolution of accreting and recycled NSs. Case of a wide system. The parameters adopted are: $\mu_{26} = 5, P_{-3} = 1.5, \alpha = 1, n_{0.615} = 1, R_6 = 1, m = 1.4, f = 1$ . . . . .	46
2.5	Solid lines: critical orbital period in hours times the magnetic moment in $\text{G cm}^3$ (logarithmic axis), $\log[P_{h\_CRIT} \times \mu_{26}^{24/5}]$ (see Equation 2.5), versus spin period in millisecond, $P_S$ , for three values of the maximum luminosity, $L_{36} = 1, 10, 100$ . Crosses: orbital period in hours times the magnetic moment versus spin period for MSPs (39 galactic field's and 3 GC's, filled squares). Adopted parameters for Equation 2.5 are indicated on the top of the plot. . . . .	49

- 2.6 Solid lines: critical orbital period in hours times the magnetic moment in  $\text{G cm}^3$  (logarithmic axis),  $\log[P_{h\_CRIT} \times \mu_{26}^{24/5}]$  (see Equation 2.5), versus spin period in millisecond,  $P_S$ , for three values of the maximum luminosity,  $L_{36} = 1, 10, 100$ . Empty squares: orbital period in hours times the magnetic moment versus spin period for eleven of the twelve known AMXPs listed in Table 2.2. Adopted parameters for Equation 2.5 are indicated on the top of the plot. . . . . 50
- 2.7 Critical period times the magnetic moment versus the spin period plotted adopting typical values (*solid* line) for two values of the accretion luminosity,  $L_{36}$  and  $L_{37}$ , and upper and lower values (*dashed* and *dashed and dotted* lines) of the range of their variation, for  $L_{37}$  and keeping  $\alpha = 1$ . The other values are: for the *dashed* line,  $n_{0.615} = 1, R_6 = 1.5, m = 1, m_2 = 0.88$ , and for the *dashed and dotted* line,  $n_{0.615} = 1, R_6 = 0.6, m = 2.1, m_2 = 0.02$ . . . . . 57
- 2.8 Critical period times the magnetic moment versus the spin period plotted adopting typical values (*solid* line) for two values of the accretion luminosity,  $L_{36}$  and  $L_{37}$ , and upper values (*dashed* line) of the range of their variation,  $R_6 = 1.5, m = 1, m_2 = 0.88$ , for  $L_{36}$  and adopting  $\alpha = 0.1$ . . . . . 58
- 2.9 Spin period vs accreted baryonic mass relations for the case of a unmagnetized NS considering three selected equations of state: L (stiff: *dashed* line), A (soft: *dotted* line), and FPS (intermediate: *solid* line) (Burderi, Possenti et al. 1999). . . . . 60

3.1	Left panel: plot with the highest $S/N$ for XTE J0929–314. The grayscale <i>on the left</i> shows the signal in the 255 subintegrations of the whole observation vs the spin phase. <i>On the right</i> are indicated the parameters used for the folding. The diagram <i>on bottom</i> displays about 6 phases of the integrated pulse profile. Top right panel: parameters for the candidate with the highest $S/N$ . Bottom right panel: $S/N$ in function of the spin frequency (20 step above and 20 below the nominal value, corresponding to 0) and the dispersion measure (72 steps corresponding to values interval from 5.51 to 396.74 $\text{cm}^{-3} \cdot \text{pc}$ ) at $P_{\text{orb}} = 2614.74575$ s (Iacolina et al. 2009). . . . .	75
3.2	Left panel: plot with the highest $S/N$ for XTE J1751–305. The grayscale <i>on the left</i> shows the signal in the 255 subintegrations of the whole observation vs the spin phase. <i>On the right</i> are indicated the parameters used for the folding. The diagram <i>on bottom</i> displays about 4 phases of the integrated pulse profile. Top right panel: parameters for the candidate with the highest $S/N$ . Bottom right panel: $S/N$ in function of spin frequency (10 step above and 11 below the nominal value, corresponding to 0) and DM (60 steps corresponding to the interval between 485.22 and 932.54 $\text{pc cm}^{-3}$ ) at $P_{\text{orb}} = 2545.34361$ s (Iacolina et al., submitted). . . . .	76
3.3	Flux density upper limits in $\mu\text{Jy}$ for XTE J0929–314 obtained with Eq. 3.8 for increasing values of the duty cycle (Iacolina et al. 2009). . . . .	78
3.4	Pseudoluminosity distribution of a sample of 46 MSPs of galactic field. The red lines indicate the upper limits related to the four sources analyzed in this work. . . . .	81
B.1	The Parkes radiotelescope (New South Wales, Australia). - <a href="http://www.parkes.atnf.csiro.au/">http://www.parkes.atnf.csiro.au/</a> . . . . .	94

# List of Tables

1.1	Parameters of AMXPs. The fourth column indicates the star classes which companions, most likely, belong to: DD = Degenerate Dwarf, WD = White Dwarf, BD = Brown Dwarf, MS = Main Sequence star. The fifth column indicates the companion minimum masses, obtained by the mass function for $\sin i = 1$ , hence for an inclination of $90^\circ$ . . . . .	14
2.1	Values derived from “The ATNF Pulsar Database”, available at website <a href="http://www.atnf.csiro.au/research/pulsar/psrcat/">http://www.atnf.csiro.au/research/pulsar/psrcat/</a> (Manchester et al. 2005). GC indicates pulsars belonging to Globular Clusters. . . . .	62
2.2	Parameters of AMXPs. The fourth column indicates the star classes which companions, most likely, belong to: DD = Degenerate Dwarf, WD = White Dwarf, BD = Brown Dwarf, MS = Main Sequence star. The fifth column indicates the companion minimum masses, obtained by the mass function for $\sin i = 1$ , hence for an inclination of $90^\circ$ . The seventh column indicates the estimates of the surface magnetic field $B_s$ , derived by Eq. 2.5, for $L_{36} = 1$ . . . . .	63

- 3.1 Optical depth at various radio frequencies, for the four analyzed sources. Parameters used are: for XTE J0929–314,  $\dot{m}_{-10} \sim 2.9$ ,  $m_2 \sim 0.02$ ,  $P_h = 0.73$  (Galloway et al. 2002); for XTE J1751–305,  $\dot{m}_{-10} \sim 8.5$ ,  $m_2 \sim 0.015$ ,  $P_h = 0.71$  (Markwardt et al. 2002); for XTE J1814–338,  $\dot{m}_{-10} \sim 1.2$ ,  $m_2 \sim 0.17$ ,  $P_h = 4.27$  (Markwardt & Swank 2003); and for SAX J1808.4–3658,  $\dot{m}_{-10} \sim 3.7$  (which is the average mass transfer rate for the 1998, 2000 and 2002 outbursts, see Papitto et al. (2005)),  $m_2 \sim 0.05$ ,  $P_h = 2.01$ . 68
- 3.2 Spin period derivative (fourth column) obtained for XTE J0929–314, XTE J1814–338 and SAX J1808.4–3658, considering the excess of optical luminosity,  $L_{\text{exc}}$  (third column). The second column indicates the fraction  $f$  of dipolar radiation intercepted by the companion star and the disk (Burderi et al. 2003), calculated with parameters indicated in Table 3.4 and adopting: for XTE J0929–314,  $\dot{m}_{-10} \sim 2.9$ ,  $m_2 \sim 0.02$ ; for XTE J1814–338,  $\dot{m}_{-10} \sim 1.2$ ,  $m_2 \sim 0.17$ ; and for SAX J1808.4–3658,  $\dot{m}_{-10} \sim 3.7$ ,  $m_2 \sim 0.05$ . . . . . 74
- 3.3 Flux density upper limits for the four sources at the analyzed frequencies, calculated at the nominal values of DM. . . . . 79
- 3.4 Orbital and spin parameters for XTE J0929–314 (Di Salvo et al. in prep.), XTE J1751–305 (Papitto et al. 2008), XTE J1814–338 (Papitto et al. 2007) and SAX J1808.4–3658 (Hartman et al. 2009). For XTE J0929–314, the errors on the last quoted digit(s), reported in parentheses, are intended to be at  $1\sigma$ . For XTE J1751–305 and XTE J1814–338, the errors are at the 90 per cent confidence level and are reported in parentheses, except where explicitly indicated. For SAX J1808.4–3658 the spin period derivative is referred to the outburst closest to our radio observations (Burderi et al. (2006), with error at the 90% confidence level; see the text for further explanations), while the other parameters are referred to the timing after the 2008 outburst (Hartman et al. (2009), with errors at  $1\sigma$  level. . . . . 84

---

3.5	Parameters for the observations and data analyses for XTE J1814–338 and XTE J1751–305, taken with Parkes radio telescope. . . . .	85
3.6	Parameters for the observations and data analyses for XTE J0929–314 and SAX J1808.4–3658, taken with Parkes radio telescope. . . . .	86
B.1	Properties of the Parkes radio telescope. . . . .	95
B.2	Receivers used for the observations of the four AMXPs analyzed in this work at Parkes 64–meters radiotelescope. . . .	95

# Bibliography

- Alpar, M. A., Cheng, A. F., Ruderman, M. A., & Shaham, J. 1982, *Nature*, 300, 728
- Altamirano, D., Casella, P., Patruno, A., Wijnands, R., & van der Klis, M. 2008, *ApJ*, 674, L45
- Altamirano, D., Strohmayer, T. E., Heinke, C. O., et al. 2009, *The Astronomer's Telegram*, 2182, 1
- Archibald, A. M., Stairs, I. H., Ransom, S. M., et al. 2009, *Science*, 324, 1411
- Baade, W. & Zwicky, F. 1934, *Physical Review*, 46, 76
- Bassa, C. G., van Kerkwijk, M. H., & Kulkarni, S. R. 2003a, *A&A*, 403, 1067
- Bassa, C. G., Verbunt, F., van Kerkwijk, M. H., & Homer, L. 2003b, *A&A*, 409, L31
- Bildsten, L. 1998, *ApJ*, 501, L89+
- Bisnovatyi-Kogan, G. S. & Komberg, B. V. 1974, *Sov. Astron.*, 18, 217
- Bradt, H. V. D. & McClintock, J. E. 1983, *Ann. Rev. Astr. Ap.*, 21, 13
- Burderi, L., D'Antona, F., & Burgay, M. 2002, *ApJ*, 574, 325
- Burderi, L., D'Antona, F., Menna, M. T., & Stella, L. 2001, in *Astronomical Society of the Pacific Conference Series*, Vol. 229, *Evolution of Binary and Multiple Star Systems*, ed. P. Podsiadlowski, S. Rappaport, A. R. King, F. D'Antona, & L. Burderi, 455–+

- Burderi, L., Di Salvo, T., D'Antona, F., Robba, N. R., & Testa, V. 2003, *A&A*, 404, L43
- Burderi, L., Di Salvo, T., Menna, M. T., Riggio, A., & Papitto, A. 2006, *ApJ*, 653, L133
- Burderi, L., Possenti, A., Colpi, M., di Salvo, T., & D'Amico, N. 1999, *ApJ*, 519, 285
- Burderi, L., Possenti, A., D'Antona, F., et al. 2001, *ApJ*, 560, L71
- Burderi, L., Riggio, A., di Salvo, T., et al. 2009, *A&A*, 496, L17
- Burgay, M., Burderi, L., Possenti, A., et al. 2003a, *ApJ*, 589, 902
- Burgay, M., Burderi, L., Possenti, A., et al. 2003b, *ApJ*, 589, 902
- Camilo, F., Lorimer, D. R., Freire, P., Lyne, A. G., & Manchester, R. N. 2000, *ApJ*, 535, 975
- Casella, P., Altamirano, D., Patruno, A., Wijnands, R., & van der Klis, M. 2008, *ApJ*, 674, L41
- Chadwick, J. 1932, *Nature*, 129, 312
- Chakrabarty, D. & Morgan, E. H. 1998, *Nature*, 394, 346
- Cocke, W. J., Disney, M. J., & Taylor, D. J. 1969, *Nature*, 221, 525
- Cook, G. B., Shapiro, S. L., & Teukolsky, S. A. 1994, *ApJ*, 423, L117
- Cordes, J. M. & Lazio, T. J. W. 2001, *ApJ*, 549, 997
- Cordes, J. M. & Lazio, T. J. W. 2002, *ArXiv Astrophysics e-prints*
- D'Avanzo, P., Campana, S., Casares, J., et al. 2008, in *American Institute of Physics Conference Series*, Vol. 1068, American Institute of Physics Conference Series, 217–220
- Deloye, C. J., Heinke, C. O., Taam, R. E., & Jonker, P. G. 2008, *MNRAS*, 391, 1619
- Di Salvo, T. & Burderi, L. 2003, *A&A*, 397, 723

- Di Salvo, T., Burderi, L., Riggio, A., Papitto, A., & Menna, M. T. 2007, in *American Institute of Physics Conference Series*, Vol. 924, *The Multicolored Landscape of Compact Objects and Their Explosive Origins*, ed. T. Di Salvo, G. L. Israel, L. Piersant, L. Burderi, G. Matt, A. Tornambe, & M. T. Menna, 613–622
- Di Salvo, T., Burderi, L., Riggio, A., Papitto, A., & Menna, M. T. 2008a, *MNRAS*, 389, 1851
- Di Salvo, T., Burderi, L., Riggio, A., Papitto, A., & Menna, M. T. 2008b, in *American Institute of Physics Conference Series*, Vol. 1054, *American Institute of Physics Conference Series*, 173–182
- Eggleton, P. P. 1983, *ApJ*, 268, 368
- Emmering, R. T. & Chevalier, R. A. 1989, *ApJ*, 345, 931
- Falanga, M., Bonnet-Bidaud, J. M., Poutanen, J., et al. 2005, *A&A*, 436, 647
- Faulkner, J. 1971, *ApJ*, 170, L99+
- Frank, J., King, A., & Raine, D. J. 2002, *Accretion Power in Astrophysics: Third Edition* (*Accretion Power in Astrophysics*, by Juhan Frank and Andrew King and Derek Raine, pp. 398. ISBN 0521620538. Cambridge, UK: Cambridge University Press, February 2002.)
- Galloway, D. K., Chakrabarty, D., Morgan, E. H., & Remillard, R. A. 2002, *ApJ*, 576, L137
- Galloway, D. K., Markwardt, C. B., Morgan, E. H., Chakrabarty, D., & Strohmayer, T. E. 2005, *ApJ*, 622, L45
- Geppert, U. & Urpin, V. 1994, *MNRAS*, 271, 490
- Ghosh, P. & Lamb, F. K. 1992, in *X-ray Binaries and Recycled Pulsars*, ed. E. P. J. van den Heuvel & S. A. Rappaport (Dordrecht: Kluwer), 487–510
- Gilfanov, M., Revnivtsev, M., Sunyaev, R., & Churazov, E. 1998, *A&A*, 338, 83
- Goldreich, P. & Julian, W. H. 1969, *ApJ*, 157, 869

- Habets, G. M. H. J. & Heintze, J. R. W. 1981, *A&AS*, 46, 193
- Hansen, B. M. S. & Phinney, E. S. 1998a, *MNRAS*, 294, 557
- Hansen, B. M. S. & Phinney, E. S. 1998b, *MNRAS*, 294, 569
- Hartman, J. M., Patruno, A., Chakrabarty, D., et al. 2008, *ApJ*, 675, 1468
- Hartman, J. M., Patruno, A., Chakrabarty, D., et al. 2009, *ApJ*, 702, 1673
- Hayakawa, S. 1985, *Phys. Rep.*, 121, 317
- Hessels, J., Ransom, S., Stairs, I., et al. 2006, *Science*, astro-ph/0601337
- Hewish, A., Bell, S. J., Pilkington, J. D. H., Scott, P. F., & Collins, R. A. 1968, *Nature*, 217, 709
- Iacolina, M. N., Burgay, M., Burderi, L., Possenti, A., & di Salvo, T. 2009, *A&A*, 497, 445
- Jahan Miri, M. 1996, *MNRAS*, 283, 1214
- Jahan Miri, M. & Bhattacharya, D. 1994, *MNRAS*, 269, 455
- Kaaret, P., Morgan, E. H., Vanderspek, R., & Tomsick, J. A. 2006, *ApJ*, 638, 963
- King, A. R., Pringle, J. E., & Livio, M. 2007, *MNRAS*, 376, 1740
- Konar, S. & Bhattacharya, D. 1997, *MNRAS*, 284, 311
- Konar, S. & Bhattacharya, D. 1999, *MNRAS*, 303, 588
- Konar, S. & Choudhuri, A. R. 2004, *MNRAS*, 348, 661
- Kraft, R. P., Mathews, J., & Greenstein, J. L. 1962, *ApJ*, 136, 312
- Krauss, M. I., Wang, Z., Dullighan, A., et al. 2005, *ApJ*, 627, 910
- Krimm, H. A., Markwardt, C. B., Deloye, C. J., et al. 2007, *ApJ*, 668, L147
- Kuiper, L., Hermsen, W., Verbunt, F., & Belloni, T. 1998, *A&A*, 336, 545
- Kulkarni, S. R. 1986, *ApJ*, 306, L85

- Landau, L. D. & Lifshitz, E. M. 1975, *Course of Theoretical Physics, Vol. 2, The Classical Theory of Fields*, 4th edn. (Oxford: Pergamon Press)
- Lattimer, J. M. & Prakash, M. 2007, *Phys. Rep.*, 442, 109
- Lorimer,  
D. R. & Kramer, M. 2004, *Handbook of Pulsar Astronomy (Handbook of pulsar astronomy, by D.R. Lorimer and M. Kramer. Cambridge observing handbooks for research astronomers, Vol. 4. Cambridge, UK: Cambridge University Press, 2004)*
- Lundgren, S. C., Cordes, J. M., Foster, R. S., Wolszczan, A., & Camilo, F. 1995, *BAAS*, 186, 4703
- Manchester, R. N., Hobbs, G. B., Teoh, A., & Hobbs, M. 2005, *VizieR Online Data Catalog*, 7245, 0
- Manchester, R. N., Lyne, A. G., D'Amico, N., et al. 1996, *MNRAS*, 279, 1235
- Markwardt, C. B., Altamirano, D., Swank, J. H., et al. 2009, *The Astronomer's Telegram*, 2197, 1
- Markwardt, C. B., Smith, E., & Swank, J. H. 2003, *The Astronomer's Telegram*, 122, 1
- Markwardt, C. B. & Swank, J. H. 2003, *IAU Circ*, 8144, 1
- Markwardt, C. B., Swank, J. H., Strohmayer, T. E., Zand, J. J. M. i., & Marshall, F. E. 2002, *ApJ*, 575, L21
- Monelli, M., Fiorentino, G., Burderi, L., et al. 2005, in *American Institute of Physics Conference Series, Vol. 797, Interacting Binaries: Accretion, Evolution, and Outcomes*, ed. L. Burderi, L. A. Antonelli, F. D'Antona, T. Di Salvo, G. L. Israel, L. Piersanti, A. Tornambè, & O. Straniero, 565–568
- Morton, D. C. 1960, *ApJ*, 132, 146
- Navarro, J., de Bruyn, G., Frail, D., Kulkarni, S. R., & Lyne, A. G. 1995, *ApJ*, 455, L55

- Paczyński, B. 1967, *Acta Astronomica*, 17, 287
- Paczyński, B. 1971, *Ann. Rev. Astr. Ap.*, 9, 183
- Paczynski, B. & Sienkiewicz, R. 1981, *ApJ*, 248, L27
- Papitto, A., di Salvo, T., Burderi, L., et al. 2007, *MNRAS*, 375, 971
- Papitto, A., Menna, M. T., Burderi, L., et al. 2005, *ApJ*, 621, L113
- Papitto, A., Menna, M. T., Burderi, L., di Salvo, T., & Riggio, A. 2008, *MNRAS*, 383, 411
- Poutanen, J. 2008, in *American Institute of Physics Conference Series*, Vol. 1068, *American Institute of Physics Conference Series*, ed. R. Wijnands, D. Altamirano, P. Soleri, N. Degenaar, N. Rea, P. Casella, A. Patruno, & M. Linares, 77–86
- Rappaport, S., Joss, P. C., & Webbink, R. F. 1982, *ApJ*, 254, 616
- Rappaport, S. A., Fregeau, J. M., & Spruit, H. 2004, *ApJ*, 606, 436
- Ruderman, M. 1991, *ApJ*, 366, 261
- Ruderman, M. A. & Sutherland, P. G. 1975, *ApJ*, 196, 51
- Sauls, J. A. 1989, in *Timing Neutron Stars*, (NATO ASI Series), ed. H. Ögelman & E. P. J. van den Heuvel (Dordrecht: Kluwer), 457–490
- Schönberner, D., Driebe, T., & Blöcker, T. 2000, *A&A*, 356, 929
- Shahbaz, T., Casares, J., & Charles, P. A. 1997, *A&A*, 326, L5
- Shakura, N. I. & Syunyaev, R. A. 1973, *A&A*, 24, 337
- Srinivasan, G., Bhattacharya, D., Muslimov, A. G., & Tsygan, A. I. 1990, *Curr. Sci.*, 59, 31
- Szkody, P., Fraser, O., Silvestri, N., et al. 2003, *AJ*, 126, 1499
- Taam, R. E., King, A. R., & Ritter, H. 2000, *ApJ*, 541, 329
- Tauris, T. M. & Savonije, G. J. 1999, *A&A*, 350, 928

- Taylor, J. H. & Cordes, J. M. 1993, *ApJ*, 411, 674
- Taylor, J. H. & Manchester, R. N. 1977, *ApJ*, 215, 885
- Torres, M. A. P., Jonker, P. G., Steeghs, D., et al. 2008, *ApJ*, 672, 1079
- van Paradijs, J. 1982, *A&A*, 107, 51
- Verbunt, F. 1993, *Ann. Rev. Astr. Ap.*, 31, 93
- Verbunt, F. & Zwaan, C. 1981, *A&A*, 100, L7
- Webbink, R. F., Rappaport, S., & Savonije, G. J. 1983, *ApJ*, 270, 678
- Wijnands, R., Homan, J., Heinke, C. O., Miller, J. M., & Lewin, W. H. G. 2005, *ApJ*, 619, 492
- Wijnands, R. & van der Klis, M. 1998, *Nature*, 394, 344
- Zhang, C. M. & Kojima, Y. 2006, *MNRAS*, 366, 137

# Acknowledgements

I would like to thank Prof. Luciano Burderi for his precious guidance during all the course of this work. I am sincerely grateful to Marta Burgay and Andrea Possenti, whose constant guidance, encouragement and support, throughout the course of this work, enabled me to develop this PhD thesis work. I also want to thank Tiziana Di Salvo for her precious comments and advices.

My acknowledgements also go to Prof. Roberto Turolla, for his comments, very helpful to improve the presentation of my work.

Thank to my family: unless they, this thesis would not have been possible.

Last but not least, all the people of the Cagliari Astronomical Observatory and all the colleagues and friends of the Physics Department of Cagliari, that made more pleasant the work of these years.